RADIATION FROM SMALL-SCALE MAGNETIC FIELD TURBULENCE:
Implications for Gamma-Ray Bursts and Laboratory Astrophysical Plasmas

By

Sarah J. Reynolds

Submitted to the Department of Physics and Astronomy
and the Graduate Faculty of the University of Kansas
in partial fulfillment of the requirements for the degree of

Doctor of Philosophy

Committee members

Mikhail Medvedev, Chair

Thomas Cravens

Barbara Anthony-Twarog

Gregory Rudnick

Mark Richter

Date defended: April 10, 2012

The Dissertation Committee for Sarah J. Reynolds certifies
that this is the approved version of the following dissertation:

RADIATION FROM SMALL-SCALE MAGNETIC FIELD TURBULENCE:
Implications for Gamma-Ray Bursts and Laboratory Astrophysical Plasmas

Committee:

Mikhail Medvedev, Chair

Thomas Cravens

Barbara Anthony-Twarog

Gregory Rudnick

Mark Richter

Date approved: April 10, 2012

Abstract

Relativistic charged particles moving within regions of small-scale magnetic field turbulence radiate as they undergo transverse accelerations reflective of the magnetic field variation along the particle's path. For a particle of Lorentz factor γ, relativistic beaming concentrates the bulk of the particle's emission within a small angle $1/\gamma$ from the particle's forward direction. Synchrotron radiation is produced when large-scale magnetic fields cause the charged particles to gyrate, with the resulting radiation spectrum being primarily determined by the intermittent sweep of the relativistic beaming cone past the direction to the observer. In small-scale magnetic field turbulence, magnetic fields may be locally strong but varies over sufficiently small scales that the particle's emission is more consistently oriented towards a particular direction. Consequently, deflection effects cease to dominate the observed spectrum and the standard synchrotron model no longer applies. In this dissertation, we focus on the strong jitter radiation regime, in which the field varies over sufficiently short scales that the particle is never substantially deviated from a straight line path and an observer in the particle's forward direction receives consistently strong radiation over many correlation lengths of the magnetic field. We develop the general jitter radiation solutions for such a case and demonstrate that the resulting radiation spectrum differs notably from the synchtrotron spectrum and depends directly on the spectral distribution of the magnetic field encountered by the particle.

The Weibel-like filamentation instability generates small-scale magnetic field turbulence through current filamentation in counterstreaming particle populations, such as may be found at or near propagating shock fronts, in outflow from regions of magnetic reconnection, or from a variety of other scenarios producing an anisotropic particle velocity distribution. The current filamentation produces an anisotropy in magnetic field distribution that causes the jitter radiation spectrum to be sensitive to the radiating particle's orientation with respect to the filamentation axis. Because the spectrum observed from any given direction will be dominated by emission from particle's moving along that particular line-of-sight, this results in a natural angular dependence of the jitter radiation spectrum.

We explore the implications of jitter radiation's spectral sensitivity to the field anisotropy produced by the Weibel-like filamentation instability to relevant astrophysical and laboratory plasma scenarios. We calculate the jitter radiation spectra that may be produced in a high-energy density laboratory plasma by using quasi-monoenergetic electron beams to generate and then probe a region of current filamentation, and show that the jitter radiation may be used as a radiative diagnostic to determine features of the magnetic field distribution within this region.

For gamma-ray bursts, this instability may play a significant role in generating magnetic field strength from relativistic collisionless shocks or other particle acceleration mechanisms. We show that the viewing angle dependence of the jitter radiation spectrum can result in a rapidly time-evolving spectrum whose hard-to-soft evolution, synchrotron-violating low-energy spectral indices, and correlation between low-energy spectral hardness and the flux at peak energy may explain trends noticed in time-resolved GRB spectral evolution. We generate the jitter radiation spectra as would be produced in the co-moving frame by a single, instantantaneously-illuminated shock front, which may then be relativistically transformed with appropriate geometry into

a time-evolving spectrum and multiple such signals assembled to produce “synthetic” GRB for comparison with observations.

Acknowledgments

Completing a dissertation is a monumental task and I wish to express my grateful appreciation for the many wonderful colleagues, friends, and family members that have supported me in attaining this goal. First, I wish to thank my advisor Dr. Misha Medvedev for his patient guidance, expert direction, unfailing support, and the many ways his influence has made me a better scholar in our years of working together. Also, my work has been made better and more enjoyable by the collaboration and helpful contributions of my friend and colleague Harsha Pothapragada. I would also like to thank my committee members, Drs. Tom Cravens, Greg Rudnick, and Barbara Anthony-Twarog, for their good advice on matters of research, career, and life in general.

The Department of Physics and Astronomy at the University of Kansas has been a wonderful place to learn and grow as a student and a scholar, and I will be forever grateful to the many professors here who have encouraged me along the way. The KU Society of Physics Students has also been such a delightful group full of camaraderie and shared learning, and I will never forget the joys I have had in getting to know so many students here.

Finally, to my family and close friends who have put up with me through the ups and downs, many thanks – I could never have done this without your love, support, patience, and encouragement.

Contents

List of Figures

Chapter 1

Introduction

1.1 Context and Outline

Understanding the dynamics of high-energy astrophysical phenomena is one of the great challenges facing modern astronomers. Whereas our ancestors viewed the celestial realms as a place of reliable constancy, we now know that our universe is actually one of constant change across a variety of scales in time and space. Through explosive events like supernovae (SNe) and gamma-ray bursts (GRBs), we find that rapid change is not only possible, it is essential in redistributing matter and energy in a variety of astronomical processes. Even the Sun, our own stable star, releases energy through rapid events ranging down to a few hundred seconds in time. Furthermore, space-based detectors have given us a new view of the energetic X-ray and gamma-ray universe, and in particular have revolutionized our understanding of the extreme events in which matter and energy are redistributed in the cycles of stellar and galactic evolution.

While the high energies of such astrophysical events make them of intrinsic interest, their extreme dynamics and rapid topological changes often make them difficult to treat analytically. In particular, the dynamic processes in such high-energy systems can generate turbulence and instabilities that distribute energy across a wide range of spatial scales. Changes in large-scale magnetic field topology and particle flows can thus be strongly affected by physics occurring on scales many orders of magnitude smaller. The breadth of scales involved makes modeling such systems computationally intensive. While many high-energy astrophysical phenomena are being simulated using advanced computing techniques, much work remains in verifying that the results of such simulations are well quantified, reproducible, and consistent across multiple systems.

There is a standard “lore” in astrophysics which tends to consider all radiation produced by relativistic particles to be synchrotron radiation (or possibly relativistic bremsstrahlung). However, as we shall demonstrate, synchrotron radiation is only one possible solution to the radiation equations for a relativistic particle, occuring specifically in the limit of large-scale magnetic fields. The synchrotron radiation approach breaks down when magnetic fields vary over spatial scales too small for the particle to complete a gyration without encountering a variation in the local magnetic field.

Radiation from relativistic particles moving in small-scale turbulent magnetic fields must instead be modeled via jitter radiation, in which the particle’s emission directly reflects the underlying magnetic field variations accelerating the particle. In this thesis we focus on applying the theory of jitter radiation to correctly understand the radiation produced by relativistic charged particle populations moving in instability-generated magnetic fields that are locally strong in magnitude but have correlation lengths shorter than the particle’s gyroradius.

In this chapter we present the context for our work and background on the laboratory and astrophysical plasma environments which we will consider. Chapter 2 develops the mathematical theory of jitter radiation used in our calculations. Chapter 3 presents our results of applying jitter radiation theory to calculate the angular distribution of emission that could be produced in laser-plasma experiments by particles moving within regions of filamentation. In Chapter 4, we present the results of using jitter radiation to calculate the angle-averaged emission produced in the rest frame of a propagating radiating region containing small-scale magnetic field turbulence. These results can then be relativistically transformed and used to simulate a gamma-ray burst (GRB) event as a series of illuminating "flashes" from multiple shock or reconnection events within the relativistically-propelled outflow from a central engine. Chapter 5 presents further analysis of the jitter radiation solutions and explorations of the effect of variations in our initial choice of magnetic field parameters upon the resulting spectra. Chapter 6 contains analysis and conclusions from our full study of jitter radiation.

1.2 Magnetic Field Dynamics in Plasma Physics

The energies of many astrophysical systems are such that they contain a substantial charged particle population. In appropriate conditions, these charged particle populations can exhibit unique collective behaviors as a plasma, essentially a charged particle fluid in which fluid flow and bulk motions are intrinsically linked to electric and magnetic field. Plasma is the natural state of matter for stellar interiors and outflow; furthermore, plasmas permeate much of what is commonly considered "empty" space. Plasma processes are essential to the development and persistence of stellar, planetary, and interstellar magnetic fields.

In a plasma, the approximate equality between the local number density of positive and negative charges ($n_+ \approx n_-$) establishes quasi-neutrality so that the overall field produced by the collection of particles is negligible outside the plasma. Within the plasma, a sufficiently large charge density of a particular species is required in relation to its average temperature so that the local thermal motions of particles are effectively screened at large distances by compensating changes in the spatial distribution of neighboring particles. The radius of the sphere of influence of an individual particle's motion (outside of which the charge is "screened") is known as the Debye length $\lambda_D = \sqrt{k_B T_e / 4\pi n_e q_e^2}$ (where k_B is the Boltzmann constant, and T_e, n_e, and q_e are the temperature, number density and charge of the electrons, in a plasma with minimal ion motion). This establishes the minimum scale for collective motions within the plasma.

The intrinsic link between particle motions and field configuration within a plasma allows magnetic field to be created, modified, or destroyed by various plasma processes and instabilities. Within a plasma, any attempted change in magnetic field configuration causes the particles to react inductively to preserve their local magnetic field. In ideal magnetohydrodynamics (MHD), the plasma is a perfect conductor in which there is no resistance to this inductive behavior (resistivity $\eta = 0$), allowing for magnetic flux to be conserved within each volume element of the plasma so that a magnetic field line is effectively embedded or "frozen" into the plasma. The propagation of each volume element of the plasma carries the "frozen-in" magnetic field lines along within that volume. Restrictions on the free motion of the plasma particles in regions of non-ideal MHD may prevent the plasma particles from perfectly preserving the local field configuration, in which case the motion of the field line through the plasma can be described by a term of magnetic diffusivity or resistance which defines the rate at which the field line can "slip" through the plasma. For a plasma of resistivity η, the distance ℓ which a field line can slip in time t is given by

$$\ell = \sqrt{\frac{\eta c t}{4\pi}} \tag{1.1}$$

Consequently, the flux freezing condition in such a plasma will hold true for scales larger than ℓ.

Because of flux freezing, magnetic field topology within a plasma can differ substantially from what it would be outside this charged particle medium. In empty space, magnetic field lines are completely defined by source end points. No “kinks” are possible for a magnetic field line in empty space, other than where any changes to the magnetic field propagate at the speed of light to update in space. On the other hand, magnetic field topology in a plasma reflects the particle motions within the plasma and can be kinked or twisted in what are effectively higher-energy configurations. Particle kinetic energies are tied into maintaining these high-energy field configurations; consequently, the magnetic field can be viewed as storing magnetic energy.

To visualize this, one can consider what happens when a bar magnet is moved in empty space versus within a plasma. In empty space, the bar magnet defines the magnetic field through all surrounding space. If the bar magnet is suddenly moved, the magnetic field simply moves with it (updating at the speed of light). On the other hand, if a bar magnet is embedded within a plasma, the plasma particles have established motions in response to the imposed dipole magnetic field (we are assuming that the bar magnet has been in its position long enough for the system to reach an equilibrium). If the embedded bar magnet is suddenly moved, the change in its magnetic field contribution requires corresponding changes in the surrounding particle’s motions in order for a new equilibrium to be established. Additionally, even if the bar magnet field source remains fixed, the surrounding magnetic field could be modified by dynamics in the plasma itself, as any forced plasma flow will necessarily result in the propagation of the embedded magnetic field.

When plasma particles are forced to a critical point in which the ideal MHD conditions break down, the result can be a rapid topological transformation of the magnetic field into a lower-energy configuration, a process known as magnetic reconnection. Magnetic reconnection releases the stored magnetic energy, redistributing the particle kinetic energies that were tied into maintenance of the high-energy field configuration. This can result in high-velocity plasma (and field) outflow from a reconnection region. Magnetic reconnection operates within a variety of astrophysical systems, playing an especially notable role within flaring systems and other sites of rapid energy release (see Zweibel and Yamada [2009] for a review).

Particle motions and magnetic field topology are intrinsically linked within a plasma. Like their fluid counterparts, plasmas are subject to a variety of instabilities in which a small perturbation within the plasma can lead to the growth of new plasma motions that may build, modify, or destroy magnetic field as a result. Turbulent processes, with their chaotic particle motions and transfer of energy across multiple length scales, can tangle or disrupt existing magnetic fields. As we will see in the following section, we are specifically interested in a mechanism by which initially small magnetic field fluctuations grow in strength within a plasma population with an anisotropic distribution in velocity space.

1.3 Small-Scale Magnetic Turbulence from the Weibel-like Filamentation Instability

Counter-streaming particle populations can enhance existing magnetic field anisotropies in the plane transverse to their streaming due to an instability which coalesces the counterstreaming particles into current filaments. Medvedev and Loeb [1999] proposed that such an instability could be responsible for magnetic field production in relativistic collisionless shocks, generating strong magnetic fields with short correlation lengths.

The particular instability mechanism we are interested in has been called by various names in the literature, and has often been associated with the Weibel instability due to its origins in an initial particle distribution function (PDF) anisotropy. Weibel [1959] noted that anisotropic velocity distributions of electrons in a plasma could lead to the growth of transverse electromagnetic waves. Fried [1959] provided an example of a related physical mechanism for a particular anistropy in the electron PDF by showing that counterstreaming electrion beams would be unstable to magnetic field perturbations transverse to the beam and result in the formation of current filaments. Although the filamentation instability Fried described is closely related to the Weibel instability, the Weibel instability itself is significantly more general and includes the effects of a Maxwellian thermal velocity distribution. Thus, although the two instabilities are often confusingly convolved with one another in the literature, they are not quite equivalent.[Fried, 1959, Bret et al., 2010] For our purposes here we will thus designate the filamentation instability mechanism originating with Fried as the Weibel-like filamentation instability, with a mechanism as described in the following paragraph.

The Weibel-like filamentation instability forms when a small magnetic field perturbation causes counterstreaming particle populations to form into current filaments. The basic mechanism is illustrated in Figure 1.1. In the idealized version shown here, the instability begins from two particle populations which are uniform in density but with oppositely directed bulk flow vectors. (In our simple illustration, we assume that the particles are all identical in mass and charge; although in a real plasma there will be both ions and electrons, the generally heavier mass of the ions tends to separate the dynamical timescales of positively and negatively charged particles sufficiently that they can be largely treated as separate systems.) A small field perturbation in the plane transverse to particle flow causes the particles to be slightly redirected by the Lorentz force, so that the initially uniform current density begins to coalesce into current filaments. In the sinusoidal perturbation shown, one can see that the particles are effectively funneled towards the nodes of the function, with the oppositely directed “upward” and

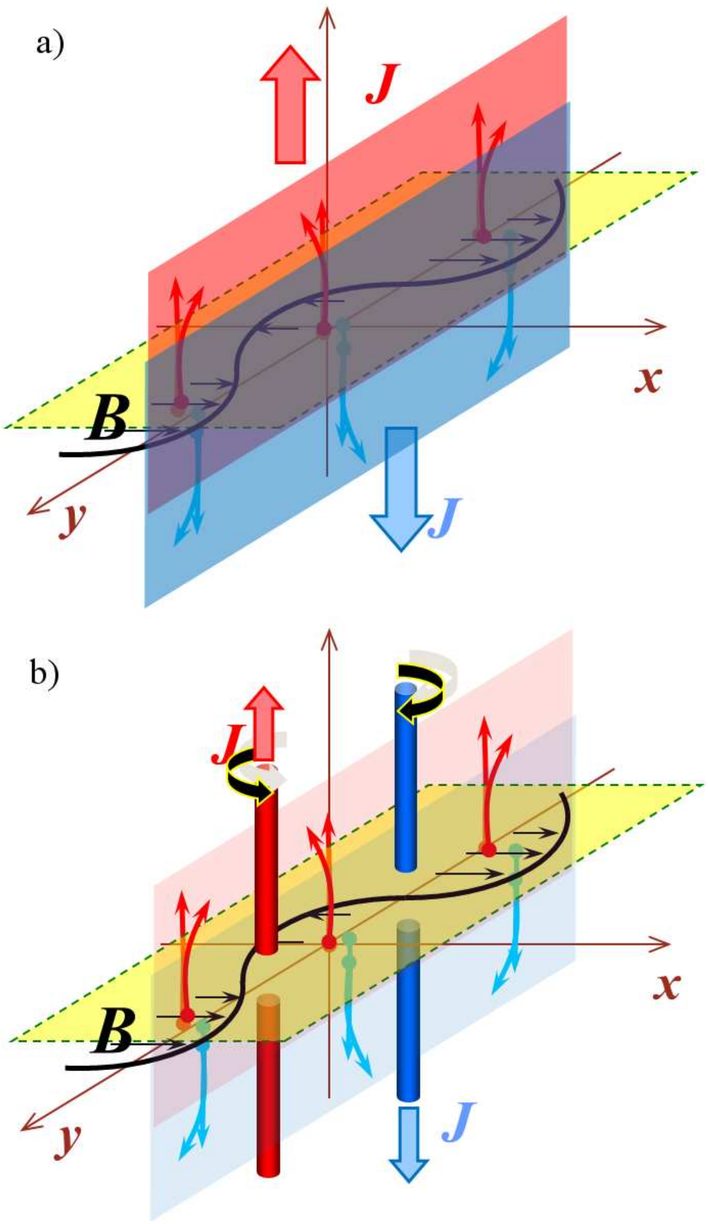

Figure 1.1: The Weibel-like filamentation instability occurs when a small transverse magnetic field perturbation causes counterstreaming particle populations with an initially uniform current density across the *yz*-plane (top) to be "funneled" into current filaments (bottom). The simple sinusoidal perturbation shown directs the oppositely-directed particles towards alternate nodes of the sine wave where current filaments grow. As can be seen from the Lorentz force, the concentration of current into filaments produces an enhancement in the original perturbation until the filament growth eventually saturates.

“downward” particles being redirected to alternate nodes of the function. As these current filaments form, they reinforce the initial magnetic field perturbation, causing the local field fluctuations in the transverse plane to grown in strength and contribute to further current filamentation. Eventually the instability will reach a saturation point that limits the spatial scale of the magnetic field variations and further growth of the current filaments. The Weibel-type filamentation instability is of interest for a variety of relativistic collisionless plasmas because of its ability to grow small-scale magnetic turbulence. The randomly oriented magnetic field variations in the plane transverse to particle counterstreaming become enhanced in strength as the instability proceeds, so that when the filamentation reaches its saturation point the local magnetic fields have been increased in strength but still have short correlation lengths.

This instability mechanism has been extensively studied via particle-in-cell (PIC) computer simulations, for a variety of plasma compositions and initial and boundary conditions. (See Silva et al. [2003], Bret et al. [2010], Fonseca et al. [2003], Chang et al. [2008], Frederiksen et al. [2004], Nishikawa et al. [2009] for some examples.) Simulations indicate that the current filaments start small and then merge as they grow, reaching saturation at some limiting density and scale of the filaments. Early simulations and analytical treatments generally assumed that the Weibel-like filamentation instability would occur due to interpenetrating plasma populations at or just upstream from a propagating shock front. However, this instability appears to be much more ubiquitous, occurring in many plasma scenarios with an appopriate anisotropy in particle distributions.[Bret et al., 2010] This instability may also lead to filamentation in regions where magnetic reconnection drives an outflow into the surrounding plasma.[Zenitani and Hesse, 2008]

1.4 Radiation from Small-Scale Turbulence

Electromagnetic radiation is released by the rearrangement of electric and magnetic fields due to the acceleration of charged particles. Any change in either the direction or speed of a charged particle's motion can produce radiation, which is essentially a traveling perturbation of the electric and magnetic fields. Charged particles moving at relativistic speeds are known to emit the bulk of their radiation within a small angle of their forward direction. This property, known as relativistic beaming, can be calculated directly from the radiation equations, as will be shown in Chapter 2. For a radiating particle moving with Lorentz factor γ, the bulk of the emission is emitted within an angle $\alpha_{em} = 1/\gamma$ of the direction of the particle's instantaneous velocity.

In a large-scale magnetic field, the particle is deflected by the Lorentz force so that it follows a helical path. This deflection causes the particle to radiate, but since its instantaneous direction is constantly changing, the relativistic beaming cone is constantly being redirected as the particle gyrates. The bulk of the radiation is not consistently emitted into any one direction relative to an inertial reference frame. Consequently, an observer will either receive very low levels of emission if positioned outside the sweep of the radiation cone or will receive periodic pulses of strong radiation from the moments when the particle's velocity is directed towards the observer. This is the synchrotron radiation scenario, in which the the strongly deflected particle trajectory causes the radiation emitted into a particular direction in space to vary substantially in intensity as the particle propagates. The spectrum of radiation received by the observer in this case is thus dominated by the frequency of the pulses as the particle spirals.

The characteristic frequency and the shape of the synchrotron radiation spectrum are a result of the regular sweep of the relativistically beamed radiation cone past the direction to an observer. For a particle with charge q, mass m and Lorentz factor γ, responding to a magnetic field $\boldsymbol{B}$, the particle gyrates with a frequency $\omega_r = qB/\gamma m = \omega_g/\gamma$. Accounting for relativistic beaming, the particle radiates into a given direction only in short pulses of duration $\Delta t = 1/\gamma^2 \omega_g$. The resulting radiation is dominated by the critical frequency $\omega_c = (3/2)\gamma^2 \omega_g \sin \alpha_B$, where α_B is the radiating particle's pitch angle with respect to the magnetic field.[Rybicki and Lightman, 2004, Ginzburg and Syrovats, 1965] For $\omega < \omega_c$, the radiation spectrum produced by a single particle is a power law with a spectral index of 1/3; for $\omega > \omega_c$ the spectrum decreases exponentially. For a distribution of particles, the convolution of such spectra can modify the shape of the resulting synchrotron radiation spectrum for a particle distribution, but the low-frequency spectral index remains limited to values below 1/3 (-2/3 in the photon spectrum) in the absence of absorption.

If instead of remaining (nearly) homogeneous on large-scales the magnetic field orientation varies over a small scale relative to the distance on which a particle would gyrate around the local field line, the particle will still be deflected, but the deflection will not be consistently directed towards any particular direction long enough to substantially redirect the particle's velocity and emission. Consequently, the particle will emit strong radiation consistently along a certain line of sight as it undergoes these small-scale deflections from the varying magnetic field. The spectrum of radiation received by an observer positioned in the direction of the particle's velocity will not be influenced by major changes in the amplitude of the emission and will instead depend directly upon the deflections undergone by the particle due to the magnetic field. Since the particle can be thought of as "jittering" with small transverse accelerations as it propagates, the resulting emission has been called "jitter radiation". In principle jitter radiation has always been a possible limiting solution of the radiation equations (see Landau and Lifshitz [1971], Brau [2004] for the classic textbook examples); however, Medvedev [2000] pointed out its relevance for modeling radiation from small-scale magnetic field turbulence and thus for gamma-ray bursts and related astrophysical systems.[Medvedev and Loeb, 1999, Medvedev, 2006, Reynolds et al., 2010]

1.5 Implications for GRB studies

Gamma-ray bursts (GRBs) have long been an enigmatic challenge for high-energy astrophysics because of the very high energies and short dynamical timescales involved. Observationally, a gamma-ray burst is simply a brief, strong (notably above background) gamma-ray signal. The typical duration of a GRB is less than a few hundred seconds.

Because gamma-rays are strongly absorbed by the Earth's atmosphere, studies of astronomical gamma-ray sources require space-based detectors. The first gamma-ray burst detections were made in the late 1960s by the Vela satellites, a small network of satellites which had been launched to watch for gamma-ray and X-ray signatures of nuclear explosions in order to monitor compliance with the Nuclear Test Ban treaty.[Mészáros, 2006]. Scientists working with the Vela project noticed several strong gamma-ray signals that had no corresponding X-ray signature and did not appear to be connected with any other indicators of nuclear weapons testing. Studies of the signal detection across multiple members of the Vela satellite network indicated that the gamma-ray bursts were not associated with any particular local source and appeared to come from deep space. Klebesadel et al. [1973] first published the declassified detection of 13 gamma-ray bursts.

For a couple decades, progress in GRB research was severely limited by the observational challenges of their short time durations, coupled with the inherent difficulty of focusing or tracing gamma-ray signals to indicate a point of origin. Early statistical studies suggested that GRBs were detected isotropically from all directions in space, which was confirmed in 1993 by the Burst Alert and Transient Source Experiment (BATSE) on the Compton Gamma-Ray Observatory (CGRO).[Mészáros, 2006] Firm associations with source objects were not achieved until the late 1990s when improving rapid response networks and instrumentation allowed the Dutch-Italian Beppo-SAX satellite to make the first detection of an X-ray transient associated with GRB 970228. (GRB names are based on the date of observation, so that GRB 970228 corresponds to the GRB detected on February 28, 1997. Multiple GRB detections on the same day are denoted by letters after the numerical designation.) The X-ray transient associated with GRB 9702228 improved localization sufficiently to lead to the corresponding discovery of the first GRB optical counterpart and started the new era of GRB afterglow observations.

Afterglow observations in X-ray, ultraviolet (UV), and optical allow for much improved localization of GRB sources. Additionally, minimum redshifts may be determined from spectral features in the optical afterglow for some GRBs. Redshifts determined for GRBs so far range up to $z > 9$, with the average value among current (Swift) burst detections of $z \approx 2$, verifying that GRBs do indeed originate at cosmological distances.[Gehrels et al., 2009] The isotropic equivalent energy (that is, the total energy emitted by the source if the energy detected at our observation point is representative of that emitted isotropically in all directions) released is thus found to be approximately 10^{53} ergs in gamma-ray emission alone, making GRBs one of the most luminous events in the known universe. In the few seconds of its duration, a GRB outshines its host galaxy and releases more energy than the Sun will produce in its entire lifetime.

The number of observed GRBs now totals in the thousands, with new detections occuring nearly every day. The real advances in our understanding of these events have come not from just the increasing quantity of detections, but by improvements in the breadth of information obtained. Gamma-ray bursts are recognized and defined by their light curve, tracking how the brightness of the event changes with time. A GRB's initial bright "prompt emission" (recognized predominantly in gamma-rays although we now know that the energy coverage does extend to lower energies) declines rapidly in brightness after a few hundred seconds or less, followed by afterglow emission at longer wavelengths. The prompt emission phase itself can vary widely in the lightcurve progression, from a single peak with smooth decay, to more complex multiple peak behavior.

The duration of the prompt gamma-ray emission is often quantified by defining T_{90} as the time duration in which 90% of gamma-ray counts above background are recorded. A bimodality in the T_{90} distribution seems to indicate that GRBs may be divided into two classifications, short ($T_{90} < 2$ seconds) and long ($T_{90} > 2$ seconds). Some evidence indicates that short GRBs may differ spectroscopically and in source location from long GRBs and may have underlying differences in their production mechanism; however, strong observational biases and inconsistencies among different detectors have made this difficult to determine conclusively.[Ghirlanda et al., 2009]

The fluence of detected GRBs compared with the cosmological distances determined by redshift measurements in the afterglow of certain GRBs require substantial energies in excess of 10^{53} ergs to be released at the GRB source. (This is true even if the emission is strongly beamed.) Such energies suggest that the central engine which drives the GRB is likely a cataclysmic event involving the core collapse of very high mass stars or the merger of massive compact stellar remnants (e.g., a merger between two neutron stars). The rapid time variability of the flux indicates that the source of the energy must itself be very compact, driving some strong outflow which carries energy either kinetically or as Poynting flux out to some distance at which the energized matter becomes thin enough for radiation to escape from the system. This outflow is likely jetted within a certain solid angle rather than isotropic around the central engine, evidenced in many GRB spectra by achromatic light breaks as the edge of the propagating jet front passes the line of sight to the observer.

For our purposes in this thesis, the central engine driving the outflow is of little concern, as we are primarily concerned with understanding the radiation mechanisms in the relativistically-propagating jet. The prompt and afterglow emission have generally been understood as originating in a series of internal and external shocks. The basic theoretical model of a GRB suggests that prompt emission originates in the internal shocks between shells of outflow material moving with slightly different speeds, while afterglow emission is produced by external shocks between the outflow and surrounding material. However, much is still being discovered about the dynamics of jetted outflows, which appear in a variety of astrophysical scenarios and may have more complicated outflow structures, energy conversion processes, and magnetic field effects than are accounted for in this simple internal-external shock scenario. The role of magnetic fields in GRB prompt and afterglow emission is still poorly understood, partly because little is known about the magnetic field strength within the emission sites. Attempts to estimate magnetic field strength from polarization within the GRB prompt emission have so far proven problematic and both theoretical and observational advances are required to improve upon our knowledge here.

Chapter 2

Theory of Jitter Radiation

2.1 Summary

Jitter radiation theory represents a new mechanism of radiation by a charged, ultrarelativistic particle traveling through a region of small-scale magnetic field turbulence. At each point along its path, the particle experiences a transverse acceleration due to the relativistic Lorentz force in a random magnetic field. However, the field's correlation length is sufficiently small that the series of accelerations produces very little deflection of the particle. Consequently, an observer receives a consistent portion of the angular distribution of the particle's emission, which is relativistically beamed in the forward direction. In this chapter we present the general equations for jitter radiation and then develop the equations relevant to the particular geometry representative of the magnetic turbulence generated by the Wiebel-like filamentation instability, with magnetic wavenumber distributions that are independent along and transverse to instability-generated current filamentation.

2.2 General Theory of Jitter Radiation

The Lienard-Weichert equation [Landau and Lifshitz, 1971, Brau, 2004] gives the energy emitted towards an observer in direction $\hat{\mathbf{n}}$ per frequency per unit solid angle by a charged particle moving relativistically along a trajectory $\mathbf{r}(t)$ with velocity $\boldsymbol{\beta}(t) = \mathbf{v}(t)/c$ and acceleration $\dot{\boldsymbol{\beta}}(t) = d\mathbf{v}/cdt$:

$$\frac{d^2W}{d\omega d\Omega} = \frac{e^2}{4\pi^2 c}\left|\int_{-\infty}^{\infty} dt e^{i\omega(t-\hat{\mathbf{n}}\cdot\mathbf{r}/c)} \frac{\hat{\mathbf{n}}\times\left[(\hat{\mathbf{n}}-\boldsymbol{\beta})\times\dot{\boldsymbol{\beta}}\right]}{(1-\hat{\mathbf{n}}\cdot\boldsymbol{\beta})^2}\right|^2 \tag{2.1}$$

This equation takes into account the changing travel time of the radiation as the particle propagates. The radiation received at a time t_{obs} is due to the field produced by the particle at the retarded time $t' = t - \hat{\mathbf{n}}\cdot\mathbf{r}(t)/c)$, where t is the time at the origin of a local inertial reference frame at rest with respect to a distant observer. (Since we are concerned with the evolution of a time signal, the constant time offset in $t_{obs} = t + R/c$ where R is the distance from the observer to the origin of the local frame can be neglected.)

The denominator factor proportional to $(1-\hat{\mathbf{n}}\cdot\boldsymbol{\beta})^4$ means that for ultrarelativistic speeds $\boldsymbol{\beta} \approx 1$ the emission peaks strongly at $\hat{\mathbf{n}} \parallel \boldsymbol{\beta}$, a property known as "relativistic beaming". The particle's deviation relative to the opening angle $1/\gamma$ of the relativistic beaming cone determines whether the observed radiation spectrum will be dominated by particle deflection effects (as in synchrotron radiation) or by variations in the field itself. We can quantify this by defining a deflection parameter δ_{rad} which is the ratio between the angle of deflection $\theta_{defl} = |e|\langle B_\perp\rangle \lambda_B/\gamma mc^2$ and the relativistic beaming cone's opening angle $1/\gamma$. Thus we have

$$\delta_{rad} = \frac{\theta_{defl}}{1/\gamma} = \frac{|e|\langle B_\perp\rangle \lambda_B}{mc^2} \tag{2.2}$$

where $< B_\perp >$ is the average magnetic field strength transverse to the particle's velocity, λ_B is the correlation length of the magnetic field (and hence defines the scale over which the magnetic field varies), m is the particle's mass, and e is the particle's charge. The parameter δ_{rad} is notably independent of the particle's velocity β (or equivalently its Lorentz factor γ).

For $\delta_{rad} \gg \gamma$, we have the synchrotron radiation regime, in which the path length along which a particle's radiation cone is oriented towards a particular direction is much shorter than the correlation length λ_B of the magnetic field. Consequently, the emission received by a particular observed is dominated by intensity variations due to the sweep of the relativistic beaming cone. For $\delta_{rad} \ll 1$, which we designate as the strong (or small-angle) jitter regime, the particle's radiation cone is consistently directed towards a particular direction over a path length much longer than λ_B. In this case, the emission into a particular direction is produced by particles which undergo accelerations but not significant deflections. In the intermediate regime $1 \lesssim \delta_{rad} \lesssim \gamma$, which we designate as the weak (or large-angle) jitter regime, the radiation spectrum is influenced both by the path geometry and the magnetic field distribution. In such a case, the particle is deflected beyond the relativistic beaming angle, but the field geometry along the path segment before this deflection occurs leads to the occurence of low-frequency harmonics that differ from the synchrotron. Figure 2.1 illustrates the differences in the two jitter regimes, with part (a) showing the the weak (large-angle) jitter regime where larger deflections lead to shorter path lengths (highlighted in bold) radiating towards an observer. Part (b) of Figure 2.1 shows the strong (small-angle) jitter regime that has minimal deflection and so a long path length (again highlighted in bold) radiates in the direction of the observer.

In the strong (small-angle) jitter regime, the velocity $\boldsymbol{\beta}$ is nearly constant and the time-dependence of the integrand is contained primarily in the acceleration $\dot{\boldsymbol{\beta}}$. With a

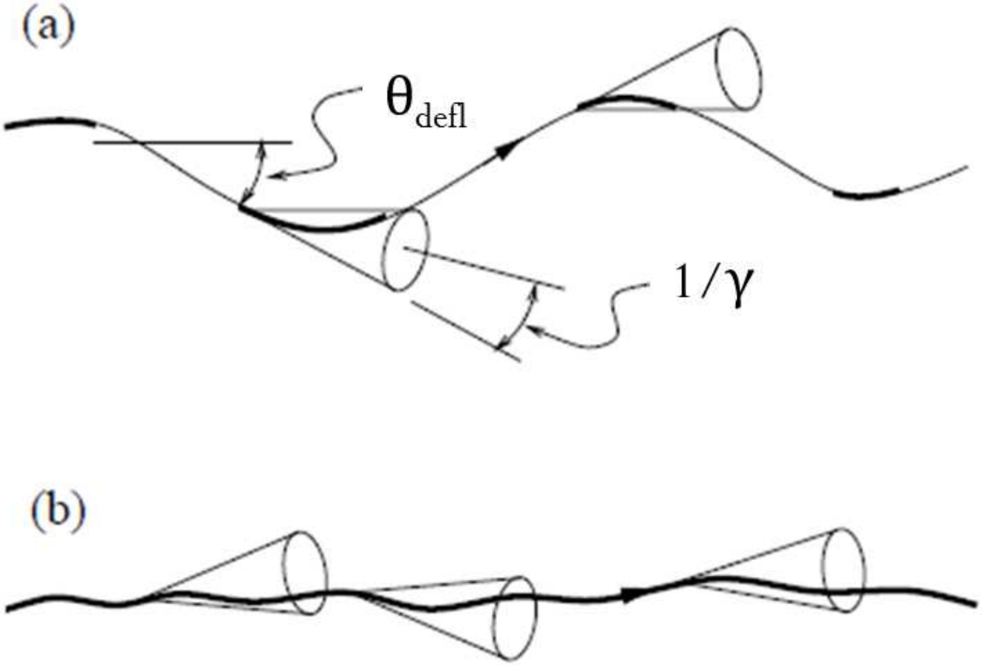

Figure 2.1: (a) In the weak, or large-angle, jitter regime (defined by $1 \lesssim \delta_{rad} \lesssim \gamma$), the deflection of the particle over a field correlation length is approximately equal or slightly larger than the opening angle $1/\gamma$ of the relativistic beaming cone. The radiating path lengths (in bold) seen by an observer are thus of intermediate size, so that the resulting radiation depends both on the intermittency of emission towards the observer and on the variation of the field over those parts of its path for which the particle is correctly oriented. (b) In the strong (or small-angle) jitter radiation regime, the particle's deflection is negligibly small compared to the opening angle $1/\gamma$ of the relativistically beaming angle. Consequently the observer receives radiation from the particle as it moves over a long path, yielding a spectrum that depends upon the magnetic field distribution that accelerates the particle.

constant velocity, the position vector $\boldsymbol{r}(t)$ becomes $\boldsymbol{r}(t) = \boldsymbol{r_0} + c\boldsymbol{\beta}t$. We can then define $\omega' = \omega(1 - \hat{\mathbf{n}} \cdot \boldsymbol{\beta})$, where ω' is the frequency corresponding to the Fourier transform of the particle's acceleration $\boldsymbol{\xi} = \int \dot{\boldsymbol{\beta}} e^{i\omega' t} dt$. Equation 2.1 then becomes:

$$\frac{d^2W}{d\omega d\Omega} = \frac{e^2}{4\pi^2 c} \frac{\left|\hat{\mathbf{n}} \times [(\hat{\mathbf{n}} - \boldsymbol{\beta}) \times \boldsymbol{\xi}]\right|^2}{(1 - \hat{\mathbf{n}} \cdot \boldsymbol{\beta})^2} \tag{2.3}$$

To evaluate this, we define the components of $\boldsymbol{\beta}$ and $\boldsymbol{\xi}$ in the direction $\hat{\mathbf{n}}$ of an observer as $\beta_n = \hat{\mathbf{n}} \cdot \boldsymbol{\beta}$ and $\xi_n = \hat{\mathbf{n}} \cdot \boldsymbol{\xi}$. We define $\beta_\perp$ and $\xi_\perp$ as the magnitudes of the vector projections of $\boldsymbol{\beta}$ and $\boldsymbol{\xi}$ on the plane perpendicular to $\hat{\mathbf{n}}$. The angular spectral fluence becomes:

$$\frac{d^2W}{d\omega d\Omega} = \frac{e^2}{4\pi^2 c} \left[\frac{\xi_n^2 + |\boldsymbol{\xi}|^2}{(1-\beta_n)^2} - \frac{2\xi_n(\xi_n - (\boldsymbol{\beta} \cdot \boldsymbol{\xi}))}{(1-\beta_n)^3} + \frac{\beta_\perp^2 \xi_n^2}{(1-\beta_n)^4} \right] \tag{2.4}$$

The accelerations undergone by the particle, generated by the Lorentz force, will lie in the plane perpendicular to the particle's velocity. Thus, $\boldsymbol{\beta} \cdot \boldsymbol{\xi} = 0$, and the above reduces to:

$$\frac{d^2W}{d\omega d\Omega} = \frac{e^2}{4\pi^2 c} \left[\frac{|\boldsymbol{\xi}|^2}{(1-\beta_n)^2} + \frac{\xi_n^2(\beta^2 - 1)}{(1-\beta_n)^4} \right] \tag{2.5}$$

Where the radiation peaks in the forward direction $\hat{\mathbf{n}} \parallel \boldsymbol{\beta}$, this becomes:

$$\frac{d^2W}{d\omega d\Omega} = \frac{e^2}{4\pi^2 c} \frac{|\xi_\perp|^2}{(1-\beta)^2} \tag{2.6}$$

As it propagates, the particle's acceleration is determined by the underlying magnetic field, so we can relate the Fourier transform of the acceleration $\boldsymbol{\xi}$ to the magnetic field encountered by the particle. At each position, the particle's acceleration $\dot{\boldsymbol{\beta}} = (e\beta/m\gamma)\hat{\boldsymbol{\beta}} \times \mathbf{B}$ due to the Lorentz force is determined by the the local magnetic field vector $\mathbf{B}$ and the particle's velocity $\boldsymbol{\beta}$ at that point.

In the strong jitter regime (hereafter we will operate exclusively within this regime), the particle's velocity is nearly constant in magnitude and direction, so the temporal evolution of the particle's acceleration reflects the particle's propagation along a (nearly) straight-line path through the turbulent magnetic field. Consequently, the time-integral of the particle's acceleration can be translated into an integral over the magnetic field vector distribution along the particle's path. Using the relativistic Lorentz force, we find that

$$\boldsymbol{\xi} = \int \dot{\boldsymbol{\beta}} e^{i\omega' t} dt = \left(\frac{e\beta}{m\gamma}\right) \hat{\boldsymbol{\beta}} \times \mathbf{B}_{\omega'} \tag{2.7}$$

where we have defined $\mathbf{B}_{\omega'} = \int \mathbf{B}(\mathbf{r_0} + c\boldsymbol{\beta} t, t) e^{i\omega' t} dt$. Taking the dot product $\boldsymbol{\xi} \cdot \boldsymbol{\xi^*}$, we obtain

$$\begin{aligned} |\boldsymbol{\xi}|^2 = \xi_i^* \xi^i &= \left(\frac{e\beta}{m\gamma}\right)^2 \left[|\mathbf{B}_{\omega'}|^2 - (\hat{\boldsymbol{\beta}} \cdot \mathbf{B}^*_{\omega'})(\hat{\boldsymbol{\beta}} \cdot \mathbf{B}_{\omega'}) \right] \\ &= \left(\frac{e\beta}{m\gamma}\right)^2 (\delta_{\mu\nu} - \hat{\beta}_\mu \hat{\beta}_\nu) W^{\mu\nu} \end{aligned} \tag{2.8}$$

where we have defined a tensor W whose terms are products of the Fourier spectrum of the magnetic field, $W^{\mu\nu} = \mathbf{B}^{*\mu}_{\omega'} \mathbf{B}^{\nu}_{\omega'}$. We can also take the dot product $\boldsymbol{\xi} \cdot \hat{\mathbf{n}}$ to determine ξ_n and square this to obtain

$$\begin{aligned} \xi_n^2 &= \left(\frac{e\beta}{m\gamma}\right)^2 \left[\mathbf{B}^*_{\omega'} \cdot (\hat{\mathbf{n}} \times \hat{\boldsymbol{\beta}}) \right] \left[\mathbf{B}_{\omega'} \cdot (\hat{\mathbf{n}} \times \hat{\boldsymbol{\beta}}) \right] \\ &= \left(\frac{e\beta}{m\gamma}\right)^2 \left[\delta_{\mu\nu}(1 - (\hat{\boldsymbol{\beta}} \cdot \hat{\mathbf{n}})^2) - \hat{\beta}_\mu \hat{\beta}_\nu - \hat{n}_\mu \hat{n}_\nu - (\hat{\boldsymbol{\beta}} \cdot \hat{\mathbf{n}})(\hat{\beta}_\mu \hat{n}_\nu + \hat{\beta}_\nu \hat{n}_\mu) \right] W^{\mu\nu} \end{aligned} \tag{2.9}$$

Although we are considering the radiation produced by a single particle, we can assume that the field and particle distributions within the radiating region are sufficiently homogeneous that the exact starting position and trajectory of the particle has little effect on the radiation produced. For simplicity, we also assume that the propagation time

Δt_{prop} during which the particle traverses the turbulent field region is much less than the dynamic time scale ΔT of the magnetic field turbulence, allowing us to treat the magnetic field distribution as static. In principle, the radiation produced by the particle at a particular time is dependent only on the local magnetic field accelerating it at that point at its trajectory, so the full field evolution within the radiating volume is not required. (Overall, we are assuming that the distribution of the magnetic field encountered at the particle's position as a function of space and time is roughly equivalent to the statistically-averaged distribution of the static magnetic field within the radiating volume.) With these assumptions, the magnetic field spectrum tensor $W^{\mu\nu}$ becomes

$$W^{\mu\nu} = \left\langle \mathbf{B}^{*\mu}_{\omega'} \mathbf{B}^{\nu}_{\omega'} \right\rangle = (2\pi)^{-3} V^{-1} \int_{-\infty}^{\infty} \mathbf{B}^{*\mu}_{\omega'} \mathbf{B}^{\nu}_{\omega'} \delta(\omega' - c\mathbf{k} \cdot \boldsymbol{\beta}) d^3\mathbf{k} \tag{2.10}$$

Equations 2.5 and 2.10 do not presume any particular geometry of the turbulent magnetic field. These equations determine the jitter radiation spectra for any possible magnetic field distribution that varies on short enough scales to be within the jitter regime. The Weibel-like filamentation instability mechanism can generate such small-scale magnetic field turbulence in both laboratory and astrophysical plasmas. In the following section we consider the magnetic field distribution produced by this instability and incorporate it into our equations.

2.3 Jitter Radiation from the Filamentation Instability

In the magnetic turbulence produced by the Weibel-like filamentation instability, the magnetic field perturbations in the plane transverse to the bulk flow of the counterstreaming particle populations cause the counterstreaming particles to coalesce into filaments. We define the unit vector $\hat{\mathbf{s}}$ as the filamentation axis, the direction of the counterstreaming particle flow and filamentation. The filamentation instability builds magnetic field strength in the plane perpendicular to the filamentation axis $\hat{\mathbf{s}}$, with the resulting magnetic field wavenumbers being randomly oriented within this plane. The random orientations are generated independently at each position along $\hat{\mathbf{s}}$. Consequently, the distribution of magnetic wavenumber along $\hat{\mathbf{s}}$ is independent of the distribution of magnetic wavenumber produced in the plane transverse to $\hat{\mathbf{s}}$.

For such a case, the magnetic field correlation tensor can be written as

$$\mathbf{B}^{*\mu}_{\omega'}\mathbf{B}^{\nu}_{\omega'} = (\delta_{\mu\nu} - \hat{s}_\mu\hat{s}_\nu)\,|\mathbf{B_k}|^2 = C_k(\delta_{\mu\nu} - \hat{s}_\mu\hat{s}_\nu)f_\perp(k_\perp)f_{||}(k_{||}) \tag{2.11}$$

where $f_{||}(k_{||})$ is the distribution of the magnetic wavenumber component parallel to $\hat{\mathbf{s}}$, $f_\perp(k_\perp)$ is the distribution of the magnitude of the projection of the wavevector $\mathbf{k}$ onto the plane transverse to $\hat{\mathbf{s}}$, and C_k is a normalizable constant defined so as to make the wavenumber distributions unitless. Combining this with Equations 2.8, 2.9, and 2.10 and inserting the result into Equation 2.5, we obtain:

$$\begin{aligned}\frac{dW}{d\omega d\Omega} &= \frac{e^2}{4\pi^2 c}G(\hat{\mathbf{s}},\hat{\mathbf{n}},\boldsymbol{\beta})\times \\ &\left[\left(\frac{e\beta}{\gamma m}\right)^2\frac{1}{8\pi^3 V}\int|B_{\mathbf{k}}|^2\delta(\omega(1-\boldsymbol{\beta}\cdot\hat{\mathbf{n}})-c\mathbf{k}\cdot\boldsymbol{\beta})d^3\mathbf{k}\right]\end{aligned} \tag{2.12}$$

where we have defined the geometry and velocity dependent amplitude factor $G(\hat{\mathbf{s}},\hat{\mathbf{n}},\boldsymbol{\beta})$ as

$$G(\hat{\mathbf{s}},\hat{\mathbf{n}},\boldsymbol{\beta}) = \left[\frac{1+(\hat{\mathbf{s}}\cdot\hat{\boldsymbol{\beta}})^2}{(1-\boldsymbol{\beta}\cdot\hat{\mathbf{n}})^2} - \frac{1}{\gamma^2}\frac{(\hat{\mathbf{s}}\cdot\hat{\boldsymbol{\beta}})^2+(\hat{\mathbf{s}}\cdot\hat{\mathbf{n}})^2-2(\hat{\boldsymbol{\beta}}\cdot\hat{\mathbf{n}})(\hat{\mathbf{s}}\cdot\hat{\boldsymbol{\beta}})(\hat{\mathbf{s}}\cdot\hat{\mathbf{n}})}{(1-\boldsymbol{\beta}\cdot\hat{\mathbf{n}})^4}\right] \tag{2.13}$$

We can consider the simplifying geometry in which we choose to view the emission within the plane defined by the filamentation axis and the particle velocity, so that $\hat{\mathbf{s}},\hat{\mathbf{n}}$, and $\hat{\boldsymbol{\beta}}$ lie in the same plane. In this geometry we can define the angle θ between the particle trajectory and the filamentation axis and define the viewing angle α between the particle trajectory and the direction $\hat{\mathbf{n}}$ to the observer. The relationships between the angles and the corresponding vectors can be summarized as follows:

$$\hat{\mathbf{s}} \cdot \hat{\boldsymbol{\beta}} = \cos\theta \tag{2.14}$$

$$\hat{\boldsymbol{\beta}} \cdot \hat{\mathbf{n}} = \cos\alpha \tag{2.15}$$

$$\hat{\mathbf{s}} \cdot \hat{\mathbf{n}} = \cos(\theta + \alpha) \tag{2.16}$$

In this planar case, Equation 2.13 becomes

$$G_{plane}(\beta, \theta, \alpha) = \frac{1 + \cos^2\theta}{(1 - \beta\cos\alpha)^2} - \frac{(1 - \beta^2)\sin^2\alpha}{(1 - \beta\cos\alpha)^4} \tag{2.17}$$

Figure 2.2 shows this factor $G_{plane}(\beta, \theta, \alpha)$ plotted versus α for $\theta = 10^\circ$ and $\beta = 0.99$ and normalized to its value at $\alpha = 0^\circ$. This plot demonstrates the strong relativistic beaming of the emitted radiation into the forward direction.

To solve for the power emitted per solid angle as a function of frequency, we make the substitution $|\mathbf{B_k}|^2 = C_k f_\perp(k_\perp) f_\parallel(k_\parallel)$ from Equation 2.11 into Equation 2.12.

$$\frac{d^2W}{d\omega d\Omega} = \frac{e^4\beta^2}{4\pi^2\gamma^2 m^2 c} \frac{G(\hat{\mathbf{s}}, \hat{\mathbf{n}}, \boldsymbol{\beta})}{8\pi^3 V} \int f_\parallel(k_\parallel) f_\perp(k_\perp) \delta\left(\omega(1 - \boldsymbol{\beta}\cdot\hat{\mathbf{n}}) - c\mathbf{k}\cdot\boldsymbol{\beta}\right) d^2k_\perp dk_\parallel \tag{2.18}$$

Analysis of Equation 2.18 indicates that the radiation spectrum will be determined by the form of the magnetic field distribution encountered by the particle. We shall see that the delta function plays a critical role within the integral in determining the relative influence of the two different magnetic field distributions for different particle paths and viewing angles.

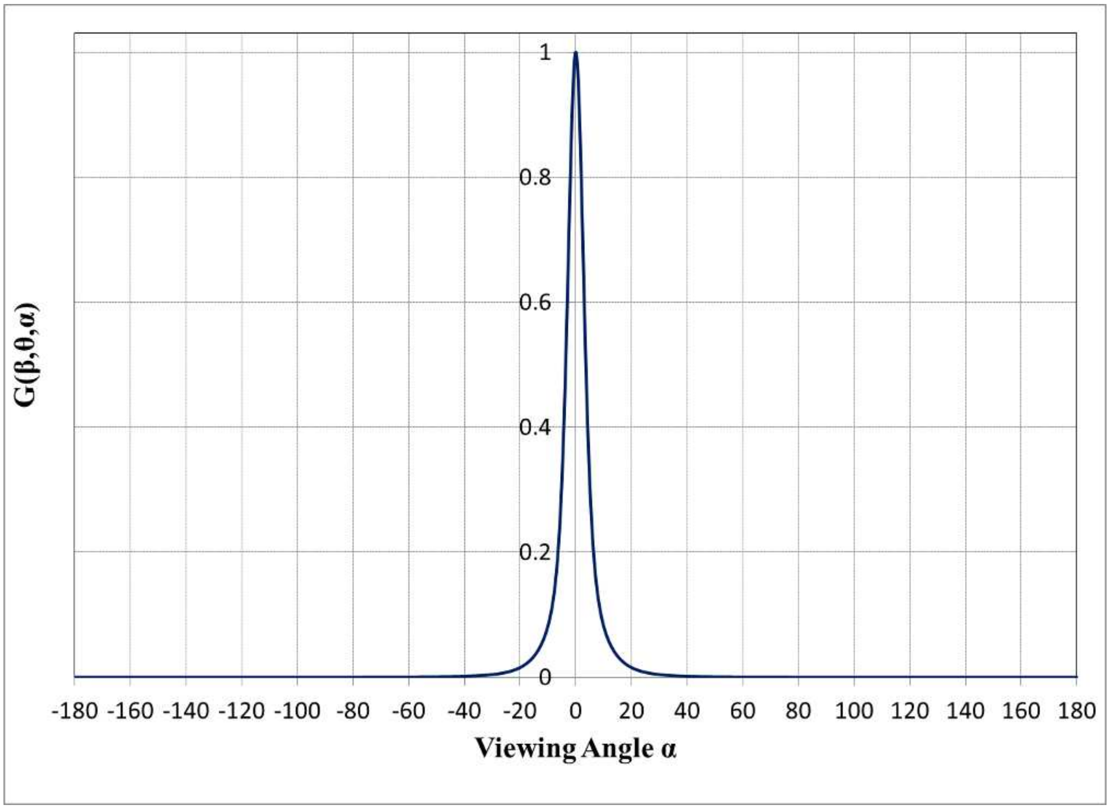

Figure 2.2: The geometry-dependent amplitude factor $G_{plane}(\beta, \theta, \alpha)$ for varying viewing angles α as measured from the particle's velocity $\boldsymbol{\beta}$ in the same plane as both $\boldsymbol{\beta}$ and the filamentation axis $\hat{\mathbf{s}}$. Here we have used values of particle speed $\beta = 0.99$ and angle $\theta = 10^\circ$ between the particle's velocity and the filamentation axis $\hat{\mathbf{s}}$. The vertical axis is normalized to the value at $\alpha = 0$ (that is, $G_{plane}(0.99, 10^\circ, \alpha)/G_{plane}(0.99, 10^\circ, 0^\circ)$).

The transverse magnetic field distribution $f_\perp(k_\perp)$ generated by the Weibel-like filamentation instability has been explored analytically [Medvedev and Loeb, 1999] and through plasma simulations [Frederiksen et al., 2004]. The exact characterization of the distribution and the parameters influencing it are not fully developed, but it has been shown to rise and then drop after a scale of order the plasma skin depth. The field distribution $f_\|(k_\|)$ along the filamentation axis is even less well known in principle, but we choose here to assume that it has a similar form. For our field distributions, we use

$$f_\perp(k_\perp) = \frac{k_\perp^{2a_\perp}}{\left(\kappa_\perp^2 + k_\perp^2\right)^{a_\perp + b_\perp}}, \tag{2.19}$$

and

$$f_\|(k_\|) = \frac{k_\|^{2a_\|}}{\left(\kappa_\|^2 + k_\|^2\right)^{a_\| + b_\|}}, \tag{2.20}$$

where the free parameters κ, a, and $b > 0$ control the spectral break and the soft and hard spectral indices, respectively.

The basic asymptotic behavior of these equations for the magnetic field distributions is

$$f(k_p) \propto \begin{cases} k_p^{2a_p}, & \text{if } k_p << \kappa_p, \\ k_p^{-2b_p}, & \text{if } k_p >> \kappa_p. \end{cases} \tag{2.21}$$

where p is simply a reference index indicating either the parallel or perpendicular component of wavenumber. The factors of 2 within the powers of k_p are to keep $f_p(k_p)$ as positive definite. Since a_p can in principle take on values which result in $2a_p$ having an odd value, it is important in implementing this equation within numerical calculation to ensure that the numerator is either evaluated as $(k_p^2)^{a_p}$ or as $|k_p|^{2a_p}$.

Our field spectra (Equations 2.19 and 2.20) are defined so as to make variables k and κ dimensionless values, expressed in terms relative to a wavenumber unit k_0. This will result in a normalizable factor $B_{p0}k_0^{-2b_p}$ contributed to Equation 2.18 by each spectral distribution, From the delta function in Equation 2.18 this means our frequencies will be defined in terms of units $\omega_0 = ck_0$.

2.4 Angular Dependence of Jitter Radiation

For calculation purposes, we define a Cartesian coordinate system in which the current filamentation axis $\hat{\mathbf{s}}$ lies along the z-axis and the magnetic field is randomly oriented in the transverse xy-plane. The independent magnetic field wavenumber components in the directions along and transverse to the filamentation axis are then $k_{\parallel} = k_z$ and $k_{\perp} = (k_x^2 + k_y^2)^{1/2}$. We can rewrite the delta function in Equation 2.18 to isolate one of the three wavenumber components. The integral of the delta function then allows a substitution to be made for that wavenumber component as a function of the other variables within the delta function. Because the wavenumber within the delta function comes in via the dot product $\mathbf{k} \cdot \boldsymbol{\beta}$, and $\mathbf{k}$ is defined in terms of components along or transverse to $\hat{\mathbf{s}}$, the angle θ between $\hat{\mathbf{s}}$ and $\boldsymbol{\beta}$ modifies the effect of different components of the wavevector.

The delta function in Equation 2.18 can be written in terms of $\omega' = \omega(1 - \boldsymbol{\beta} \cdot \hat{\mathbf{n}}) = \omega(1 - \beta \cos \alpha)$:

$$\delta(\omega(1 - \boldsymbol{\beta} \cdot \hat{\mathbf{n}}) - c\boldsymbol{k} \cdot \boldsymbol{\beta}) = \delta(\omega' - c\boldsymbol{k} \cdot \boldsymbol{\beta}) \tag{2.22}$$

In the cases where the particle velocity $\boldsymbol{\beta}$ is aligned directly along ($\theta = 0^\circ$) or transverse ($\theta = 90^\circ$) to the filamentation axis $\hat{\boldsymbol{s}}$ (which we have defined as the z-axis in our geometry) the term $\boldsymbol{k} \cdot \boldsymbol{\beta}$ within the delta function in Equation 2.22 reduces to a function of a single component of k (we choose the x-axis so that $\boldsymbol{\beta}$ lies within the xz-plane).

The integral over the delta function then reduces to a simple substitution for k_x or k_z as a function of ω, θ, and β.

For the case of velocities along the filamentation axis ($\boldsymbol{\beta} \parallel \hat{\mathbf{z}}$), we obtain $\mathbf{k} \cdot \boldsymbol{\beta} = k_z \beta$, which yields

$$\delta(\omega' - ck_z\beta) = \frac{1}{|c\beta|}\delta\left(k_z - \frac{\omega}{c\beta}(1 - \beta\cos\alpha)\right) \tag{2.23}$$

This leads to:

$$\begin{aligned}&\int_{-\infty}^{\infty} f_\perp(k_\perp) f_\parallel(k_\parallel)\delta(\omega' - c\mathbf{k}\cdot\boldsymbol{\beta})d^3\mathbf{k} \\ &= f_\parallel(\omega'/c\beta)\int_{-\infty}^{\infty}\int_{-\infty}^{\infty} f_\perp((k_x^2 + k_y^2)^{1/2})dk_x dk_y\end{aligned} \tag{2.24}$$

Consequently, we find that the spectrum produced by particles moving parallel to the filamentation axis is directly dependent on the distribution of the magnetic field wavenumber along this axis,

$$\frac{dW}{d\omega d\Omega} \propto f_\parallel(\omega'/c\beta) \tag{2.25}$$

On the other hand, if we consider velocities transverse to the filamentation axis (meaning $\boldsymbol{\beta} \parallel \hat{\mathbf{x}}$ in our chosen geometry), then $\mathbf{k}\cdot\boldsymbol{\beta} = k_x\beta$ and we obtain

$$\delta(\omega' - ck_x\beta) = \frac{1}{|c\beta|}\delta\left(k_x - \frac{\omega'}{c\beta}\right) \tag{2.26}$$

which leads to

$$\begin{aligned}&\int_{-\infty}^{\infty} f_\perp(k_\perp) f_\parallel(k_\parallel)\delta(\omega' - c\mathbf{k}\cdot\boldsymbol{\beta})d^3\mathbf{k} \\ &= \frac{1}{c|\beta|}\int_{-\infty}^{\infty}\int_{-\infty}^{\infty} f_\perp(((\omega'/c\beta)^2 + k_y^2)^{1/2}) f_\parallel(k_z)dk_y dk_z\end{aligned} \tag{2.27}$$

The integral over k_z will produce a constant, so we find that for the case of particles moving transverse to the filamentation axis, the jitter radiation spectrum is directly dependent on the form of the distribution of the transverse magnetic field wavenumber components:

$$\frac{dW}{d\omega d\Omega} \propto \int_{-\infty}^{\infty} f_{\perp}(((\omega'/c\beta)^2 + k_y^2)^{1/2}) dk_y \tag{2.28}$$

In both limiting cases we obtain a spectrum whose frequency dependence is determined only by the distribution of the magnetic field along (for $\theta = 0°$) or perpendicular (for $\theta = 90°$) to the filamentation axis.

For a more general orientation of the beam at some angle $0° < \theta < 90°$ relative to the filamentation axis, the substitution for k_x or k_z includes the other wavenumber component and the frequency dependence of the resulting spectrum is influenced by both magnetic field distributions. Particle velocities at an oblique angle θ from $\hat{\mathbf{s}}$ (we again select the x-axis so that β lies in the xz-plane) lead to $\mathbf{k} \cdot \boldsymbol{\beta} = k_x \beta \sin\theta + k_z \beta \cos\theta$. The delta function then allows substitution for either k_x or k_z:

$$\begin{aligned} & \delta(\omega' - ck_x\beta\sin\theta - ck_z\beta\cos\theta) && (2.29) \\ = \; & \frac{1}{|c\beta\cos\theta|}\delta\left(k_z - \frac{\omega'}{c\beta\cos\theta} - k_x\tan\theta\right) \\ = \; & \frac{1}{|c\beta\sin\theta|}\delta\left(k_x - \frac{\omega'}{c\beta\sin\theta} - k_z\cot\theta\right) \end{aligned}$$

$$(2.30)$$

The substitutions for k_x or k_z lead to

$$
\begin{aligned}
&\textstyle\int_{-\infty}^{\infty} f_\perp(k_\perp) f_\parallel(k_\parallel)\delta(\omega' - c\mathbf{k}\cdot\boldsymbol{\beta})d^3\mathbf{k} \\
&= \tfrac{1}{|c\beta\cos\theta|}\textstyle\int_{-\infty}^{\infty}\int_{-\infty}^{\infty} f_\perp((k_x^2+k_y^2)^{1/2}) f_\parallel\left(\frac{\omega'}{c\beta\cos\theta} + k_x\tan\theta\right)dk_x dk_y \qquad (2.31)\\
&= \tfrac{1}{|c\beta\sin\theta|}\textstyle\int_{-\infty}^{\infty}\int_{-\infty}^{\infty} f_\perp\left(\left(\left(\frac{\omega'}{c\beta\sin\theta} + k_z\cot\theta\right)^2 + k_y^2\right)^{1/2}\right) f_\parallel(k_z)dk_y dk_z \qquad (2.32)
\end{aligned}
$$

For a single radiating particle, we can plug Equations 2.19 and 2.20 for $f_\perp$ and $f_\parallel$ into Equation 2.31 to obtain:

$$
\frac{dW}{d\omega d\Omega} = \frac{C\eta_1(\theta)G(\hat{\mathbf{s}},\hat{\mathbf{n}},\boldsymbol{\beta})}{|\beta|}\int_{-\infty}^{\infty}\int_{-\infty}^{\infty}\frac{(k_x^2+k_y^2)^{a_\perp}}{(\kappa_\perp^2+k_x^2+k_y^2)^{b_\perp}}\frac{(\frac{\omega'}{c\beta\sin\theta}+k_x)^{2a_\parallel}}{(\kappa_\parallel^2\cot^2\theta+(\frac{\omega'}{c\beta\sin\theta}+k_x)^2)^{a_\parallel+b_\parallel}}dk_x dk_y \tag{2.33}
$$

where we have combined constant factors into a single constant C and have defined the θ-dependent factor

$$
\eta_1(\theta) = \frac{(\tan\theta)^{-2b_\parallel}}{|\cos\theta|} \tag{2.34}
$$

Alternatively, if we put Equations 2.19 and 2.20 into Equation 2.32, we obtain

$$
\begin{aligned}
\frac{dW}{d\omega d\Omega} &= \frac{C\eta_2(\theta)G(\hat{\mathbf{s}},\hat{\mathbf{n}},\boldsymbol{\beta})}{|\beta|} \qquad (2.35)\\
&\times\int_{-\infty}^{\infty}\int_{-\infty}^{\infty}\frac{((\frac{\omega'}{c\beta\cos\theta}+k_z)^2+k_y^2\tan^2\theta)^{a_\perp}}{\left(\kappa_\perp^2\tan^2\theta+(\frac{\omega'}{\beta\cos\theta}+k_z)^2+k_y^2\tan^2\theta\right)^{a_\perp+b_\perp}}\frac{k_z^{2a_\parallel}}{(\kappa_\parallel^2+k_z^2)^{a_\parallel+b_\parallel}}dk_y dk_z
\end{aligned}
$$

where

$$
\eta_2(\theta) = \frac{(\cot\theta)^{-2b_\perp}}{|\sin\theta|} \tag{2.36}
$$

The two forms are equivalent; however, as we approach $\theta = 0$ or $\theta = \pi/2$, the calculation is more convenient if one avoids denominators approaching zero by choosing the appropriate form. In our calculation, we use Equation 2.33 for angles $\pi/4 \leq \theta < \pi/2$

and Equation 2.35 for angles $0 < \theta \leq \pi/4$. Neither form is valid for the endpoints $\theta = 0$ or $\theta = \pi/2$, as the delta function substitutions at those values must be treated separately as above.

An analysis of equations (2.33) and (2.35) indicates that ω' functions as a shift of the center of the magnetic spectral form in which we have made the delta-function substitution. Since this ω' factor is always positive, the function's offset always occurs in the direction of negative wavenumber components k_x or k_z. An example of this behavior for the product of two functions such as equations (2.19) and (2.20) over a range of offsets is shown in Figure 2.3. The resulting integral is highly sensitive to the shape of the two functions and the offset between them, which control the resonance like behavior that produces the resulting peak and transition points in the spectrum. The angle θ plays a role in determining both the width and the offset of one function relative to the other: the $\kappa_{\|}^2 \cot^2\theta$ or $\kappa_{\perp}^2 \tan^2\theta$ terms in the denominator influence the width of the function under consideration, while the offset is given by $\frac{\omega'}{c\beta\cos\theta}$ or $\frac{\omega'}{c\beta\sin\theta}$. These are linked such that as θ increases, both the width and the offset of the function containing θ increases. The spectral indices $a_{\perp}$, $a_{\|}$, $b_{\perp}$, and $b_{\|}$ can also influence the width of the functions and hence also affect the location of the transition points in the acceleration spectra. The overall effect of such variations on the resulting jitter radiation spectrum will be explored more in Chapter 4.

We can see from the jitter radiation spectrum's dependence on $\omega' = \omega(1-\beta\cos\alpha)$ that the viewing angle α between $\boldsymbol{\beta}$ and the direction $\hat{\mathbf{n}}$ to the observer functions primarily as a shift of the radiation spectrum's distribution in frequencies, proceeding from $\omega' = \omega(1-\beta)$ for $\hat{\mathbf{n}} \parallel \boldsymbol{\beta}$ to $\omega' = \omega$ for $\hat{\mathbf{n}} \perp \boldsymbol{\beta}$. With a series of small-angle substitutions, we find that $\omega' = \omega(1-\beta\cos\alpha) \approx \omega/2(\alpha^2+\gamma^{-2})$. The integration over solid angle $d\Omega \approx \alpha d\alpha d\phi$ can then be converted to an integration over $d\phi d\omega'/\omega$ and integrate over

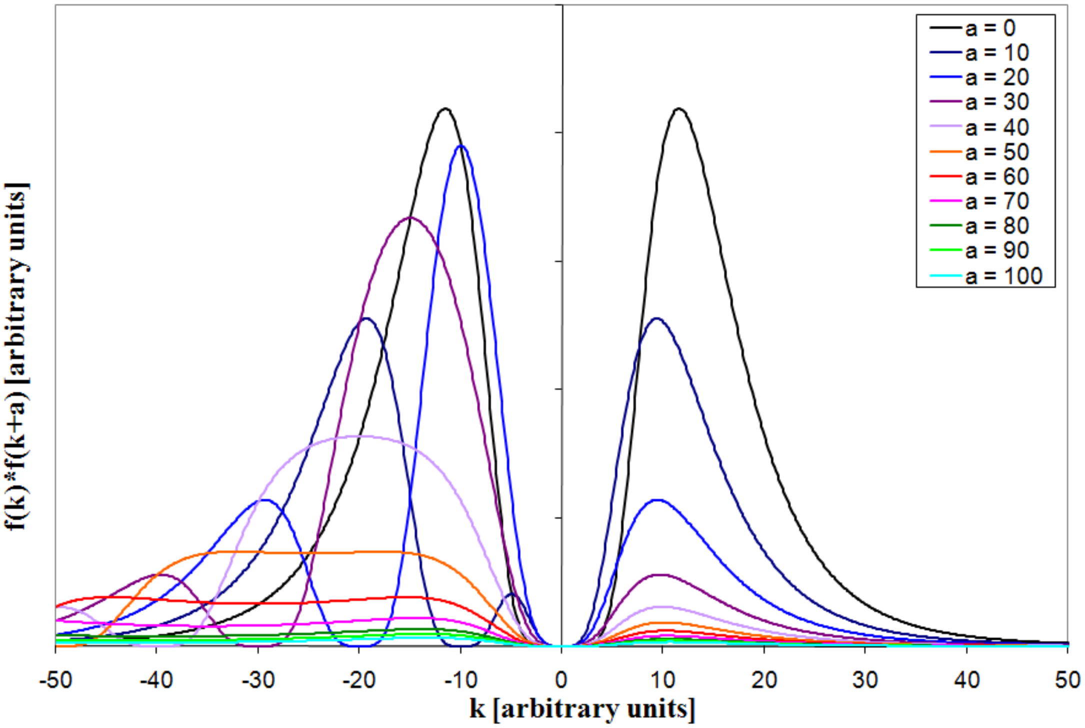

Figure 2.3: Plots of the product $f(k)f(k+a)$ of two functions of the form of our magnetic field spectra (Equations (2.19) and (2.20, illustrating the effect of the offset a. As discussed, the angle-resolved jitter radiation spectrum is the integral of a product of such functions, with an offset controlled by ω', β, and θ.

ϕ to obtain the angle-averaged emission:

$$\frac{dW}{d\omega} = \frac{2\pi e^2}{c^3 \omega} \int_{\omega/2\gamma^2}^{\infty} |\boldsymbol{\xi}|^2 \left(1 - \frac{\omega}{\omega' \gamma^2} + \frac{\omega^2}{2\omega'^2 \gamma^4}\right) d\omega' \tag{2.37}$$

Solving this using $|\boldsymbol{\xi}|^2$ and the independent magnetic field distributions $f_\perp(k_\perp)$ and $f_{||}(k_{||})$ as in the previous section, we obtain

$$\begin{aligned} \frac{dW}{d\omega} &= C_{av}\left(1+\cos^2\theta\right) \int_{\omega/2\gamma^2}^{\infty} \left(\int f_{||}(k_z) f_\perp((k_x^2+k_y^2)^{1/2}) \delta\left(\omega' - c\mathbf{k}\cdot\boldsymbol{\beta}\right) dk_x dk_y dk_z \right) \\ &\quad \times \left(1 - \frac{\omega}{\omega'\gamma^2} + \frac{\omega^2}{2\omega'^2\gamma^4}\right) d\omega' \end{aligned} \tag{2.38}$$

where C_{av} is a normalizable constant.

The delta function operates as in the angle-resolved case to replace either the k_x or k_z component within the integrand. The ω-dependence of the lower integration limit in $\omega\prime$ means that we are effectively integrating over changing portions of the angle-resolved spectral distribution. We will explore this further in Chapters 3 and 4 as we look at the results of numerical calculations of both the angle-averaged and angle-resolved spectra.

2.5 Discussion of Results

We have seen that because of relativistic beaming, the radiation observed from a relativistic particle is strongly influenced by the particle's deflection relative to the opening angle $1/\gamma$ of the cone into which the bulk of its radiation is emitted (around the particle's forward direction). Magnetic fields with sufficiently long correlation lengths result in large-angle deflections of the particle, producing radiation in the synchrotron regime as the emission from the gyrating particle sweeps back and forth relative to a given line of sight. For the strong (small deflection angle) jitter regime, particles moving in magnetic fields with extremely short correlation lengths are accelerated but not substantially deiated, so that an observer consistently receives radiation over a long path length, with the spectrum of that radiation depending on the magnetic field variations the particle encounters. For intermediate ranges in the weak (large deflection angle) jitter regime, the particles are deflected but over sufficiently long scales that the radiation spectrum obtained is determined both by particle deflection and by magnetic field variation.

The jitter radiation spectral power per frequency per unit solid angle depends directly upon the Fourier spectrum of accelerations undergone by the particle, which depends via the relativistic Lorentz force on the distribution of magnetic field. We have developed the relevant equations in general in Section 2.2 and in the particular context of the magnetic field turbulence by the Weibel-like filamentation instability in Section 2.3. In the instability, the filamentation axis defines an anisotropy in the field distribution, such that the magnetic wavenumber distributions are independent along and transverse to this axis.

The resulting equations for the jitter radiation spectrum produced by particles propagating through field turbulence created by the Weibel-like filamentation instability are explicitly dependent on the angle the particle's path makes relative to the filamentation axis. Particles moving along the filamentation axis produce a jitter radiation spectrum proportional to the distribution of the magnetic wavenumber component along the axis. Consequently, the radiation obtained from such particles will contain crucial information about the form of this magnetic field distribution. As $f_{\|}(k_{\|})$ is thus far largely unknown for such a system, jitter radiation studies could provide valuable insight into this aspect of the field. Particles moving transverse to the filamentation axis produce a spectrum proportional to the transverse field distribution $f_{\perp}(k_{\perp})$ integrated over the magnetic wavenumber component that is transverse to both the viewing direction and the filamentation axis. The integration over the second wavenumber component in the transverse case results in a flattening of the spectrum at low-frequencies, which makes it observationally distinct from the spectrum produced by particles moving along the filamentation axis. Particles moving at oblique angles between these two cases will have spectrum with a mixed dependence on the transverse and parallel magnetic field distributions; however, as we shall see in Chapter 5, spectral differences in the two magnetic field distributions can cause one or the other to dominate the spectrum produced at intermediate angles.

The radiation produced by particles with a particular velocity orientation $\hat{\boldsymbol{\beta}}$ relative to the filamentation axis $\hat{\mathbf{s}}$ thus depends upon the angle θ between $\hat{\boldsymbol{\beta}}$ and $\hat{\mathbf{s}}$. Furthermore, the angular distribution of radiation produced by those particles is strongly peaked in the forward direction, where viewing angle α between the particle velocity $\boldsymbol{\beta}$ and the direction to the observer $\hat{\mathbf{n}}$ is small. Consequently, even with a radiating particle population that is isotropic in velocity space, the radiation received by an observer at a specific viewing angle Θ relative to the filamentation axis will be dominated by contributions from the particles moving in that direction (with $\theta = \Theta$). Consequently, the jitter radiation spectrum may vary widely in form depending on an observer's viewing angle with respect to the filamentation axis in the radiating region, regardless of the radiating particle distribution. This, as well as the lack of a low-energy spectral index limit, is distinct from the synchrotron case.

Chapter 3

Laboratory Applications of Jitter Radiation

3.1 Summary

The development of high-energy density laboratory plasmas has led to exciting new possibilities for laboratory astrophysics, as such plasmas can be generated in controlled laboratory conditions yet appear to scale well for comparison with the underlying physics in high-energy astrophysical events. The Weibel-like filamentation instability may be generated through laser-plasma interactions in order to study dynamics of small-scale magnetic field turbulence that are significant for both astrophysical and laboratory plasmas. In this chapter we develop the relevant jitter radiation theory for such laboratory experiments and explore the effect of variations in the magnetic field distribution upon the jitter radiation spectrum produced by particles moving through the turbulent region.

3.2 Studying the Weibel-Like Filamentation Instability in Laboratory Laser-Plasmas

Filamentary structures have long been observed in laboratory plasma experiments, often problematically, as filamentation can disrupt inertial confinement fusion (ICF) and degrade the quality of laser and beam applications. While plasma density filamentation may be easily observed in a variety of scenarios, such filamentation has yet to be reliably studied with the simultaneous particle density, particle flow, and magnetic field measurements that would be necessary to fully characterize the filamentary structures. Understanding the instabilities leading to the formation of these filaments and the processes governing their behavior once formed could have valuable applications for the improvement of ICF and high-energy laser-plasma interactions. Furthermore, as we have discussed in Chapter 1, such filamentation may play a significant role in a variety of astrophysical plasma scenarios, including magnetic reconnnection, particle acceleration at shocks, and astrophysical jet structure. Consequently, we may be able to gain valuable insight into high-energy density plasma physics relevant across a variety of scales by exploring filamentation instabilities in the laboratory.

The Weibel-like filamentation instability, which has been extensively studied in particle-in-cell (PIC) simulations (see Silva et al. [2003], Frederiksen et al. [2004], Nishikawa et al. [2009], Chang et al. [2008] for instance), may be responsible for generating near equipartition strength magnetic field turbulence within collisionless plasmas. Originating in counterstreaming particle motion, this instability was originally considered primarily as a source of filamentation at or immediately upstream from a propagating shock front. More recent studies have shown that this instability may operate in a wider variety of contexts, arising at various sites of interpenetrating plasma flow, at sites of plasma injection or outflow from magnetic reconnection or other processes, and in non-shock plasmas with an appopriate anisotropy in particle velocity distributions.

Jitter radiation, with its particular sensitivity to magnetic field distribution and field anisotropy, is the appropriate radiation mechanism for relativistic particles in a small-scale turbulent region such as produced by the Weibel-like filamentation instability. Consequently, jitter radiation can provide a powerful, minimally-invasive diagnostic for the magnetic field distribution in such regions.[Reynolds and Medvedev, 2012]

A typical laboratory laser-plasma experiment creates a plasma by focusing a high-energy laser on a solid target within a chamber. For studies of the (Weibel-like) filamentation instability, an electron beam or strong laser beam can produce anisotropy in the plasma distribution function (PDF), which then drives the instability. The PDF anisotropy is produced in the direction parallel to the impinging beam, and this direction will become the axis along which current filaments form. Once the filaments form, jitter radiation will be produced by the plasma particles moving in the resulting small-scale turbulent magnetic fields of the filaments. This radiation, which will be strongly peaked in the forward direction of the impinging beam and the resulting filamentation axis, can be used to diagnose properties of the magnetic field distribution. Such diagnostics, making use of the radiation inherently produced by the plasma particles, have a distinct advantage in allowing properties of the magnetic field within the instability to be explored without the use of *in situ* probes that might otherwise disrupt or alter the instability itself.

As we have seen, the spectrum of jitter radiation is strongly dependent on the orientation of the radiating particle population compared to any strong field anisotropies. In our filamentation instability case, we showed the jitter radiation spectrum depends strongly on the angle θ between the radiating particles' velocity $\boldsymbol{\beta}$ and the filamentation axis $\hat{\mathbf{s}}$. In the scenario just described, the dynamics of the instability are such that the bulk of the particle population will be moving along the filamentation axis or in directions a very small angle from it. The jitter radiation produced as a result will thus reflect only a very small range of $\theta \approx 0$. As our analysis in Chapter 2 Section 2.4 demonstrated, the jitter radiation spectrum produced for $\theta = 0$ depends directly upon the parallel magnetic field distribution (that is, the distribution along the filamentation axis $\hat{\mathbf{s}}$) and is uninfluenced by the transverse magnetic field distribution. Thus, the transverse magnetic field distribution cannot be well-explored using the jitter radiation produced by particles from the instability-generating beam.

Alternatively, a second, lower-intensity, electron beam could be used to "probe' the filamentation instability region from a wider range of directions, generating jitter radiation from electrons moving at the angle $\theta = \Theta_{probe}$ relative to the filamentation axis. While this scenario is more challenging in terms of experimental design and engineering, it can provide a much more powerful diagnostic in its varying sensitivity to particular components of the magnetic field distribution. Furthermore, the energy distribution of the radiating particle population can be better controlled in this scenario.

Recent years have seen the development and improvement of a technique for generating quasi-monoenergetic relativistic electron beams using laser wake field acceleration.[Mangles et al., 2004, Geddes et al., 2004, Faure et al., 2004, 2006, Nakamura et al., 2007, Malka et al., 2008, Osterhoff et al., 2008, Lindau et al., 2008, Pollock et al., 2011] Such beams would be useful in minimizing particle energy distribution effects on our jitter radiation spectrum, allowing for better characterization of the magnetic field itself. The electron energy distribution in such beams is roughly Gaussian and can be characterized by a peak energy and a full-width-at-half-maximum (FWHM). For our calculations for radiating beams in sections 3.3.2 and 3.3.3, we have chosen our radiating particle population to have modest representative values for a quasi-monoenergetic electron beam, with peak energy of 200 MeV and a full-width at half maximum of 50

MeV. The radiation produced, either by the instability-generating beam or by a separate probe beam, would be best detected near the peak of the radiation emission at $\alpha = 0^\circ$, which will be in the forward direction along the axis of the radiating beam. The electron beam itself could be deflected, using a large scale magnetic field outside the instability region, to avoid impingement on the radiation detector.

3.3 Jitter Radiation Spectral Solutions for Laboratory Scenarios

3.3.1 Solutions for a single particle energy

From Chapter 2, we recall that the angle-resolved jitter radiation spectrum depends upon the Fourier transform of the accelerations undergone by the particle as it propagates through the region of small-scale magnetic field turbulence (see Equation 2.5). From this, we used the anisotropy inherent in filamentation to develop an equation for the power emitted per frequency per unit solid angle in terms of separate magnetic field distributions along and transverse to the filamentation axis (Equation 2.18). We then used two-power law forms (Equations 2.20 and 2.19) for both our parallel and transverse magnetic field wavenumber distributions to obtain Equations 2.33 and 2.35 for the angle-resolved emission spectrum in terms of parameters controlling the low-wavenumber and high-wavenumber spectral index of each field distribution as well as the "break" or transition point between them. As noted in section 2.4, Equations 2.33 and 2.35 are equivalent but vary in calculation difficulty as they approach the limits $\theta = 0$ and $\theta = \pi/2$.

We present here calculated solutions for the angle-resolved emission spectrum produced by a single particle energy, neglecting particle distribution effects other than the statistical consistency of particles moving in a certain direction θ relative to the filamentation axis $\hat{\mathbf{s}}$ (e.g., we have assumed that the rate of propagating particles being eventually deflected beyond a small angle from a certain path is approximately equivalent to the rate of particles being deflected into a small angle from this particular path). In this section we show results for varying θ between the radiating beam and a constant α at which the radiation is detected relative to this beam. The viewing angle α relative to the beam may be simply taken as 0, but since we have demonstrated that the effect of α is to produce a shift in the frequency dependence and the amplitude of the spectral shape, we have presented our results as functions of the frequency ω', where $\omega' = \omega(1-\beta\cos\alpha)$. For the case $\alpha = 0$, this means $\omega' = \omega(1-\beta)$. Since we are then effectively looking at a single angle α, we have normalized our data here to neglect the α dependence of the amplitude (it may be easily reintroduced by including the factor $A(\alpha)$).

We have selected arbitrary-yet-reasonable values for our magnetic field parameters, based on the spectral indices seen in GRB spectrum and in PIC simulations of Weibel-like filamentation. For simplicity, we have chosen the same parameters for the field distributions parallel and transverse to the filamentation axis, with

$$\kappa_{\parallel} = \kappa_{\perp} = 10, \tag{3.1}$$

$$a_{\parallel} = a_{\perp} = 2, \tag{3.2}$$

$$b_{\parallel} = b_{\perp} = 1.5; \tag{3.3}$$

In Figure 3.1, we present the numerically-calculated results for varying θ, the angle between the particle's direction of motion $\boldsymbol{\beta}$ and the filamentation axis $\hat{\mathbf{s}}$ in Figure 3.1. Figure 3.2 shows the same results, but focuses in greater detail on the critical region around the peak of the spectrum. The graphs show linearly-connected $\ln - \ln$ data, with

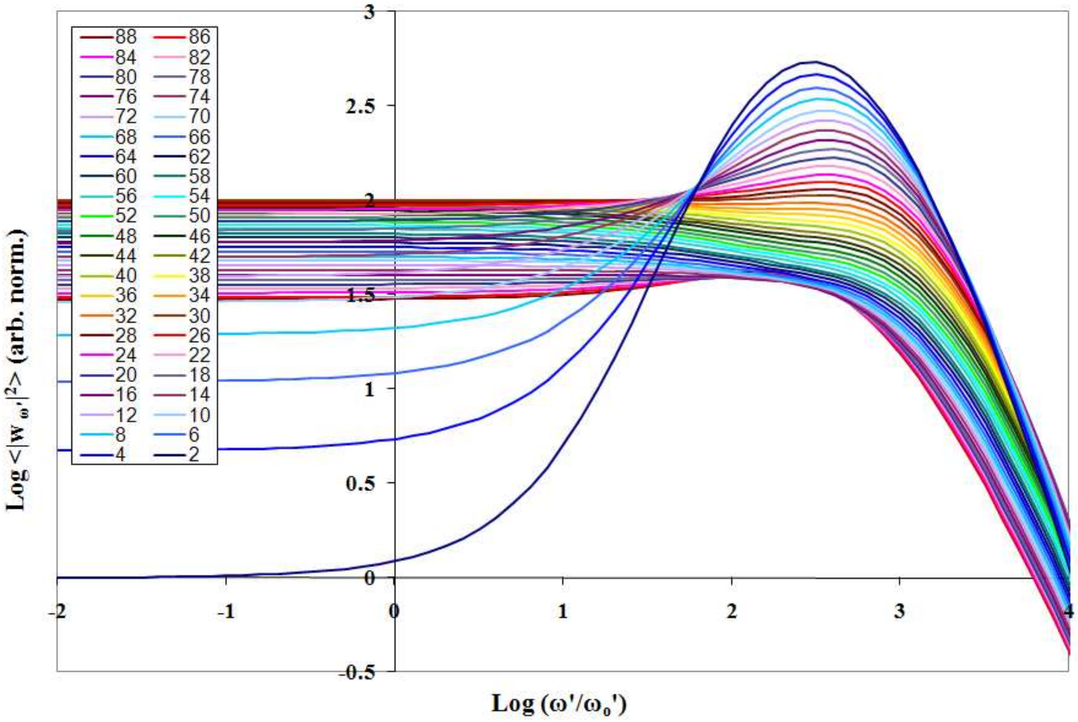

Figure 3.1: The angle-resolved jitter radiation spectra for θ ranging from 2 through 88 degrees. The spectrum is numerically calculated for a step size of 0.1 in $\log_e(\omega')$ and is normalized via division by the 3-dimensional integral over the magnetic field spectra.

data point intervals of 0.1 in $\ln(\omega)$. (Unless specified otherwise all log functions in this thesis are in base *e*.) We have arbitrarily normalized the spectra here so that the low-*k* part of the $\theta = 2^\circ$ spectrum asymptotes at unity. The resulting spectra are flat for low ω', then at a certain ω' they turn rapidly into a sloped region, then there is a second transition to a steep decline for high ω'. For θ near 0 the spectra have a clear peak, but as θ increases the peak recedes and eventually disappears altogether. As θ approaches $\pi/2$ a peak again becomes evident but the location of the peak has shifted by about 0.4 from its position for low θ. The transition point for flattening at low ω' appears to move off rapidly to lower ω' as θ approaches 0.

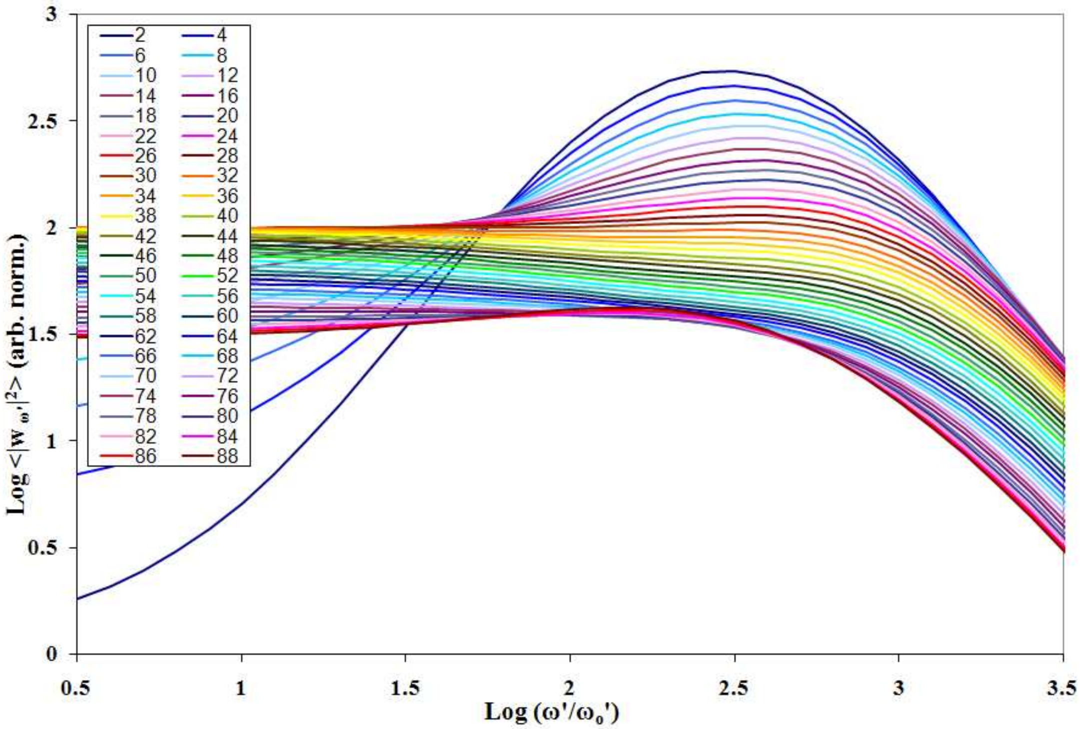

Figure 3.2: View showing detail of peak region of the angle-resolved jitter radiation spectra shown in Figure 3.1. One can see the disappearance of the peak and flattening of the spectra for mid-range θ, followed by its reappearance at slightly lower $\log(\omega')$ at θ of about 76 degrees.

Figure 3.3 plots the amplitude of the jitter radiation spectrum at our lower calculation boundary, at the approximate location of the peak for small θ, and at the approximate location of the peak for θ close to $\pi/2$. The crossing of the lines on this graph correspond to spectral transitions as the peak disappears and then eventually reappears at a new location for higher θ. The graph of the slope of the $\log - \log$ plot in Figure 3.4 also illustrates the disappearance and reemergence of the peak, but further shows that even for the unpeaked spectra there is a flattening of the slope of the mid-range θ spectra in the region in between the positions of the peaks that appear at higher and lower θ. For unpeaked spectra, there remains a transition region of some extent between the low-frequency and high-frequency power laws; consequently, the unpeaked spectra may still be better fit by division into three power law regions as opposed to two.

Summarizing the results of this section, we find that the angle-resolved jitter radiation spectra are generally characterizable to a good approximation by division into three regions: a flat low-k region and two power law regions, as shown in Figure 3.5. These may altogether be described via one amplitude, two non-zero spectral indices being functions of the a_p and b_p spectral indices of the field spectra, and two breaks, which depend primarily on the peaks $\kappa_\perp$, $\kappa_\|$ of the magnetic field wavenumber distribution.

3.3.2 Radiation from an instability-generating beam

We now consider the effects of a distribution of particle energies as would be found in an actual laboratory experiment using jitter radiation to perform field diagnostics. In our first case, we consider the radiation produced by the plasma particles propagating in the filamentation instability itself. A “simple” experimental setup could generate the filamentation instability by impinging a quasi-monoenergetic electron beam

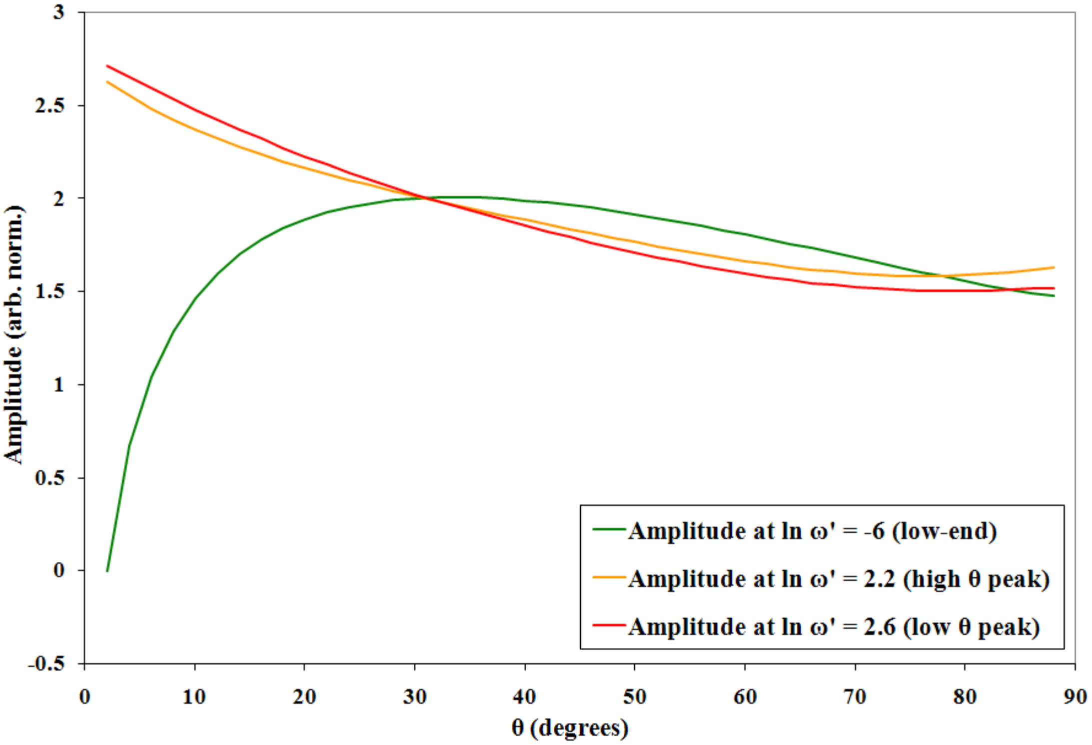

Figure 3.3: Plot of the spectral amplitudes taken at the low-ω' end of the calculated spectra, and at the approximate locations of the spectral peak for low-θ and high-θ. The dominance of one amplitude over the other illustrates the transition of the spectra from peaked to unpeaked as θ progresses from 0 to $\pi/2$.

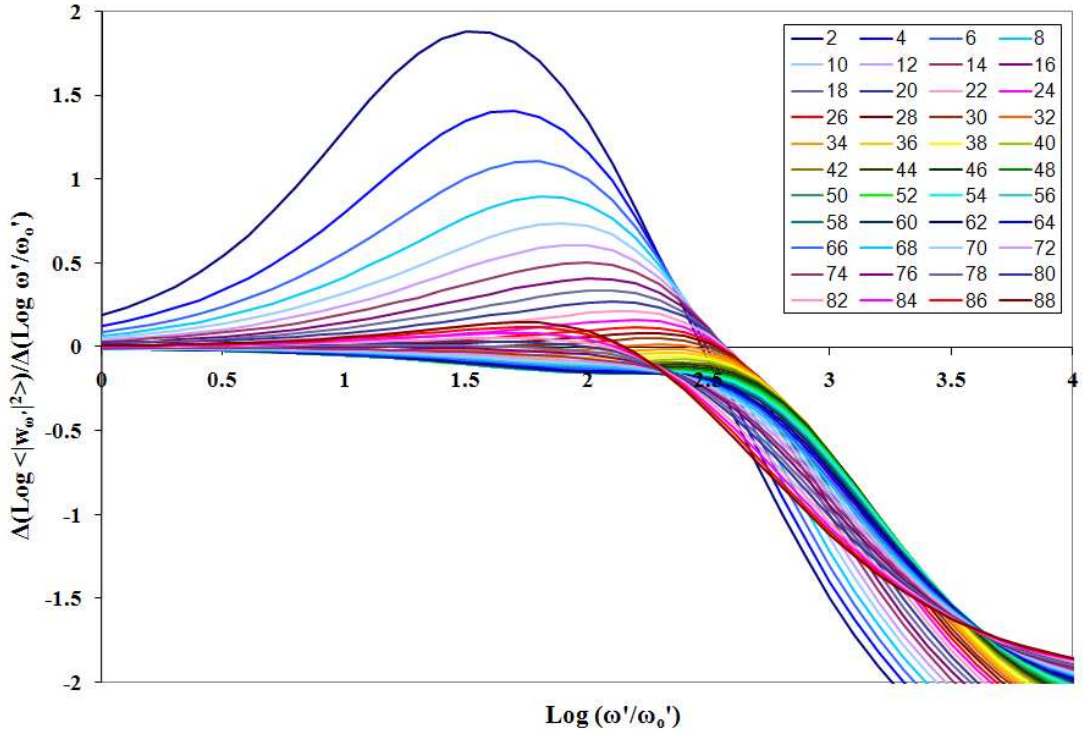

Figure 3.4: The slope of the spectra in the $\log-\log$ plot in Figure 3.1. Note that even for unpeaked spectra there is a flattening of the spectral slope and in some cases a local maximum (around $\log(\omega'/\omega_o') = 2.5$).

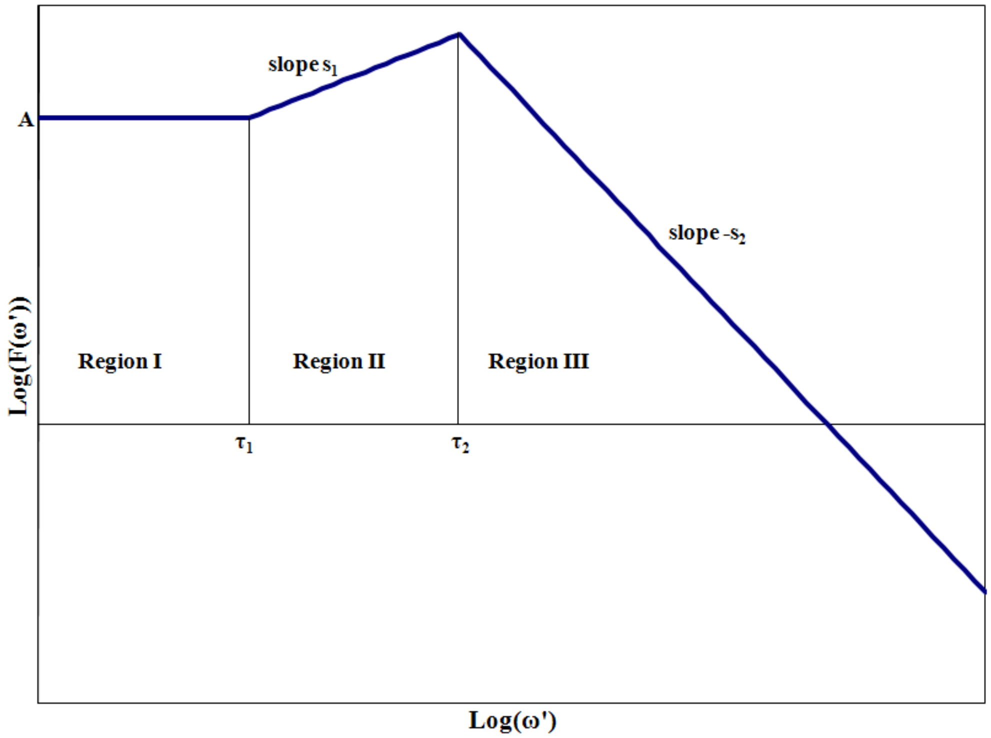

Figure 3.5: Here we show a model acceleration spectrum, as described in Equations (5.2) - (5.4). The spectrum is flat in Region I ($\log(\omega') < \tau_1$), then becomes a power law ω'^{s_1} in Region II ($\tau_1 < \log(\omega') < \tau_2$), and a power law ω'^{-s_2} in Region III ($\log(\omega') > \tau_2$).

upon a plasma, so that this electron beam both triggers the formation of the instability and provides the particle population that will be propagating through the instability after filament formation. The filamentation instability could also be formed by other mechanisms, with a strong laser beam or by generating propagating shocks within the plasma, in which case the energy distribution of the radiating particles may not be well known *a priori*. Even in the case of filamentation produced by a quasi-monoenergetic electron beam, the electrons' energy distribution may be substantially modified by the instability. While acknowledging such possible complications, we here neglect the self-consistent modifications of the beam as it propagates through the instability. We thus choose a representative quasi-monoenergetic electron beam for our radiating particle distribution, with a Gaussian energy distribution with peak energy of 200 MeV and FWHM of 50 MeV.

In this scenario, we consider the radiation produced by electrons in the same beam that produces the filamentation instability, slightly after the formation of the instability itself. The development of the filamentation instability is such that the filamentation axis $\hat{\mathbf{s}}$ will be aligned with the direction of the generating beam $\hat{\mathbf{r}}_{beam} \parallel \hat{\boldsymbol{\beta}}$. In this case, we find $\mathbf{k} \cdot \hat{\boldsymbol{\beta}} = k_{\parallel}$ and consequently, the components of $\mathbf{k}$ perpendicular to the filamentation axis are eliminated from the delta function in Equation 2.18. The resulting jitter radiation spectrum is thus obtained solely from the magnetic field distribution along the filamentation axis, $f_{\parallel}(k_{\parallel})$. Beam divergence will contribute a small influence from the transverse magnetic field to the spectrum emitted in the beam forward direction by the full particle distribution, but such contributions are strongly limited by the anisotropy of the particle distribution and the relativistic beaming factor as was shown in Figure 2.2.

For simplicity and in the absence of any particular plasma parameters governing our magnetic field distribution, we have chosen (as in the previous section) to use the same spectral parameters for the magnetic field distributions along and transverse to the filamentation axis. We have again used the arbitrary-yet-reasonable selected values for the field spectral peak $\kappa_\perp = \kappa_\| = 10$, low-wavenumber spectral indices of $a_\perp = a_\| = 2$, and high-wavenumber spectral indices of $b_\perp = b_\| = 1.5$. Our κ_p correspond to the peak of each field distribution in wavenumber, defined to be in terms of units $k_0 = \omega_0/c$. Defining our units in terms of the field correlation length $\lambda_{B\perp}$ in the direction transverse to the filamentation axis (the transverse field distribution being better developed by theory), we can define $k_0 = 10/\lambda_{B\perp}$ so that $\kappa_\perp = \kappa_\| = 1/\lambda_{B\perp}$. We then have frequency units $\omega_0 = 10c/\lambda_{B\perp}$.

Figure 3.6 shows the resulting radiation spectrum produced by electrons within the same beam that produced the instability, when the spectrum are obtained from various angles $\alpha = 0°, 2°, 5°, 10°, 45°$, and $90°$ relative to the identical direction of the beam and the filamentation axis ($\hat{\mathbf{r}}_{beam} \| \boldsymbol{\beta} \| \hat{\mathbf{s}}$, or equivalently $\theta = 0°$). The dashed line shows the spectrum produced by a particle of the electron beam's peak energy and the solid line shows the approximate overall spectrum, calculated as a weighted sum over the spectra produced by particles of different γ. The values on the vertical axis are essentially arbitrary, as they depend on the average magnetic field strength generated by the instability, the electron beam particle density, and the total volume of the radiating region in which the beam intersects with the instability. Our horizontal axis is normalized to $\omega_0 = ck_0$, which we have defined above as $10c\lambda_{B\perp}$.

3.3.3 Radiation from probe beam of varying incident angles

Exploring the magnetic field distribution transverse to the filamentation axis requires obtaining and analyzing the radiation produced by particle populations moving in these directions. We now consider our second proposed experimental scenario, in which the

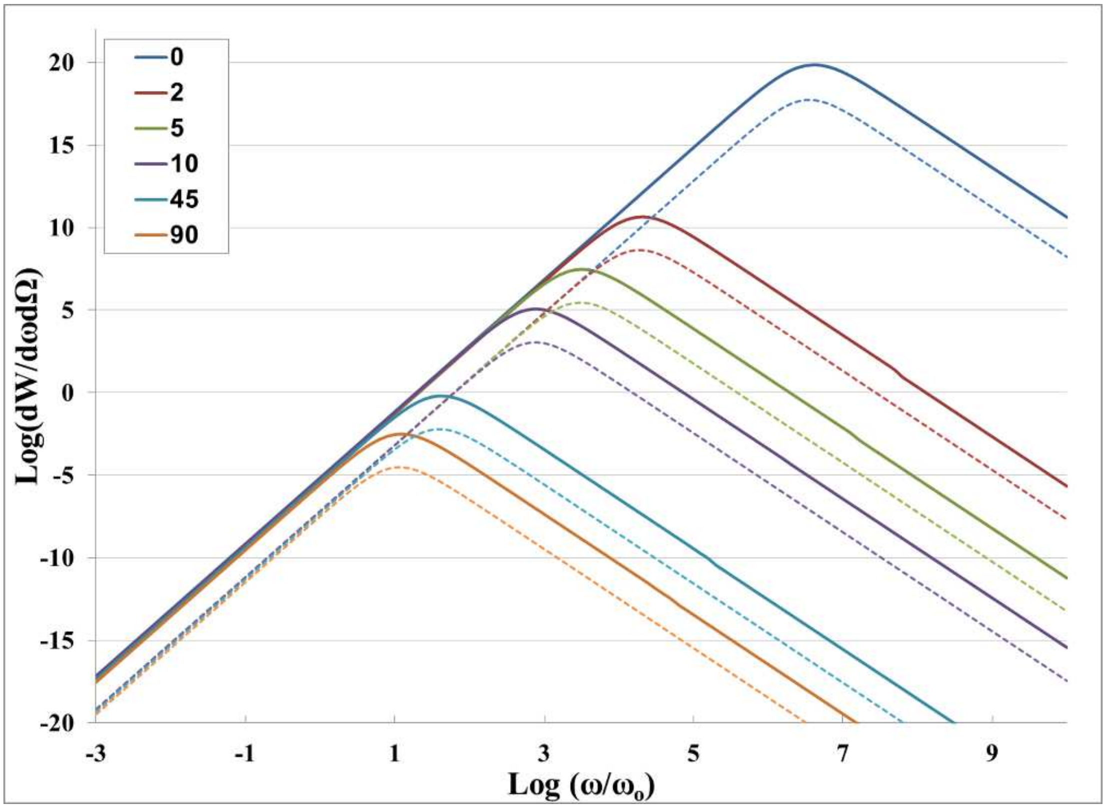

Figure 3.6: The spectrum produced by electrons moving parallel to the filamentation axis, when viewed from different angles of observation α, defined as the angle between the direction to the observer and the direction in which the beam propagates along the current filaments. Solid lines show the emission generated by the full distribution of beam particle energies; dashed lines show emission produced by an individual particle with the beam's peak energy. The maximum emission and highest peak frequency are produced in the beam's forward direction ($\alpha = 0^\circ$). As it progresses to larger viewing angles (shown are $\alpha = 2^\circ, 5^\circ, 10^\circ, 45^\circ$, and 90°), the spectrum maintains its overall shape but dims overall and softens in peak energy.

electron beam used to generate the instability is split prior to entering the plasma (or a second beam generated) and redirected to probe the instability from other angles θ between the filamentation axis and the radiating beam. Since the peak emissivity will still be in the radiating particle populations forward direction, the radiation spectra would ideally be obtained with movable detectors that can be positioned in or close to the direction of the beam's path through the filamentation region (outside of the filamentary region the beam may be deflected so as not to hit the detectors). Figure 3.7 shows the spectrum for incident beam angles of $\theta = 0^\circ, 2^\circ, 5^\circ, 10^\circ, 45^\circ$, and 90° when viewed from the beam's forward direction ($\alpha = 0$). As in the previous subsection, the vertical normalization is essentially arbitrary, but the horizontal normalization is defined in terms of $\omega_0 = ck_0 = 10c\lambda_{B_\perp}$, where $\lambda_{B_\perp}$ is the correlation length of the magnetic field distribution transverse to the filamentation. The case $\theta = 0^\circ$ is of course equivalent to that considered in section 3.3.2 if there is no variation in the energy distribution between the probe beam and the beam that generated the instability.

For each θ, we have also calculated the spectrum for several different viewing angles $\alpha = 2^\circ, 5^\circ, 10^\circ, 10^\circ, 45^\circ$ and 90°, where α is again defined as the angle between the direction to an observer and the unit vector $\hat{\mathbf{r}}_{beam}$ along the probe beam, as measured in the same plane as the angle θ on the far side of $\mathbf{r}_{beam}$ from $\hat{\mathbf{s}}$. Figure 3.8 shows the results for probe beam incident angles of $\theta = 2^\circ, 5^\circ, 10^\circ, 45^\circ$ respectively. We have omitted the $\theta = 90^\circ$ case from Figure 3.8 has been omitted since at these scales it appears nearly identical to the $\theta = 45^\circ$ case (see Figure 3.7). As before, solid lines show the weighted sum over our distribution of γ, while dashed lines show the spectrum produced by an individual particle at the peak value of γ (here a representative 200/0.511 Mev). The spectrum from an individual particle and the full distribution differ notably in amplitude but not significantly in overall shape. For all of the probe beam angles, the spectrum is strongest when viewed along the probe beam (viewing

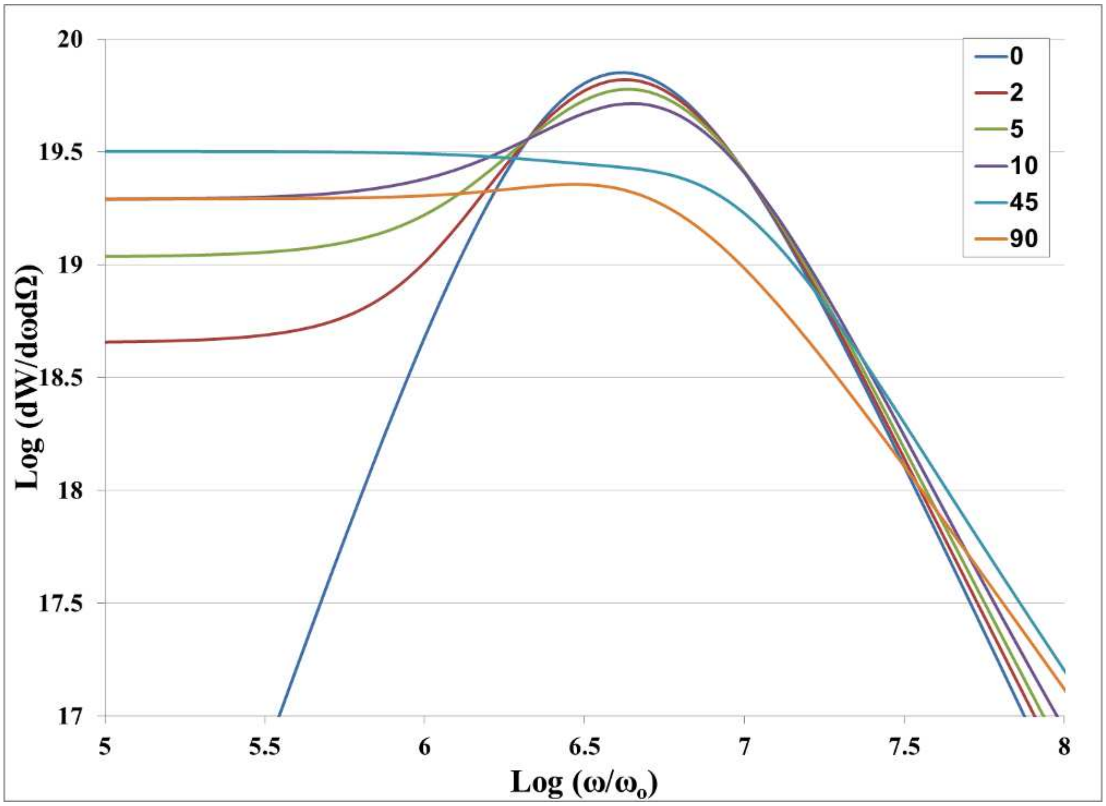

Figure 3.7: Calculated jitter radiation spectra such as produced a representative quasi-monoenergetic beam of particles probing the filamentation instability region at angles $\theta = 0^\circ, 2^\circ, 5^\circ, 10^\circ, 45^\circ$, and 90° relative to the filamentation axis, all viewed along the radiating beam ($\alpha = 0^\circ$). The spectrum notably changes from a peaked form with low-energy spectral index of approximately 2 at $\theta = 0$, through peaked forms with a second low-energy break at $\theta = 2^\circ, 5^\circ$, and 10°, to forms with a break (but no distinguishable peak) and a flat low-energy spectral index of 0 at $\theta = 45^\circ$ and 90°. Note that the horizontal scale has been selected here to focus on the region immediately surrounding the peak/break.

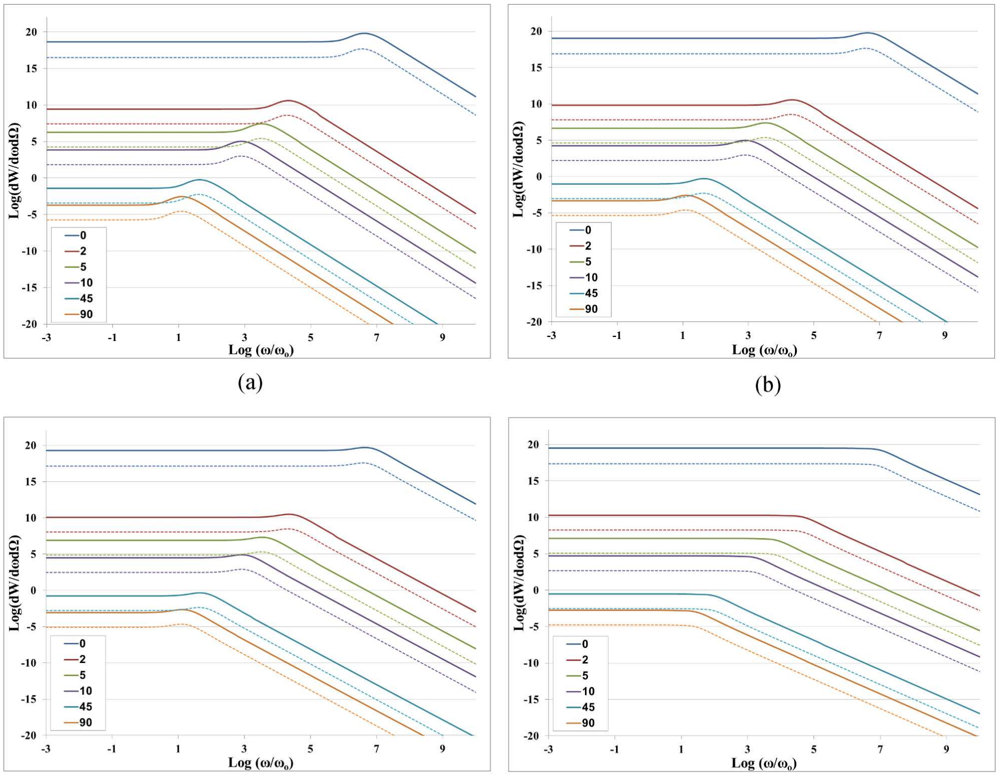

(a)

(b)

(c)

(d)

Figure 3.8: Variation in the jitter radiation spectrum produced by a quasimonoenergetic beam (solid lines) and an individual particle of the beam's peak energy (dotted lines). Each figure shows results for a particular angle θ between the probe beam and the instability's filamentation axis, when viewed from different viewing angles $\alpha = 2^\circ$ (a), 5° (b), 10° (c), and 45° (d), all measured from the beam direction $\boldsymbol{r}_{beam}$ in the same plane as θ.

angle $\alpha = 0^\circ$), with amplitudes decreasing rapidly by several orders of magnitude even when viewed at comparatively small viewing angles of $\alpha = 2^\circ, 5^\circ$, and 10° (in keeping with the relativistic beaming we expect). While the overall spectral shape is unchanged, the viewing angles α also result in a shift of the spectrum to shorter wavelengths ω. This shift can be determined analytically from equation 2.12, from which we find that for the case $\theta = 0^\circ$ a spectral feature located at $\log \omega_p$ in the $\alpha = 0^\circ$ will be shifted to $\log \omega_p - \log((1-\beta \cos \alpha)/(1-\beta))$ when viewed at other angles α.

3.4 Discussion of Results

We have numerically calculated the jitter radiation spectrum as produced by particles of a single (delta-function) energy and of a Gaussian energy distribution. As expected, we find that the jitter radiation spectrum is strongly dependent on the angle θ between the particle's velocity $\boldsymbol{\beta}$ and the direction $\hat{\mathbf{s}}$ which defines the anisotropy of the turbulent magnetic field distribution produced by current filamentation. The basic form of the resulting jitter radiation spectrum for a single-energy particle distribution at θ close to 0 is flat at low-frequencies, followed by two power laws with a peaked transition point in between them. For our choice of field parameters, the spectrum transitions to an unpeaked form after $\theta \approx 26^\circ$, with a peaked form re-emerging as θ approaches $\pi/2$. The unpeaked spectra can be approximately described as flat at low-wavenumber, transitioning at a break point to a power law decrease at high-wavenumber. However, the extended transition region for some of the unpeaked spectra suggests that a three-region description may still be best to fit such spectra.

We have also considered the angle-resolved jitter radiation spectrum as produced two particle beam scenarios as might be used in laboratory high-energy density plasmas to generate the Weibel-like filamentation instability and diagnose the magnetic field distribution using the jitter radiation spectrum. In one case, we consider particles directed in the beam that generates the instability, directed along the axis of filamentation. In the other case, we consider radiation produced by a secondary "probe" beam of particles directed into the instability region to generate jitter radiation at a wider variety of angles θ between the particle paths and the filamentation axis. The resulting radiation spectra are calculated for several different viewing angles α with respect to the probe beam, as well as several different incident angles $\theta = \Theta_{probe}$ of the beam with respect to the filamentation axis $\hat{\mathbf{s}}$.

We find that in either case the emissivity is strongly peaked in the forward beam direction as expected. The spectral distribution of the generated spectrum is dependent primarily on the distribution of the magnetic field wavenumber's component along the beam. Thus, the spectrum produced by the instability-generating beam in subsection 3.3.2 contains details about the magnetic field distribution along the filamentation axis. Information about the transverse magnetic field distribution must be obtained by using a secondary beam to probe the instability region at angles transverse to the current filamentation, as we demonstrate in subsection 3.3.3.

Chapter 4

Astrophysical Applications of Jitter Radiation

4.1 Summary

Small-scale magnetic field turbulence can be generated in a wide variety of astrophysical plasmas. In particular, the filamentation instability introduced previously is expected to operate where counterstreaming particle populations occur downstream from internal shocks or in outflow from sites of magnetic reconnection. We have focused our work on gamma-ray bursts as one proposed site of such turbulence. The theory of jitter radiation may be able to explain observational features of GRB spectra that contradict standard synchrotron radiation models.

4.2 Observed Spectral Features of Gamma-Ray Bursts

In Chapter 1 we presented the basic history of GRBs, an overview of their basic observational features, and an introduction to the theoretical framework in which they are being explored. As we outlined there, the past twenty years of GRB observation have been particularly fruitful, not just in increasing the number of GRB detections but also in expanding the information obtained along with each event. For our purposes, we are specifically interested in the role that small-scale magnetic field turbulence may play within GRB prompt emission and whether jitter radiation signatures within such emission can uncover these underlying dynamics.

The Burst and Transient Source Experiment (BATSE) on board the Compton Gamma-Ray Observatory (CGRO), launched in 1991 and deorbited in 2000, was designed to continually monitor the full area of sky for a sudden rise in gamma-ray counts, corresponding to a gamma-ray burst, a solar flare, or other astrophysical event. Upon detecting a "burst trigger" event, BATSE would initiate appropriate data recording and could also send signals to the other CGRO instruments for concurrent measurements. BATSE consisted of 8 modules, each equipped with a large area detector (LAD) and a spectroscopy detector (SD). The LADs were designed to provide the sensitive full-sky monitoring responsible for detecing burst triggers. Comparison of the count rates detected in each LAD also allowed for a rudimentary localization of the GRB, to within a couple degrees of sky. While the LADs provided good temporal resolution of a burst event, the SDs were designed to provide better energy resolution. In all cases better energy resolution was obtained for brighter bursts. [Kaneko, 2005, Band et al., 1993] BATSE's impressive catalog of over 2000 GRB detections remains one of the best sources of GRB spectra for analysis.[Band et al., 1993, Schaefer et al., 1994, Ford et al., 1995, Kaneko et al., 2006]

Both time-resolved and time-integrated GRB spectra are generally describable as a power law at low-energies with a transition to a separate power law at high energies. Fits to the spectral data generally make use of either a broken power law (BPL) model, a smoothly-broken power law (SBPL) model, or the empirical Band function model (also a transition between two power law forms) that was developed in Band et al. [1993] and found to fit many GRB spectra well. The BATSE spectral catalog has been extensively analyzed using a variety of these fits to search for correlations between

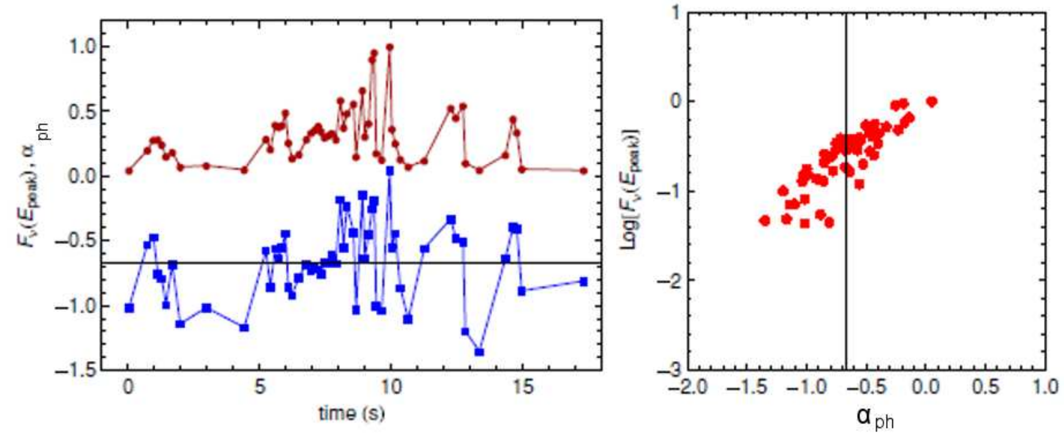

Figure 4.1: Fits to the time-resolved spectra in GRB 970315 (BATSE burst 6124) indicate that the spectral flux F_ν at peak energy E_{peak} (left panel, top, in dark red) increases and decreases in correspondences with the photon index (the low-energy index of the photon spectrum $N_E(E)$) α_{ph} (left panel, bottom, in blue). For large $F_\nu(E_{peak})$ the photon index α_{ph} exceeds the synchrotron limit $\alpha_{ph} \leq -2/3$ shown as a horizontal line in the left panel and as a vertical line in the right panel. Data from Kaneko et al. [2006].

spectral features. Among the results of such studies, it was noted that the flux at the peak energy in the spectrum appears to track with the low-energy spectral index, so that the "harder" spectra with a steeper incline at low-energies tend to have higher flux at the peak energy.[Crider et al., 1997] Figure 4.1 shows an example of this tracking behavior for GRB 970315 (BATSE burst 6124), with higher values of the photon index α_{ph} (the low-energy spectral index of the photon spectrum $N_E(E)$) clearly corresponding to larger flux at peak energy $F_\nu(E_{peak})$. Certain time-resolved GRB spectra also appear to evolve in time from "hard" to "soft" photon index values.[Crider et al., 1997, Bhat et al., 1994]

Figure 4.1 also demonstrates the remarkable result that a percentage of time-resolved GRB spectra appear to be steeper at low-energies than would be achievable from synchrotron radiation, violating what is known as the synchrotron "line of death".[Crider et al., 1997, Preece et al., 1998, Frontera et al., 2000, Kaneko et al., 2006] As we

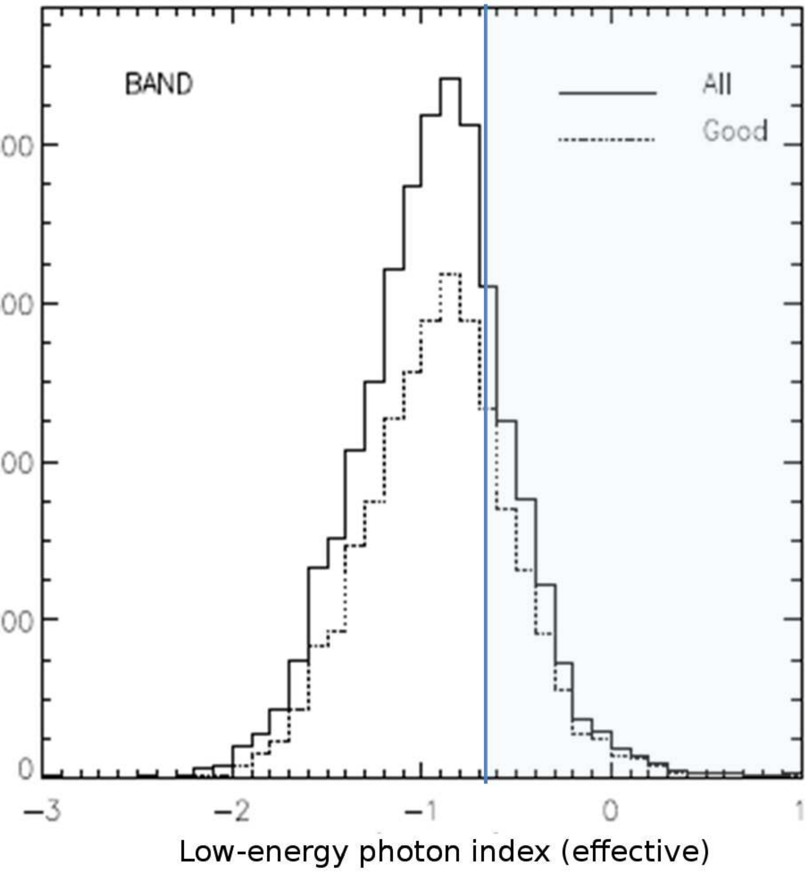

Figure 4.2: Distribution of the effective low-energy photon index as determined by BAND fits to 8459 time-resolved spectrom from the BATSE catalog [Kaneko et al., 2006]. To minimize the effects of BATSE's energy window, the *effective* low-energy photon index is the slope of the BAND fit to the observed spectrum taken at the lower-boundary of BATSE's energy window (25 keV), following an approach developed in Preece et al. [1998]. A vertical line indicates the -2/3 limit on the photon index in optically-thin synchrotron spectra, with the faintly shaded region to the right of this line indicating the portion of the spectral sample that violate this limit. Adapted from Kaneko et al. [2006].

noted in Chapter 1, Section 1.4, synchrotron radiation is limited to low-frequency spectral indices no larger than $1/3$ in the F_ν spectrum and low-energy spectral indices no larger than $-2/3$ in the corresponding photon spectrum $N_E(E)$. Analysis of the BATSE spectral catalog [Kaneko et al., 2006] demonstrated that a sizable percentage of time-resolved GRB spectra fit violated this synchrotron limit, as shown in Figure 4.2. Low-energy spectral index values in excess of the indicate that the synchrotron shock model cannot be producing such GRB spectra without some additional modification. Since the jitter radiation spectrum can be steeper than the synchrotron "line of death" at low energies, it may provide an explanation for the appearance of synchrotron-violating spectra.

4.3 Calculating Jitter Radiation from GRB Sources

4.3.1 Basic Model and Approach

We assume that the bulk of the GRB prompt emission is produced by portions of the jetted outflow which radiate strongly for a brief time when energized by plasma shocks or reconnection events. If we consider the GRB source as a jet of material relativistically propelled outward from some central engine, variations in outflow speed and density will result in a series of internal shocks within the jet. As discussed in Chapter 1, simulations indicate that the filamentation instability tends to occur at or near a propagating shock front and produce small-scale magnetic field turbulence which will cause the particles to radiate in the strong jitter regime.

We consider the propagating shock front within the GRB jet to be a portion of a relativistically expanding curved shell, briefly illuminated as it emits jitter radiation. In the simplest model, the filamentation forms directly as a result of particles streaming towards and away from the shock front and so the local filamentation axis $\hat{\mathbf{s}}$ will be aligned with the normal to the shock front $\hat{\mathbf{N}}_{shock}$ (that is, $\hat{\mathbf{s}} \parallel \hat{\mathbf{N}}_{shock}$. The curvature of the shock front means that, for an external observer located in direction $\hat{\mathbf{n}}$, the first radiation received will be from the leading edge of the shock front in the observer's direction, for which $\hat{\mathbf{N}}_{shock} \parallel \hat{\mathbf{n}}$ and at successive times will be from annular portions of the shell where the shock normal $\hat{\mathbf{N}}_{shock}$ is directed at an angle to the observer's line of sight.

Analysis of the high-ω and low-ω asymptotic behavior of the angle-averaged radiation spectrum for regions of filamentation viewed head-on (along the filamentation axis) and edge-on (transverse to the filamentation axis), as carried out in Medvedev [2006], yields:

$$
\begin{aligned}
&\text{for } \theta = 0, \qquad && \frac{dW}{d\omega} \propto \begin{cases} \omega^{1} & \text{if } \omega \ll \kappa_{\parallel} v \gamma^{2} \\ \omega^{-2\beta_{\parallel}} & \text{if } \omega \gg \kappa_{\parallel} v \gamma^{2} \end{cases} \\
&\text{for } \theta = \pi/2, \qquad && \frac{dW}{d\omega} \propto \begin{cases} \omega^{0} & \text{if } \omega \ll \kappa_{\perp} v \gamma^{2} \\ \omega^{-2\beta_{\perp}+1} & \text{if } \omega \gg \kappa_{\perp} v \gamma^{2} \end{cases}
\end{aligned}
\tag{4.1}
$$

where θ is the angle between the line of sight and the filamentation axis [Medvedev, 2006]. We thus expect the radiation spectra from an instantaneously illuminated spherical shell to vary between these two forms at successive observation times, dominated by the parallel or the transverse spectra as we vary between the two extremes.

Because of the differences in travel time from different portions of the radiating region, an instantaneous "emission event" in which the curved shell radiates translates naturally into a lightcurve received by an observer. Recalling that we defined the angle θ as the angle between the local filamentation axis $\hat{\mathbf{s}}$ and the direction $\hat{\mathbf{n}}$ to the observer (all in the co-moving frame of radiating region), we can see that this means that the received radiation spectrum will naturally evolve with time from $\theta = 0^\circ$ at the leading edge towards $\theta = 180^\circ$, with the range of angles θ depending upon the geometry of the radiating shock front and the extent to which the emission comes from a narrow jet or a complete spherical shell. Notably, this rapid temporal evolution of the spectral form arises simply from the geometry and the sensitivity of jitter radiation to the magnetic field anisotropy produced by the filamentation instability, rather than requiring any large-scale evolution in particle dynamics.

Recent research suggests that magnetic field carried along with the plasma outflow may play an important role within many jetted outflows, both in aspects of jet structure and in converting stored magnetic energy to particle acceleration through magnetic reconnection. In magnetic reconnection, segments of the plasma containing frozen-in magnetic field lines are forced by the jet dynamics into a critical state which causes the magnetic field configuration and associated particle motions to change rapidly. This can cause particle acceleration and redirection of bulk plasma flows within the jet. In our model, instead of bulk plasma flow being oriented radially inward and outward near a shock front, magnetic reconnection could generate localized strong plasma flows that occur in various directions as outflow from sites of magnetic reconnection. The filamentation instability would then cause the growth of small-scale magnetic field turbulence within these various "patches" of reconnection outflow. In such a model, the local filamentation axis $\hat{\mathbf{s}}$ would not tend to be radial and could have a much wider range of orientations relative to the normal of the radiating shell. Consequently, it would be possible to have more complex variations in the temporal evolution of the angle θ and the corresponding form of the jitter radiation from a single radiating shell.

To produce a simulated GRB using jitter radiation, we first calculate the spectrum as produced in the rest frame of an individual radiating region, then we relativistically transform this into the radiation spectrum as would be seen by an observer. The resulting spectrum is fit using the Band function commonly used for GRB spectral analysis. We may incorporate the effects of various jet geometries, alignments, and bulk Lorentz factor profiles to generate the time-evolving spectrum from a single jet front. A complete GRB may then be simulated by combining the "flashes" of multiple shells at random times with varying brightnesses that fit the statistical distribution of actual observed GRBs. The resulting time-resolved GRB spectra can be binned and fit as it would by various detectors and the results compared with real observations made by BATSE (CGRO), Fermi, or Swift.

4.3.2 Jitter Radiation Spectra in the Comoving Frame

We present here the jitter radiation spectra in the rest frame of the radiating region as it propagates relativistically away from the central engine of the GRB source. As discussed earlier, the radiation spectrum emitted depends upon the particle's angle θ with respect to the filamentation axis. Assuming an isotropic distribution of radiating particles, the radiation emitted into a particular direction towards an observer will be dominated by the emission from particles whose velocities are within a small angle of that direction (that is, $\hat{\boldsymbol{\beta}} \approx \hat{\mathbf{n}}$). The relativistic motion of the radiating shell means that radiation emitted into all directions in the shell's frame will be redirected towards the forward direction of the propagating shell. Consequently, we average the jitter radiation spectrum for a particular particle velocity orientation $\boldsymbol{\beta}$ relative to the local filamentation axis over all emission angles α and ϕ. We thus use the angle-averaged form of the jitter radiation equation 2.37 as developed in Chapter 2, Section 2.4.

Calculating the angle-averaged spectrum using Equation 2.37 requires two levels of numerical integration. First, we integrate over two of the three components of magnetic wavenumber (the integral over the third component having produced a substitution due to the delta function in Equation 2.12, as was discussed in Section 2.3). This result is the angle-resolved spectrum as developed in Chapter 2 and explored in terms of its laboratory applications in Chapter 3. The angle-resolved spectrum is directly proportional to $\langle|\xi^2|\rangle$, the average over the Fourier spectrum of the accelerations undergone by the particle; consequently, we will refer to the angle-resolved spectrum from here on as the "acceleration spectrum".

The second integration comes from averaging over all emission angles α and ϕ, where we have converted the integral over viewing angle α to an integral over $\omega' = \omega(1-\beta\cos\alpha)$ with a variable limit that translates the effective shift based on α of the first integration result's frequency dependence into an integral over a single spectral form.

We present full numerical calculations of the jitter radiation spectrum, generated by successive numerical integrations of equations (5.1) and (2.33) or (2.35) The results for varying angles θ are presented in Figure 4.3, with data point intervals of 0.2 on the $\log_e(\omega)$ scale. We have normalized the spectra such that the low-energy asymptotic value of the $\theta = 2$ spectrum is unity.

The angle-averaged radiation spectrum results again show significant changes in the spectra emitted at different angles θ relative to the main filamentation axis of the magnetic field spectrum. Note that this viewing angle effect is entirely due to particles with velocities directed along the line of sight providing the dominant contribution to the radiation emitted to any particular viewing angle, since we are using the angle-averaged emissivity for the spectrum emitted in the forward direction by particles with a particular orientation angle relative to the magnetic field filamentation.

Figure 4.4 shows a more detailed view of the peak region, calculated at data point intervals of 0.05 in $\log_e(\omega)$. The spectral shapes and trends are, as expected, much like the acceleration spectra results seen previously, but broadened and flattened overall due

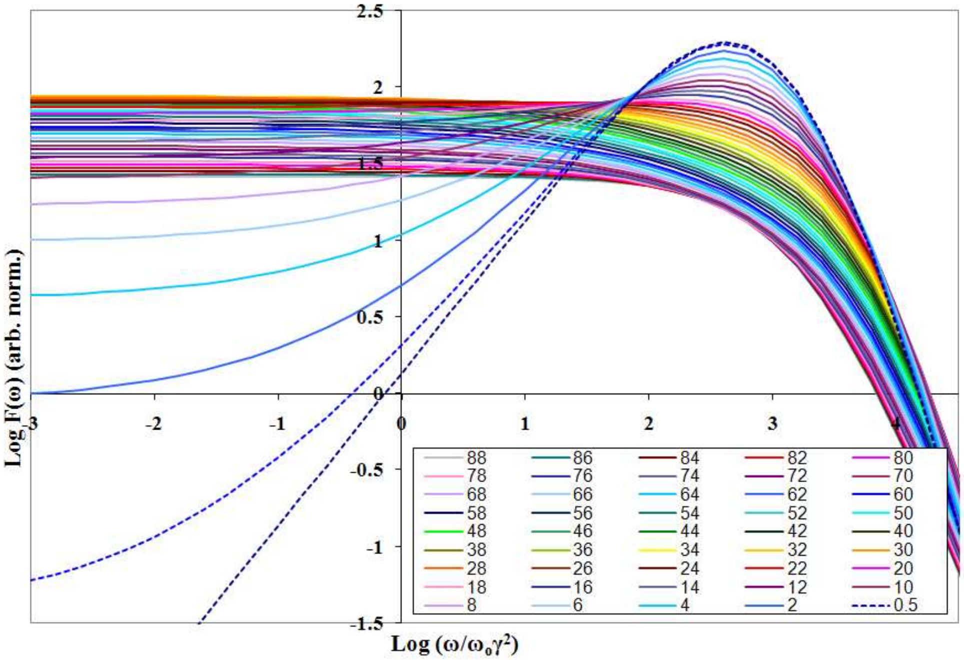

Figure 4.3: The angle-averaged radiation power spectra (F_ν) of jitter radiation, numerically calculated for a step size of 0.2 in $\log(\omega)$ for every two degrees in θ. The dotted lines are numerical calculations for values close to θ=0, illustrating the behavior of the spectrum in this limit. The spectra are arbitrarily normalized so that the first calculated value for the $\theta = 2$ spectrum is 0. The radiation spectra are flat for low-ω, then slope upwards to a notable peak for low θ. As θ progresses to $\pi/2$, the low-ω' amplitude increases and the size of the sloped region decreases until the spectra becomes relatively flat until its sharp decline at high-ω.

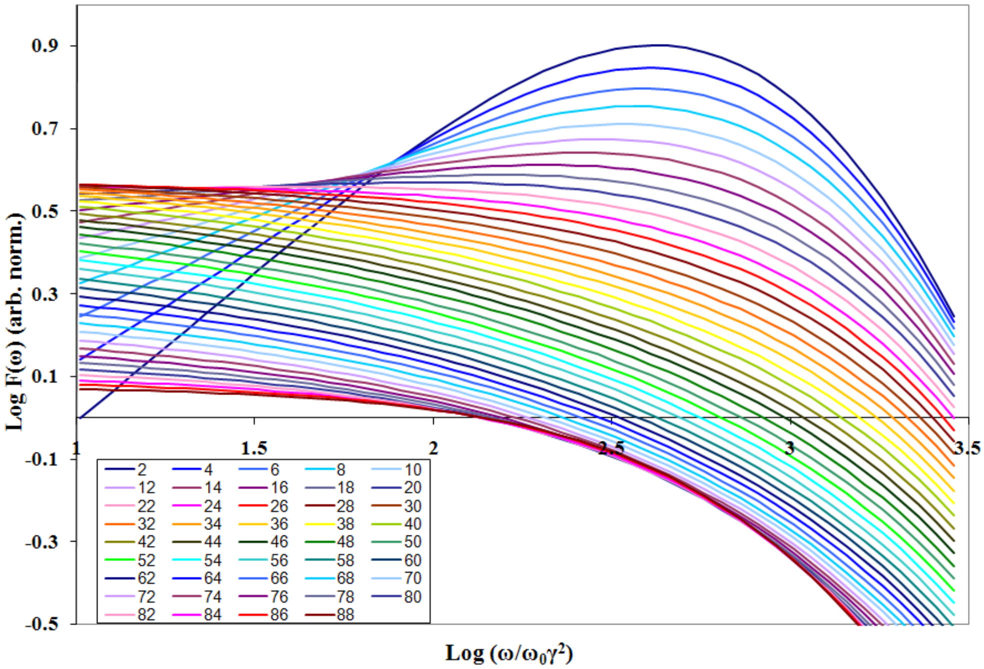

Figure 4.4: A more detailed view of the radiation spectra in the region of the spectral peak. The spectral values are calculated every 0.05 in $\log(\omega)$ for finer resolution of the detail in this region.

to the second integration. Notably, no peak reemerges in the angle-averaged radiation spectra as θ approaches $\pi/2$ although the trend suggests that peak re-emergence for θ near $\pi/2$ may be possible with a different parametrization of our magnetic field spectra. Figure 4.5 shows the νF_ν spectrum such as is commonly presented for GRBs and used in GRB spectral analysis.

Like the acceleration spectrum, the radiation spectrum can be generally described in terms of three regions (two spectral breaks), and an amplitude or slope in each. In contrast, the spectral fits typically used for GRB data analysis (i.e., broken power law (BPL), smoothly-broken power law (SBPL) or Band function) are all two-region fits. Because for jitter radiation the soft spectral index varies continuously and approaches 0 for low ω, the results of a simple two-region fit to these spectra would depend sig-

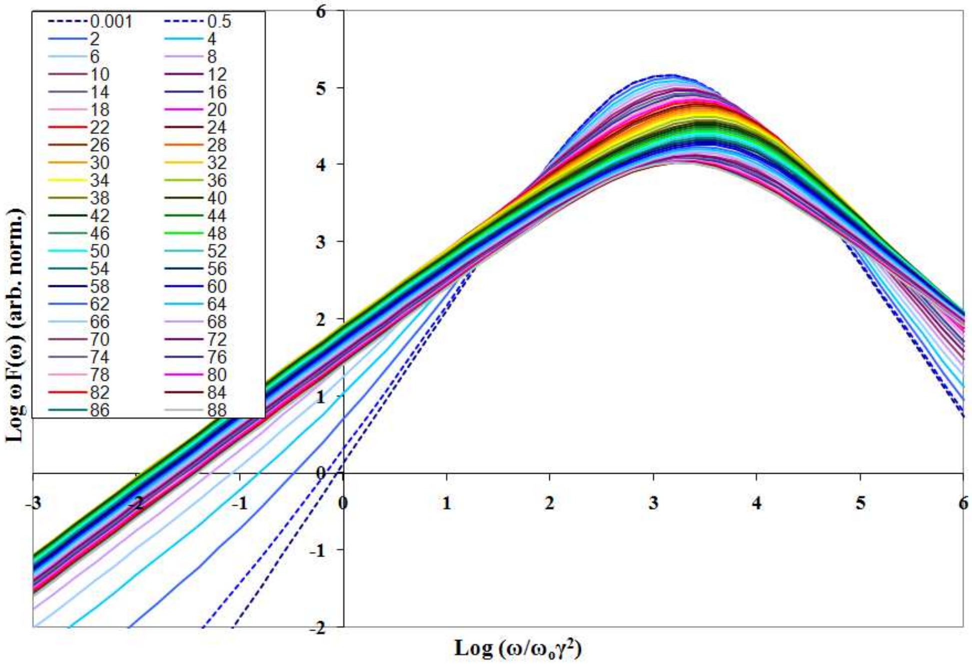

Figure 4.5: The νF_ν spectra calculated from our jitter radiation power spectral results. The νF_ν spectral peak is the peak energy E_p used in the Band functional fit commonly used for GRB spectra [Band et al., 1993, Kaneko et al., 2006].

nificantly upon where the lower bound of the data window falls relative to the peak. Within a fixed data window, a two-region spectral fit would tend to produce an artificial reduction in the soft spectral index for spectra with higher-frequency spectral peaks or breaks.

Unfortunately there is no simple way to characterize the behavior of the middle range of the spectrum because of the transition from peaked to unpeaked spectra as θ varies. Even in unpeaked spectra, the extent and curve of the transition region between the flat low ω' part of the spectrum and the strongly negatively-sloped high ω' part of the spectrum varies substantially. Consequently, we have chosen to model the unpeaked spectra still as a three-region spectra rather than solely by its upper and lower asymptotes.

To conveniently summarize the spectral features and their evolution in this section, we have developed a five-parameter fit which describes the spectral behavior in three regions, which we designate as Regions I, II, and III. We can thus characterize the spectra by defining three lines (each requiring a slope and a reference point on that line) and finding the transition points at which they intersect. We have chosen our technique to optimize our results for the spectral indices, rather than the spectral transition points. The same fit technique may be applied to either the acceleration (or angle-resolved) spectrum or the radiation (angle-averaged) spectrum. We describe here our fitting method and then present the results of its application to both types of spectra.

Region I (flat, amplitude A): The low-frequency region I is flat, with a slope close to zero. To describe this region, we take our initial calculated amplitude to be A, the low-frequency amplitude. For very small θ our lower calculation boundary may be insufficient to capture the initial flat part of the spectrum, since our first spectral transition point approaches -∞ as θ goes to 0.

Region II (positive or negative slope s_1): The intermediate-frequency region II may have positive slope resulting in a peak or a slight negative slope (of notably less magnitude than the slope in region III). We have defined the "drop point" as the region where the second derivative reaches its minimum value. As the place of largest negative change in slope, this coincides well with the "knee" or second break of the function, and is always at slightly higher frequencies than the peak itself. This has the advantage of being consistently definable for both the peaked and unpeaked spectral forms. We then find the slope and a reference point in this region by either:

- Method a: for peaked spectra, we take the maximum value of the numerical derivative as s_1 and the data point corresponding to this maximum value as our defining reference point.
- Method b: for unpeaked spectra, we take the average value of the numerical derivative in the region between the drop point and the "deviation point" where the spectrum first drops below $A - 0.01$ (this corresponds to a deviation of about 1% from its original value). Our reference point is the data point halfway between or next highest to halfway between the deviation and drop points.

Region III (negative slope, defined as -s_2): The high-frequency region III has a large negative slope compared to the rest of the function. This slope is still changing over the region close to the second spectral break that we are considering, so we determine a representative slope by calculating the slope of a line between the drop point, which is the minimum of the numerical second derivative, and the higher frequency point that is the minimum of the absolute value of the numerical second derivative (the data point closest to where the second derivative crosses zero in this region). These points are well-defined for all our radiation spectra as long as the calculation boundary extends a couple orders of magnitude in e above the drop point. Either point may be used as a reference point in this region.

The first spectral transition point τ_1 is obtained by solving for the intersection of the lines defined in Regions I and II, and the second spectral transition point τ_2 is obtained by solving for the intersection of the lines in Regions II and III.

We have chosen to work with the F_ν spectrum because of the convenience of its distinctive flat (spectral index of 0) initial amplitude, but it is easy enough to translate F_ν spectral features into spectral features of the νF_ν spectrum or the photon spectrum $N(E)$, as the spectral indices will simply be increased or decreased by 1 and the transition points between the power law regions will roughly coincide, with a slight shift based on normalization. In terms of the Band function fit commonly used for GRB spectra [Band et al., 1993], the relation between the high-energy spectral indices is $\beta_{Band} = s_2 - 1$. The relation between the low-energy spectral indices is complicated by the fact that the Band function is a two-region fit and not sensitive to multiple spectral indices below the spectral peak; consequently α_{Band} will range between -1 and $s_1 - 1$ depending on where the data fitting window falls relative to our first spectral break τ_1. The νF_ν peak energy, which is E_p in the Band function, will correspond to a slope of -1 in the F_ν spectrum, and will lie roughly in the vicinity of the second spectral break τ_2 in our fit.

Figures 4.6 - 4.10 show spectral fit results obtained using our above technique on both the acceleration and (angle-averaged) radiation spectra. In addition to data resolution effects, our results reflect the unavoidable discontinuity in fitting the peaked vs. unpeaked form of the spectrum (this transition occurs around $\theta = 26^\circ$ in our results).

Figures 4.6 and 4.10 indicate that the amplitude A and the high-frequency spectral index s_2 are close in both their values and their evolution with θ for the two types of spectra. The mid-range spectral index s_1 varies similarly in 4.8 for both spectra, but

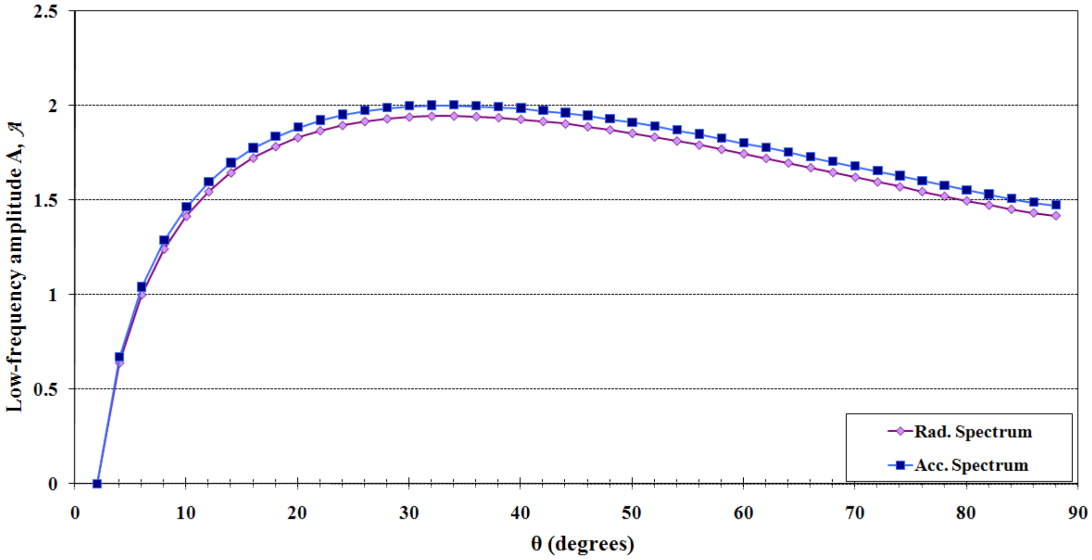

Figure 4.6: The angular dependence of the low-frequency amplitude A of our calculated jitter radiation spectra and the corresponding variation of the low-frequency amplitude $\mathcal{A}$ of our calculated acceleration spectra. The low-energy amplitude in each case is taken to be the first calculated value of the spectrum; for our choice of parameters and calculation window, this initial value is well below the first spectral break for all $\theta > 2^\circ$. In both cases, we have normalized our spectra such that the low-energy amplitude at $\theta = 2^\circ$ is 0.

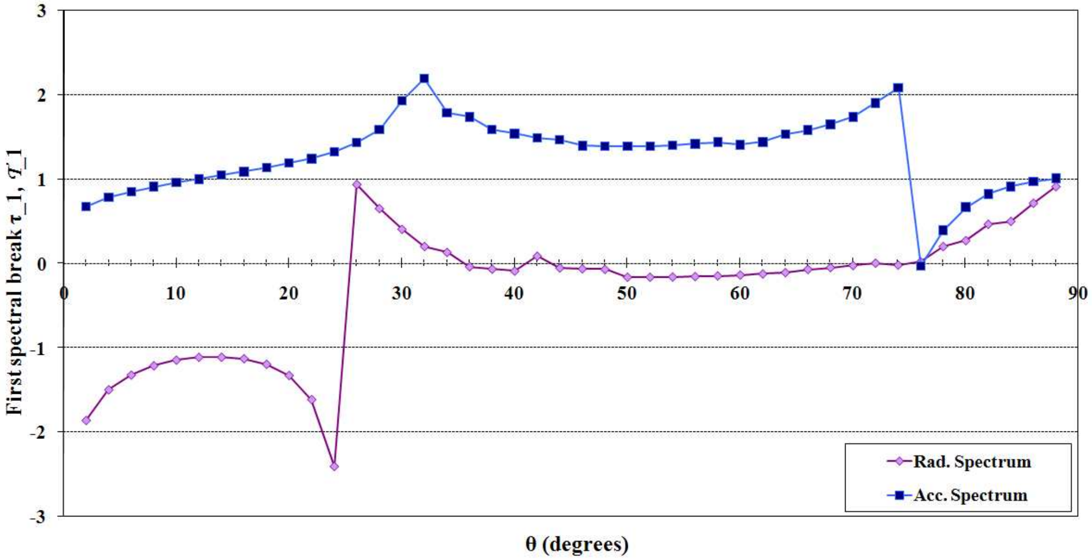

Figure 4.7: The angular dependence of the first spectral break positions $\log_e(\omega/\omega_o\gamma^2) = \tau_1$ and $\log_e(\omega'/\omega'_o) = \mathcal{T}_1$ in our calculated jitter radiation spectra and acceleration spectra, respectively. In each case these transition points are found as the intersection between the low-frequency fit line of slope 0 and the mid-range fit line of slope s_1 (radiation) or $\mathcal{S}_1$ (acceleration), as found by our described fit.

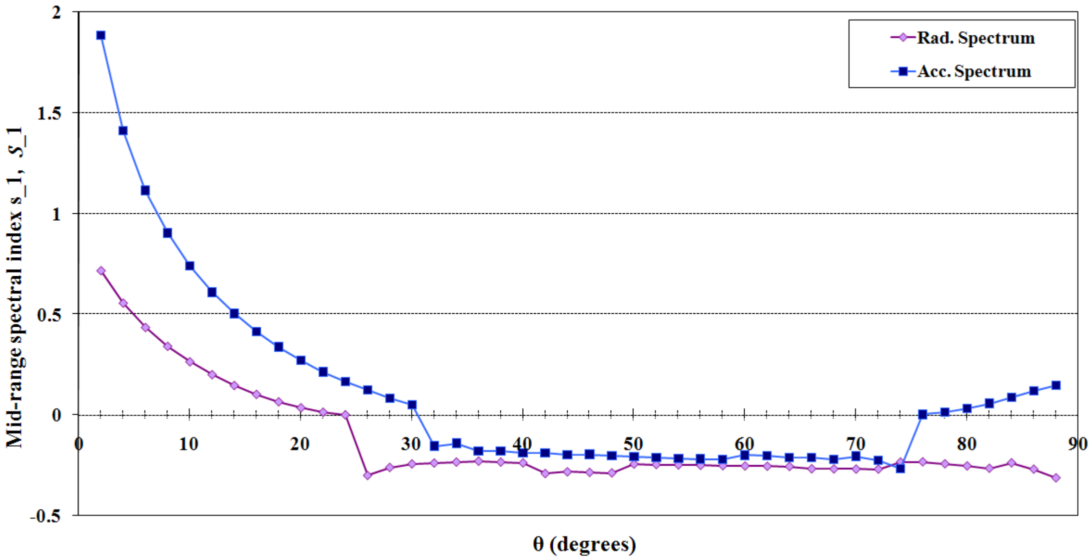

Figure 4.8: The angular dependence of the mid-range spectral indices s_1 of our calculated jitter radiation spectra and $\mathcal{S}_1$ of our calculated acceleration spectra. For peaked spectra the mid-range spectral index is the maximum slope below the spectral peak; for unpeaked spectra the mid-range spectral index is the average slope between the point at which the spectrum falls below $A - 0.01$ and the point at which the numerical second derivative reaches its minimum value (the "drop point").

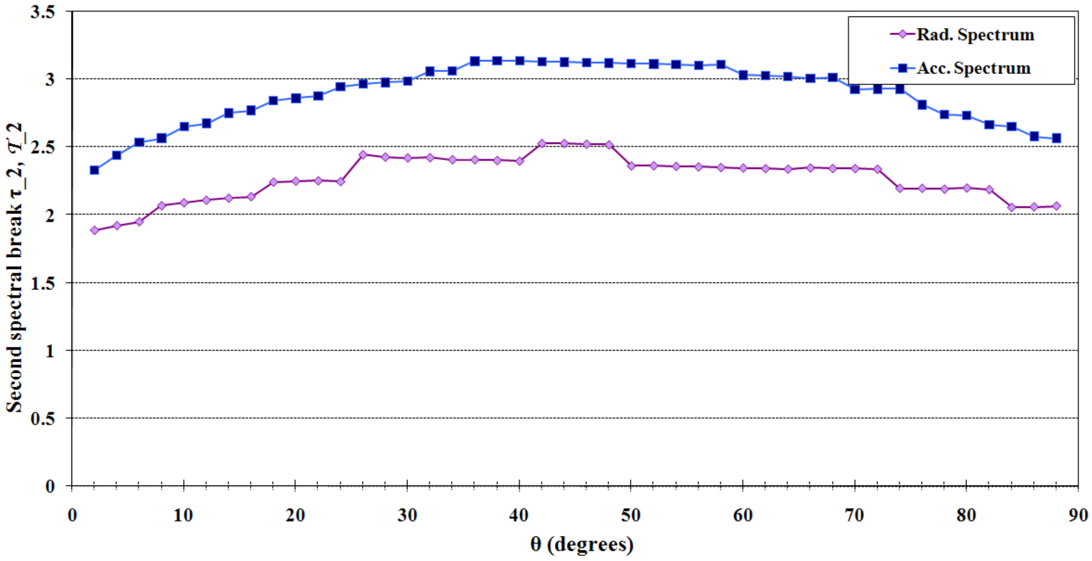

Figure 4.9: The angular dependence of the second spectral break τ_2 of the jitter radiation spectra and $\mathcal{T}_2$ of the acceleration spectra. The transition point is the calculated intersection between the mid-range fit line of slope s_1 (radiation) or $\mathcal{S}_1$ (acceleration) and the high-frequency fit line of slope $-s_2$ (radiation) or $-\mathcal{S}_2)$ (acceleration).

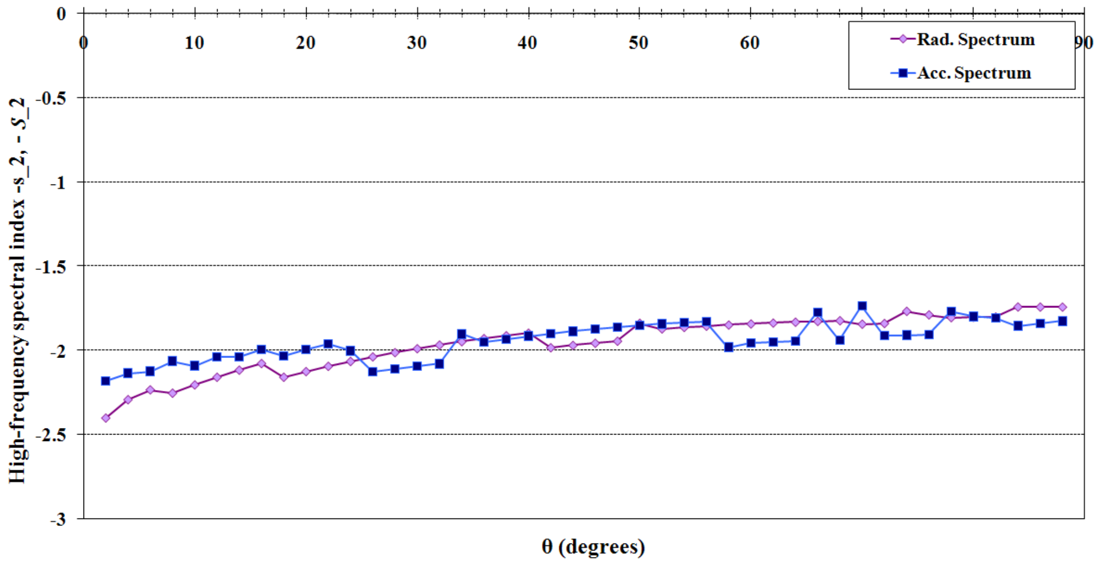

Figure 4.10: The angular dependence of the high-frequency spectral indices s_2 for our calculated jitter radiation spectra and $\mathcal{S}_2$ of the corresponding acceleration spectra. The high-frequency spectral index is calculated as the slope between the drop point (the position of the largest negative change in slope) and the higher-frequency position at which the numerical second derivative is closest to 0.

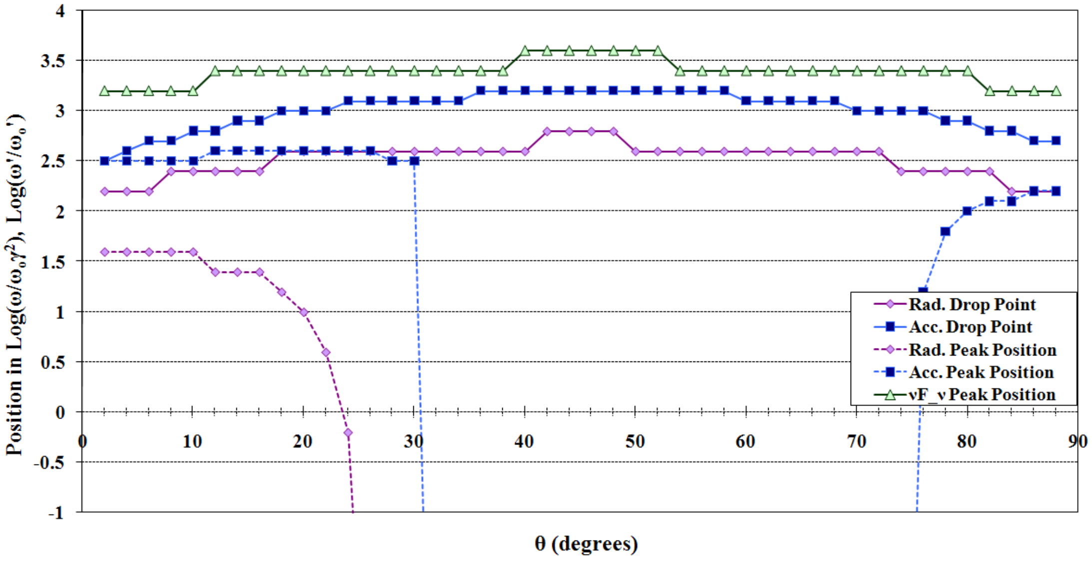

Figure 4.11: A comparison of the angular dependence of the positions of the radiation and acceleration spectral peaks and the spectral drop points, where the numerical second derivatives of our calculated spectra reach a minimum. We have also plotted the angular dependence of the peak in the νF_ν spectrum. The drop point in our F_ν radiation spectrum nicely tracks the behavior of the peak in the νF_ν spectrum, which is peak energy E_p in the Band function [Band et al., 1993] commonly used to fit GRB spectra.

appears to approach different asymptotic values as it approaches $\theta = 0$ and $\theta = \pi/2$, clearly showing the expected $s_1 < 1$ limiting behavior. The second spectral break τ_2 shows that the radiation transition point tends to be about 1/2 a power of e lower than the second spectral behavior for the acceleration case, but shows similar evolution with θ in both cases.

Figure 4.11 shows the angular dependence of the spectral peak in both our acceleration and radiation F_ν spectra, the νF_ν spectral peak (peak data point in Figure 4.5), and the drop point, which we have defined as the minimum in the numerical second derivative. We clearly see the usefulness of the drop point in tracking the spectral behavior across the full range of θ, and that it closely tracks the behavior of the νF_ν spectral

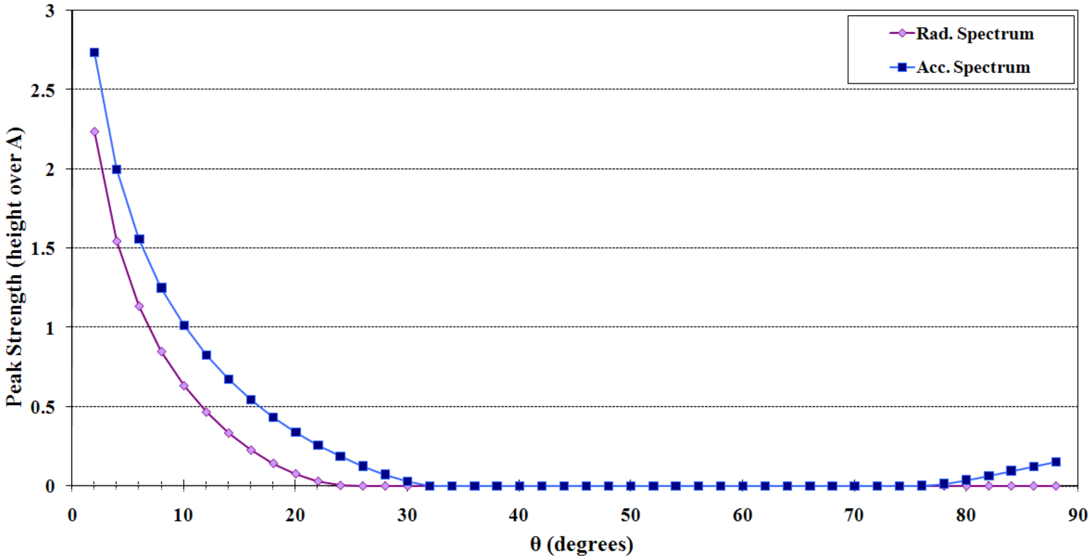

Figure 4.12: The angular dependence of the strength of the spectral peak, i.e. the height of the peak above the initial low-frequency spectral amplitude A. We see that the peak disappears in the radiation spectrum at θ roughly 8° less than in the acceleration spectrum, and does not reappear at θ close to 90°.

peak (E_peak). Both Figures 4.11 and 4.12 clearly show the re-emergence of peaked acceleration spectra as θ approaches $\pi/2$ and the lack of peaked radiation spectra for similar values of θ.

4.4 Incorporating Radiating Region Geometry and the Effects of Its Relativistic Propagation

Because the radiating region is propagating with the relativistic bulk Lorentz factor of the material ejected from the GRB central engine, the radiation emitted within the frame of the propagating material must be properly relativistically transformed in order to produce the radiation spectrum as would be seen by an observer. In the previous section, we presented the jitter radiation spectrum as generated by a particular volume element within the frame of the radiating region, which is part of the relativistically propagating outflow from the GRB central engine. We saw that the spectrum emitted by a particular volume element depends upon the angle θ between the local filamentation axis and the direction to the observer $\hat{\mathbf{n}}$. However, because the radiating region is itself propagating relativistically, the emission into a particular direction $\hat{\mathbf{n}}$ will be redirected by the relativistic Doppler effect. Thus we must correctly develop the relation associating radiation from a particular volume element in the observer's frame with the corresponding spectral form dependent on θ in the co-moving frame. Furthermore, to correctly translate this spectrum from the "co-moving" frame of this propagating slice of the jet to the spectrum as would actually be observed by a distant observer the spectrum's amplitude and frequency dependence must be relativistic transformed from one frame to the other.

The relativistic transformations for radiation produced by an optically thin, relativistically expanding source have been developed elsewhere (see Woods and Loeb [1999], Granot et al. [1999], Ryde and Petrosian [2002], for example). We follow the approach outlined in Woods and Loeb [1999] and Medvedev et al. [2009]. Within the observer frame we assume that our radiating region is a portion of a thin curved shell. The shell can be defined within a spherical coordinate system so that positions on the shell are described by a polar angle θ_{shell} and an azimuthal angle ϕ_{shell}, where we define the $\theta_{shell} = 0$ axis as the direction to the observer. Since the radiating region is likely only a portion of this shell, corresponding to the expected jetted structure of GRBs, we define a jet axis, with the radiating region lies symmetrically within an opening angle of Θ_{jet} around the jet axis. The jet axis will generally not lie along the direction to the observer, so in our geometry we define the angle Θ_{los} between the jet axis and the observer's line of sight. (We use Θ to here to designate angles that are fixed for a particular choice of shell geometry, as distinct from angles θ which vary within any given shell geometry.)

To calculate the observed flux, we want to determine the flux of radiation received by a detector at the observer's position. The energy flux per unit surface area at the detector will be

$$F_{\nu} = \int I_{\nu}(\psi, \phi) \cos \psi d\Omega \approx \int d\phi I_{\nu}(\psi, \phi) \psi d\psi \tag{4.2}$$

where ψ is the angle between an incident ray and the normal to the detector plane, $I_{\nu}(\psi, \phi)$ is the intensity (as a function of frequency ν) of a ray incident on the detector from the direction from the direction (ψ, ϕ) and $d\Omega = \sin \psi d\psi d\phi$ is the differential solid angle of the emitting region. If we presume the detector is at a large distance d so that $d \gg r$ and is oriented nearly orthogonal to the line of sight, we can make the approximations $\cos\psi \approx 1$, $\sin\psi \approx \psi$, and $\psi \approx r\sin\theta/d$. Defining $\mu = \cos\theta$ so that $\psi d\psi = (-r^2/d^2)\mu d\mu$ we obtain

$$F_\nu = \int I_\nu(\psi,\phi)\left(-\frac{r^2}{d^2}\right)\mu d\mu d\phi \tag{4.3}$$

If we define a volume emissivity j_ν for the emitting region, the intensity along a ray from a particular direction (ψ,ϕ) as produced by a path length element $ds = (r^2 d\theta^2 + dr^2)^{1/2}$ measured in the observer frame, is given by

$$I_\nu(\psi,\phi) = \int dI_\nu = \int j_\nu ds \tag{4.4}$$

If our thin spherical shell is expanding radially with local velocity $\beta_{bulk} = v_{bulk}/c$, this leads to a bulk Lorentz factor of $\Gamma = (1-\beta_{bulk}^2)^{-1/2}$. In principle the Lorentz factor may vary across the shell surface, particularly relative to the central jet axis; we can incorporate different bulk Lorentz factor profiles in our model to account for this possibility. To relativistically transform the energies from the emitting shell's co-moving frame into the observer's frame, we use the relativistic Doppler boost factor

$$D = \frac{1}{\Gamma(1-\beta_{bulk}(\boldsymbol{e}_{obs}\cdot\boldsymbol{e}_{vel}))} \tag{4.5}$$

where $\boldsymbol{e}_{obs}$ is a unit vector in the direction of the observer and $\boldsymbol{e}_{vel}$ is a unit vector in the direction of the relativistic velocity producing the boost. For our scenario, θ_{shell} is the angle between the local direction of propagation for our relativistically expanding radiating shell and the direction to the observer, so $\boldsymbol{e}_{obs}\cdot\boldsymbol{e}_{vel} = \cos\theta_{shell} = \mu$.

Defining primed quantities as those in the co-moving frame and unprimed quantities as those in the observer's frame, we can similarly define $\cos\theta'_{shell} = \mu\prime$. Relativistic angle aberration relates the angles θ_{shell} and θ'_{shell} such that

$$\mu' = \frac{\mu - \beta_{bulk}}{1 - \beta_{bulk}\mu} \tag{4.6}$$

The Doppler boosting factor can then be written in terms of either μ or $\mu\prime$ as

$$D(\mu) = \frac{1}{\Gamma(1 - \beta_{bulk}\mu)} = \Gamma(1 + \beta_{bulk}\mu') \tag{4.7}$$

The energies then transform as

$$\nu = \nu' D_{obs} = \frac{\nu'}{\Gamma(1 - \beta\mu)} \tag{4.8}$$

where primed quantities again denote values in the co-moving frame, and unprimed quantities are values in the frame of observation. To relate the volume emissivities in the co-moving and observer frames, we can use the Lorentz invariance of the quantity $j_\nu/\nu^2 = j'_{\nu'}/\nu'^2$ and the substitution $ds \approx dr/\mu$ to obtain

$$dI_\nu = j_\nu ds = j'_{\nu'} D(\mu)^2 dr/\mu \tag{4.9}$$

We have defined the co-moving frame volume emissivity $j'_{\nu'}(r', \theta'_{shell}, \phi'_{shell}, t)$ as a function of a location $(r', \theta'_{shell}, \phi'_{shell})$ of the radiating region and time t. The emissivity will be a product of the number density of radiating electrons n'_e (assumed to isotropic across the shell) and the ensemble-averaged spectral power per electron $P(\nu', \theta'_{shell}, t)$. The spectral power from a particular portion of the curved radiating surface at $(r', \theta'_{shell}, \phi'_{shell})$ has a form that depends upon the earlier-defined angle θ between the local filamentation axis $\hat{\mathbf{s}}$ and the direction of emission $\hat{\mathbf{n}}$ in the co-moving frame. If we assume a simple spherical geometry for the radiating region in the co-moving frame, where the radiating shell has a constant radius of curvature R, and that the local filamentation axis $\hat{\mathbf{s}}$ is aligned with the local normal to the spherical shock front $\hat{\mathbf{N}}_{shock}$, then θ'_{shell} is equal to θ. The angle θ'_{shell} transforms to the observer frame via Equation 4.6, and $\phi' = \phi$. The volume emissivity in the co-moving frame is thus

$$j'_{\nu'}(r', \theta'_{shell}, \phi'_{shell}, t) = n'_e P(\nu', \theta, t) \tag{4.10}$$

Differences in travel time for emission from different portions of the shell mean that an observer will receive a time-dependent spectrum even if the shell radiates at a single emission time t_{em}. In the observer frame, the photon arrival time t is related to the emission time t_{em} as $t = t_{em} - r\mu/c$, with constants eliminated so that $t = 0$ is for a photon emitted from the origin of our spherical coordinate system at time t_{em}.

To obtain the correct flux F_ν as a function of time, we must also consider the jet geometry and the contribution each emitting "slice" of our radiating shell will make due to its volume. For an infinitesimally thin shell, this translates into an illumination that progresses from a circular area at the leading edge through annuli of successively larger apparent radii, each defined by a small range of angles in θ_{shell} and contributing the corresponding relativistically transformed spectral form times a factor proportional to the radiating surface area. Because of the offset between the jet axis and the observer's line of sight, at a certain angle $\theta_{shell} = \Theta_{jet} - \Theta_{los}$, the effective "radiating annuli" will be cut off by the edge of the jet. We numerically identify the limits on ϕ_{shell} for such values of θ_{shell} to ensure remain within the jet cone.

Incorporating all relativistic and geometric effects, the resulting flux per frequency received by an observer at time t from our illuminated jet front is

$$F_\nu(t) = F_0 D^2(t) P(\nu'(t), \mu'(t))(\phi_2(t) - \phi_1(t)) \tag{4.11}$$

Our θ-dependent jitter radiation spectra in the co-moving frame can thus be transformed into a time-evolving radiation spectrum in the observer's frame. A full GRB can be simulated as a series of similar contributions by multiple radiating shells with a distribution of illumination times and peak energies taken from the statistics of actual GRB observations. A "simulated GRB" built up in this fashion can be sampled and binned as it would be by BATSE or another detector and the results analyzed statistically for comparison with observations. This work is undertaken and explored in detail in the related thesis [Pothapragada, 2012] by our collaborator.

4.5 Discussion of Results

We have calculated the angle-averaged power spectra of jitter radiation emitted by *a single relativistic electron* undergoing small Lorentz-force accelerations transverse to its overall velocity. The resulting spectra are equivalent to the ensemble-averaged spectra per electron from a monoenergetic delta-function distribution of relativistic electrons. Our results are based on smoothly broken power-law distributions of magnetic field wavenumber along and transverse to filamentation produced by the Weibel-like filamentation instability. The shapes of the resulting jitter radiation spectra are shown to depend on the underlying magnetic field distributions and to vary with the angle θ between the electron velocity (being also the line of sight) with respect to the direction of the field anisotropy due to filamentation.

The power (i.e., F_ν) spectrum produced by monoenergetic electrons moving towards the observer with the Lorentz factor γ, in general, has three power-law segments: a flat low-energy part, an intermediate-energy region which rises or slightly falls with a slope of less than unity (the exact value depending on θ), and a more steeply declining high-energy region. The shape of the spectrum changes significantly with the angle θ

between the radiating particle's velocity and the axis of the current filamentation generated by the counterstreaming Weibel instability. As $\theta \to 0^\circ$, the low-frequency spectral break τ_1 approaches $-\infty$ and the maximum spectral slope (mid-range spectral index s_1 approaches the value of 1 (the trend of our results agreeing well with the $\theta = 0^\circ$ case in Medvedev [2006]). As θ increases, the spectral peak weakens as s_1 decreases and τ_1 shifts towards the peak region. The disappearance of the spectral peak at some particular θ appears to be a result of both these spectral changes, and there is an extended transition region between the low-energy and high-energy power law trends. Consequently, we find that both the peaked and unpeaked spectra are well described by a three-region fit. Two-region fits (which are common in GRB analysis) are likely to miss out on the variation in the spectral slope below the peak at small θ; consequently the resulting low-energy spectral index will depend on where the peak falls relative to the lower bound of a measured spectral window. This will be true even if the low-energy spectral index is taken at a common energy, as in the "effective" low-energy spectral index α_{eff} commonly taken as the tangential slope of the logarithmic spectrum at 25 keV.

In comparing the radiation spectra for the full range of θ, we have found that the "drop point", which we determined as the minimum of the numerical second derivative of the logarithmic data (i.e. the largest negative change in the spectral slope) serves as a good common reference point for both peaked and unpeaked spectra; in addition, the "drop point" in the radiation power spectrum evolves with the angle θ much like the νF_ν spectral peak energy E_p.

The jitter radiation spectra are significantly harder than synchrotron spectra in the region just below the spectral peak. This may be a significant mechanism in explaining the substantial population of gamma-ray burst spectra which appear to violate the synchrotron limit. If we consider emission from a curved shell with a filamentary structure aligned everywhere along the normal to the shell (such as may be produced by a curved propagating shock front, then the leading edge of the shell, where emission energy is most boosted will also be where the effective angle for our jitter radiation spectrum is $\theta = 0^\circ$. The progression of θ with the viewing angle to more distant portions of the shell would lead to a rapid hard-to-soft evolution in the spectrum from a single radiating shell and to an overall tracking behavior between the hardness of the low-energy spectral index (or equivalently the photon index α_{ph} and the flux at peak energy $F_\nu(E_{peak})$. Both of these are key trends noticed in analysis of time-resolved GRB spectra, suggesting that jitter radiation and small-scale magnetic field turbulence may indeed play a key role in the production of GRB prompt emission.

Chapter 5

Further Explorations of Jitter Radiation Spectra

5.1 Summary

We have presented the spectrum results obtained using the angle-resolved (Chapter 3) and the angle-averaged (Chapter 4) jitter radiation equations. In both cases, the spectrum depends directly upon the accelerations undergone by the particle population radiating into the direction of an observer. These accelerations are a result, via the Lorentz force, of the magnetic field strengths and orientations as encountered along the particle's path. Based on the anisotropy generated by the Weibel-type filamentation instability, we have defined the magnetic field in the radiating region via magnetic wavenumber distributions that are independent along and transverse to the filamentation axis. The jitter radiation spectrum results presented in preceding chapters have been obtained using a particular form and choice of parameters of the magnetic field distribution. In this chapter we further develop the connection between the choice of parameters in these field distributions and the spectral features of the angle-averaged and angle-resolved jitter radiation results.

5.2 Characterizing the Jitter Radiation Spectrum

From Chapter 2, the angle-averaged emissivity of a relativistic particle undergoing a series of small transverse accelerations not substantially affecting its overall velocity is as follows:

$$\frac{dW}{d\omega} = \frac{e^2\omega}{2\pi c^2}\int_{\omega/2\gamma^2}^{\infty} \frac{|\mathbf{w}_{\omega'}|^2}{\omega'^2}\left(1 - \frac{\omega}{\omega'\gamma^2} + \frac{\omega^2}{2\omega'^2\gamma^4}\right) d\omega' \tag{5.1}$$

The ω dependence contributed by the integral primarily originates in the lower limit $\omega/(2\gamma^2)$ and where it falls on the acceleration spectrum. In Chapter 3, section 3.3, we found that the acceleration spectrum could be simply characterized as three regions of approximately power-law behavior: a flat initial amplitude at low $\log\omega'$ (Region I), a region of positive or negative slope (Region II), and a region with a more steeply negative slope (Region III) (as was shown in Figure 5.1). Using this to make a simple approximation for our acceleration spectrum in three regions, we can calculate an approximate analytical solution to equation 5.1.

We can define our simple approximation to the acceleration spectrum using five free parameters, all of which may be fit to the spectrum on a $\log_e - \log_e$ plot: $\mathcal{A} = \log a_0$ is the amplitude of the low-ω' limit; $\mathcal{T}_1 = \log\omega'_1$ is the transition point between the first and second regions; $\mathcal{S}_1$ is the spectral index in the second region; $\mathcal{T}_2 = \log\omega'_2$ is the transition point between the second and third regions; and $-\mathcal{S}_2$ is the spectral index in the third region ($\mathcal{S}_2 > 0$). One method for performing such a fit to our data was outlined in Chapter 4, section 4.3.2. The acceleration spectrum then has the form:

$$\begin{aligned}
&\text{for } \omega' < e^{\mathcal{T}_1} : \\
&\qquad \left\langle |\mathbf{w}_{\omega'}|^2 \right\rangle = e^{\mathcal{A}} = a_0, && (5.2)\\
&\text{for } e^{\mathcal{T}_1} < \omega' < e^{\mathcal{T}_2} : \\
&\qquad \left\langle |\mathbf{w}_{\omega'}|^2 \right\rangle = e^{\mathcal{A}-\mathcal{S}_1\mathcal{T}_1}\omega'^{\mathcal{S}_1} = a_0\left(\frac{\omega'}{\omega'_1}\right)^{\mathcal{S}_1}, && (5.3)\\
&\text{for } \omega' > e^{\mathcal{T}_2} : \\
&\qquad \left\langle |\mathbf{w}_{\omega'}|^2 \right\rangle = e^{\mathcal{A}+\mathcal{S}_1\mathcal{T}_2-\mathcal{S}_1\mathcal{T}_1+\mathcal{S}_2\mathcal{T}_2}\omega'^{-\mathcal{S}_2} = a_0\left(\frac{\omega'_2}{\omega'_1}\right)^{\mathcal{S}_1}\left(\frac{\omega'}{\omega'_2}\right)^{-\mathcal{S}_2} && (5.4)
\end{aligned}$$

Figure 5.1 shows example models for the acceleration spectra at θ = 10 degrees and θ = 60 degrees and their comparison to the original acceleration spectra (as in Figure 3.1) for our previously-defined choice of fitting rules.

To first order (neglecting the second and third terms in Eq. 5.1), the resulting angle-averaged radiation spectrum is as follows:

$$\begin{aligned}
&\text{for } \omega/2\gamma^2 < e^{\mathcal{T}_1} : \\
&\left(\frac{dW}{d\omega}\right)_I = \frac{e^2}{2\pi c^2}e^{\mathcal{A}}\left[(2\gamma^2) - \omega\frac{\mathcal{S}_1 e^{-\mathcal{T}_1}}{\mathcal{S}_1-1} + \omega\frac{(\mathcal{S}_1+\mathcal{S}_2)e^{-\mathcal{T}_1\mathcal{S}_1+\mathcal{T}_2(\mathcal{S}_1-1)}}{(\mathcal{S}_1-1)(\mathcal{S}_2+1)}\right] \\
&\qquad = \frac{a_0 e^2}{2\pi c^2}\left[2\gamma^2 - \frac{\mathcal{S}_1}{\mathcal{S}_1-1}\left(\frac{\omega}{\omega'_1}\right) + \frac{\mathcal{S}_1+\mathcal{S}_2}{(\mathcal{S}_1-1)(\mathcal{S}_2+1)}\left(\frac{\omega'_2}{\omega'_1}\right)^{\mathcal{S}_1}\left(\frac{\omega}{\omega'_2}\right)\right], && (5.5)\\
&\text{for } e^{\mathcal{T}_1} < \omega/2\gamma^2 < e^{\mathcal{T}_2} : \\
&\left(\frac{dW}{d\omega}\right)_{II} = \frac{e^2}{2\pi c^2}e^{\mathcal{A}-\mathcal{T}_1\mathcal{S}_1}\left[\frac{-\omega^{\mathcal{S}_1}}{(\mathcal{S}_1-1)(2\gamma^2)^{\mathcal{S}_1-1}} + \omega\left(\frac{1}{\mathcal{S}_1-1}+\frac{1}{\mathcal{S}_2+1}\right)e^{\mathcal{T}_2(\mathcal{S}_1-1)}\right] \\
&\qquad = \frac{a_0 e^2}{2\pi c^2}\left[-\frac{(2\gamma^2)^{1-\mathcal{S}_1}}{(\mathcal{S}_1-1)}\left(\frac{\omega}{\omega'_1}\right)^{\mathcal{S}_1} + \frac{\mathcal{S}_1+\mathcal{S}_2}{(\mathcal{S}_1-1)(\mathcal{S}_2+1)}\left(\frac{\omega'_2}{\omega'_1}\right)^{\mathcal{S}_1}\frac{\omega}{\omega'_2}\right], && (5.6)\\
&\text{for } \omega/2\gamma^2 > e^{\mathcal{T}_2} : \\
&\left(\frac{dW}{d\omega}\right)_{III} = \frac{e^2}{2\pi c^2}e^{\mathcal{A}-\mathcal{T}_1\mathcal{S}_1+\mathcal{T}_2(\mathcal{S}_1+\mathcal{S}_2)}\frac{(2\gamma^2)^{1+\mathcal{S}_2}}{|\mathcal{S}_2+1|}\omega^{-\mathcal{S}_2} \\
&\qquad = \frac{a_0 e^2}{2\pi c^2}\frac{(2\gamma^2)^{1+\mathcal{S}_2}}{|\mathcal{S}_2+1|}\left(\frac{\omega'_2}{\omega'_1}\right)^{\mathcal{S}_1}\left(\frac{\omega}{\omega'_2}\right)^{-\mathcal{S}_2} && (5.7)
\end{aligned}$$

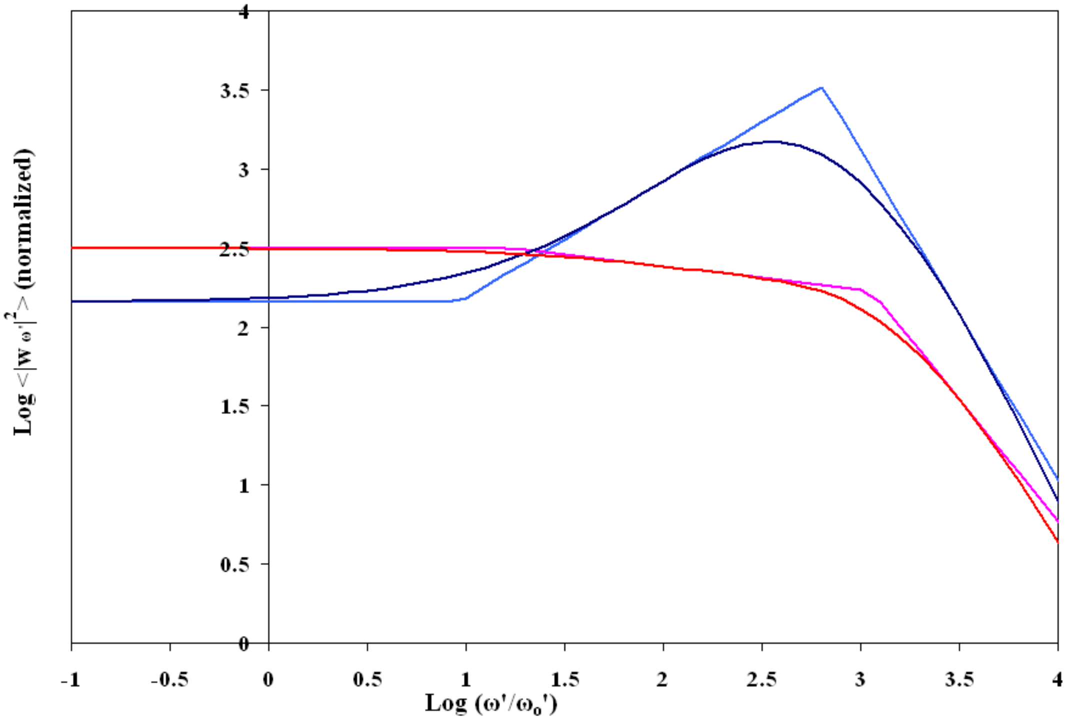

Figure 5.1: Here we show a comparison of our original calculated acceleration (angle-resolved) spectra (as presented in Figure 3.1) for θ=10 (peaked) and θ=60 (unpeaked), and our model acceleration spectra as described in Equations 5.2-5.4. In Region I, we extrapolate the initial calculated amplitude. In Region II, we fit the calculated spectra using the maximum slope in the region and fitting through the point of maximum slope or by taking the average slope between the "deflection point" and "drop point" as defined in Chapter 4, section 4.3.2. In Region III we have done a simple fit using the slope and position at a fixed point in this region. Our choice of fit here focuses on accuracy of the spectral indices, but is less accurate on the peak height and peak/break position in the calculated acceleration spectra.

The angle-averaged radiative power spectrum (equations (5.5) - (5.7)) obtained analytically by our fit-based approximation for the acceleration spectrum agrees with that obtained via full numerical integration in the following section within about 10%. We have chosen our fitting method for the acceleration spectrum to most closely capture the spectral indices; a different choice of fit may allow for a better determination of peak positions.

Calculations of the angle-averaged spectrum for parameters fitted to our acceleration spectra at $\theta = 10^\circ$ and $\theta = 60^\circ$ are shown in Figures 5.2 and 5.3. The region boundaries in these figures indicate that the radiation spectrum cannot be described by a simple linear approximation in the three regions that were defined by the breaks in our acceleration spectrum. The key features (position of spectral peak and spectral breaks) of the radiation spectrum originate in the additional terms in Equations 5.5 and 5.6. Consequently, the transition points in our radiation spectrum do not directly correspond to the transition points in the acceleration spectrum.

The asymptotic behavior of the spectrum at high and low energies can be easily obtained from Equations 5.5 and 5.7:

$$\text{for } \omega/2\gamma^2 < \omega_1' :$$

$$\left(\frac{dW}{d\omega}\right)_I \propto \omega^0, \tag{5.8}$$

$$\text{for } \omega/2\gamma^2 > \omega_2' :$$

$$\left(\frac{dW}{d\omega}\right)_{III} \propto \omega^{-s_2} \tag{5.9}$$

Thus the high and low-energy asymptotic behavior of the radiation spectrum will be identical to the high and low-energy behavior of the acceleration spectrum.

The behavior of the spectrum in the intermediary Region II can also be obtained. We take the derivative of Equation 5.6 to solve for the position $P = \log(\omega_p/2\gamma^2)$ of the

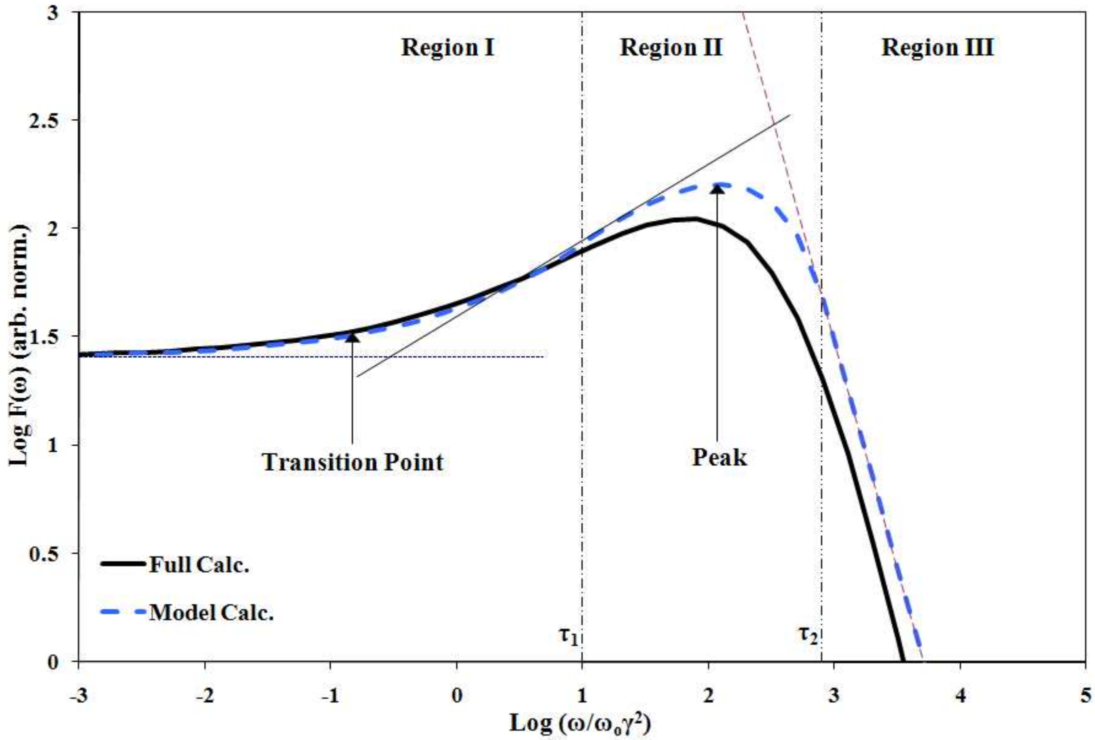

Figure 5.2: The radiation spectrum for θ=10 degrees as obtained analytically using equations 5.5 - 5.7 and the fit values for the model acceleration spectra as shown in Figure 3.5. The result calculated (black) via full double numerical integration (as in Figure 4.3) is shown here for comparison. The spectral transition point defined by Equation 5.12 and the peak defined by Equation 5.10 are marked with arrows. We note that the boundaries (dotted lines) between Regions I, II, and III as defined by our model acceleration spectra do not clearly correspond to transition points in the resulting radiation spectra. We have extrapolated slopes for Regions I, II, and III to demonstrate the variation. The model again slightly overestimates the peak energy, but matches the spectral shape well and agrees with the integrated spectra within about 10%.

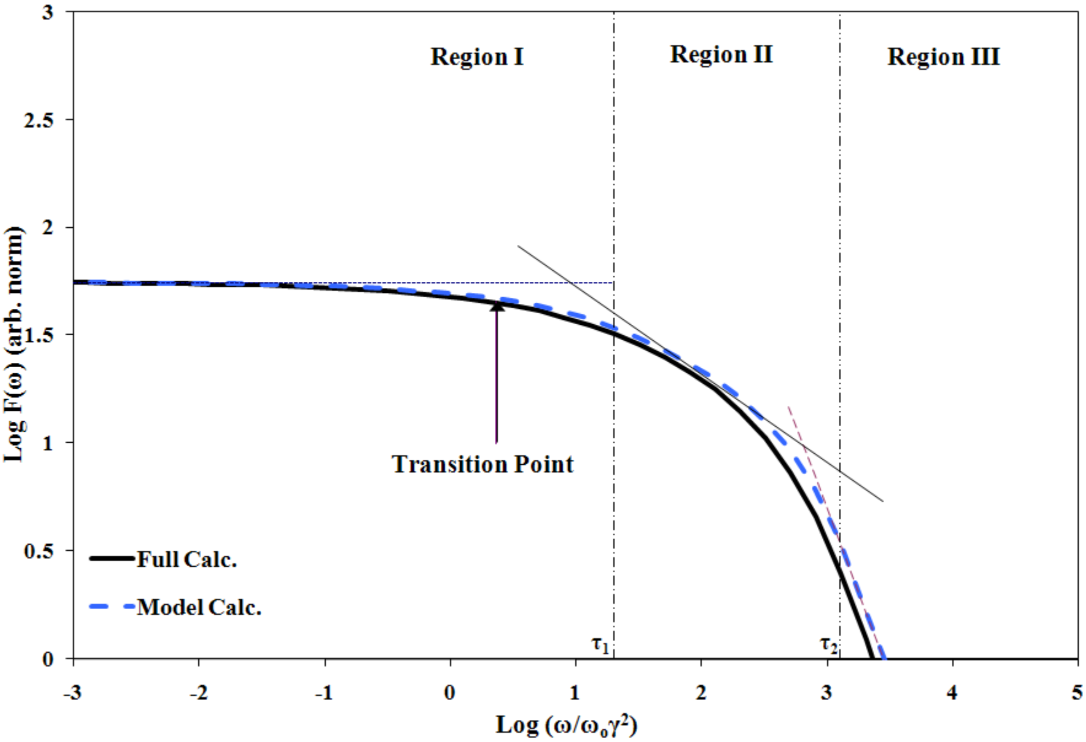

Figure 5.3: The radiation spectrum for θ=60 degrees as obtained analytically from our simplified model acceleration spectrum (as shown in Figure 3.5) versus the full double numerical integration result (black). As in the previous figure, we have extrapolated the slope in Regions I, II, and III. We again obtain a good agreement with the overall spectral shape, but now with an unpeaked form appropriate to this range of theta. The spectral transition point defined by Equation 5.12 is marked with an arrow.

spectral peak, in cases where it exists:

$$P = \frac{1}{1-\mathcal{S}_1} \log\left[\frac{\mathcal{S}_1(\mathcal{S}_2+1)}{\mathcal{S}_1+\mathcal{S}_2}\right] + \mathcal{T}_2 \tag{5.10}$$

We note that the peak position becomes undefined in the case $\mathcal{S}_1 < 0, |\mathcal{S}_1| > \mathcal{S}_2$, for which Equation (5.6) is everywhere decreasing. The case $\mathcal{S}_1 < 0, |\mathcal{S}_1| < \mathcal{S}_2$, in which the acceleration spectrum would decline more steeply in Region II than in Region III is impermissible, so we find that the radiation spectrum will be unpeaked whenever the mid-range spectral index $\mathcal{S}_1$ of the acceleration spectrum is negative (i.e., for $\mathcal{S}_1 < 0$).

An exploration of the behavior of peak point P relative to the region boundaries shows that for certain values of θ the peak of the Region II function exists, but has crossed the boundary into Region I and consequently does not appear in the resulting radiation spectrum. Thus, while a calculation of P from the results of fitting the acceleration spectrum appears to indicate the re-emergence of a peak in the radiation spectrum as θ approaches $\pi/2$, this peak falls beyond the Region II lower boundary and is not observed. We note that the first term in Equation 5.10 is negative for both $0 < \mathcal{S}_1 < 1$ and $\mathcal{S}_1 > 1$, so the peak is always located below the transition point between Regions II and III.

An analysis of the behavior of Equation(5.6) below the Region II peak indicates the following behavior:

$$\text{for } \omega_1' < \omega/2\gamma^2 < \omega_2' : \left(\frac{dW}{d\omega}\right)_{II} \propto \begin{cases} \omega^1 & if \mathcal{S}_1 > 1, \\ \omega^{\mathcal{S}_1} & if \mathcal{S}_1 < 1, \end{cases} \tag{5.11}$$

Thus, from Equations 5.8-5.11, it is evident that the spectral indices $\mathcal{S}_1$ and $\mathcal{S}_2$ of the acceleration spectra will generally correspond to spectral indices s_1 and s_2 in two power law regions of the radiation spectra. In the case of the high-frequency spectral index s_2 this correspondence is exact; however, the relation between mid-range (i.e. intermediate-frequency) spectral indices s_1 and $\mathcal{S}_1$ is modified an upper limit of unity on s_1 and also breaks down when the first term in equation 5.10 is undefined or larger in magnitude than the distance between the acceleration's spectral transition points $\mathcal{T}_2 - \mathcal{T}_1$.

The asymptotic form in Equation 5.8 suggests that we may neglect the second and third terms in Equation 5.5 and solve for the transition point $T = \log(\omega_t/2\gamma^2)$ at which the dominating term in Region II becomes significant. We find that:

$$\begin{aligned}
&\text{for } \mathcal{S}_1 < 1: \\
&\qquad \left(\frac{\omega_t}{2\gamma^2}\right)^{\mathcal{S}_1} &&= (1-\mathcal{S}_1)\omega_1'^{\mathcal{S}_1} \\
&\qquad T &&= \frac{1}{\mathcal{S}_1}\log(1-\mathcal{S}_1) + \mathcal{T}_1, \qquad (5.12) \\
&\text{for } \mathcal{S}_1 > 1: \\
&\qquad \left(\frac{\omega_t}{2\gamma^2}\right)^{\mathcal{S}_1} &&= \frac{(\mathcal{S}_1-1)(\mathcal{S}_2+1)}{\mathcal{S}_1+\mathcal{S}_2}\left(\frac{\omega_1'^{\mathcal{S}_1}}{\omega_2'^{(\mathcal{S}_1-1)}}\right) \\
&\qquad T &&= \log\left[\frac{(\mathcal{S}_1-1)(\mathcal{S}_2+1)}{\mathcal{S}_1+\mathcal{S}_2}\right] + \mathcal{S}_1\mathcal{T}_1 + (\mathcal{S}_1-1)\mathcal{T}_2 \qquad (5.13)
\end{aligned}$$

We have demonstrated that a simple approximation for our acceleration spectrum allows us to analytically obtain some of the key features of the resulting jitter radiation spectrum, notably that it will have a similar three-region form with $dW/d\omega \propto \omega^0$ for small ω and $dW/d\omega \propto \omega^{-s_2}$ for large ω and a possibly-peaked transition region. Unlike the acceleration spectrum, the intermediary region in the jitter radiation spectrum will have a maximum slope of 1 and may be unpeaked at angles θ at which the acceleration spectrum was peaked. We emphasize that our spectral calculations are all for a single emitting electron, *not* a power-law distribution of electrons. Yet, the power-law photon spectrum emerges at high energies (above the second jitter spectral break ω_2) in this jitter mechanism, in contrast to the synchrotron exponential spectral decay above the synchrotron frequency.

5.3 Spectral Features and Exploration of the Spectral Parameter Space

We have explored the influence of changes in the magnetic field spectral parameters on the acceleration experienced by the particle and hence its resulting radiative profile. Chapters 3 and 4 presented the angle-resolved and angle-averaged radiation spectra calculated from magnetic field spectra of the form given in Equations 2.19 and 2.20 with our original choice of parameters $\alpha = \alpha_{\perp} = \alpha_{\parallel} = 2.0$, $\beta = \beta_{\perp} = \beta_{\parallel} = 1.5$, $\kappa = \kappa_{\perp} = \kappa_{\parallel} = 10$. In this section, we present the results of varying these parameters. We vary the joint parameters α, β, and κ in the parallel and perpendicular magnetic field spectra. We also vary the parameters $\alpha_{\parallel}$, $\alpha_{\perp}$, $\beta_{\parallel}$, and $\beta_{\perp}$ individually. Finally, we vary the ratio $K = \kappa_{\perp}/\kappa_{\parallel}$. For each variation of the initial parameters, we have calculated the radiation spectrum for three representative angles at $\theta = 10^{\circ}$, 45°, and 80°. The results are presented according to their impact on the characteristics of the radiation spectrum as developed in section 5.2, namely the initial amplitude A, the spectral breaks τ_1 and τ_2, and the spectral indices s_1 and s_2. We also present the results for the peak “strength”, the height of the spectral peak above the initial amplitude.

The spectra are divided by $\langle B^2 \rangle \propto \int f(k_{\parallel}) f_(k_{\perp}) d^3\mathbf{k} \propto k_0^{-2(\beta_{\parallel}+\beta_{\perp})}$ to appropriately normalize the amplitudes relative to one another, but in all cases we have arbitrarily normalized the final spectra such that the low-energy asymptotic value of the $\theta = 10$ spectrum with our original choice of parameters is unity (zero on the logarithmic scale).

As in Chapter 4, Section 4.3.2, the initial, low-frequency amplitude A is the first calculated value of the angle-averaged radiative power emitted per frequency $dW/d\omega$. This value is generally a good approximation for the asymptotic value of the function as it approaches lower ω, though it may deviate somewhat from this value for θ approaching 0, as the spectra becomes sloped rather than flattened at our lower calculation boundary in ω.

Among the resulting figures 5.4-5.7, variations in the magnetic field parameters κ_i produce the largest effect on the low-frequency amplitude, causing changes of about 4 orders of magnitude in e when varied individually via the ratio $K = \kappa_{\perp}/\kappa_{||}$, and up to 7 orders of magnitude in e when varied together as $\kappa = \kappa_{||} = \kappa_{\perp}$. Variation with changes in the magnetic field spectral indices α_i and β_i are small in comparison, on the scale of about 1-2 orders of magnitude. The amplitude increases with increasing K for $\theta = 10^\circ$ and generally decreases with increasing K for $\theta = 80^\circ$; thus, it increases when $\kappa_{\perp}$ dominates at small θ and when $\kappa_{||}$ dominates at large θ.

The mid-range spectral index in peaked spectra is the maximum slope below the peak, as determined by taking the numerical first derivative of our calculated values. For unpeaked spectra, we find the spectral index as the average slope between the point at which the graph deviates by more than 0.01 from the initial amplitude A and the drop point at which the numerical second derivative reaches a minimum.

Figures 5.8-5.10 present the effect of magnetic field parameter variations on s_1. As can be seen in Figure 5.11, the mid-range spectral index is strongly affected by variations in both the parameters β_i, especially for $\theta = 10^\circ$, and in the relative strength of the κ_i values. The peaked $\theta = 10^\circ$ spectra is notably more sensitive to magnetic field variations than the unpeaked 45° and 80° spectra. The ratio $K = \kappa_{\perp}/\kappa_{||}$ has the largest influence at all three representative viewing angles, with s_1 increasing as $\kappa_{||} > \kappa_{\perp}$). We

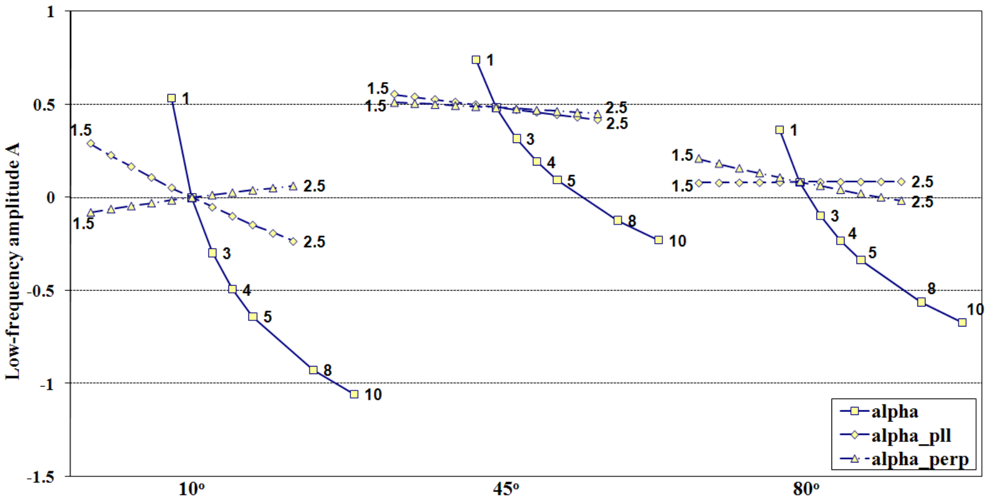

Figure 5.4: This figure shows the variation of the low-frequency amplitude of the radiation spectrum (vertical axis) with changes in the magnetic field parameters α_i, which are varied progressively in the horizontal dimension as described below, for each of the fixed viewing angles $\theta = 10^\circ$, 45°, and 80° (first, second, and third clusters respectively). The solid line with square data points indicates the behavior when α is jointly varied (over a range from 1 to 10, as indicated) in both the transverse and parallel magnetic field equation: $\alpha = \alpha_\perp = \alpha_\parallel$. The dotted lines show the effect of individually varying $\alpha_\perp$ (triangular data points) and $\alpha_\parallel$ (diamond data points), which chracterize the magnetic field transverse to and along the instability filamentation axis, respectively. The parameters $\alpha_\perp$ and $\alpha_\parallel$ are varied from a starting value of 1.5 to an ending value of 2.5, in increments of 0.1. Our original value of $\alpha = \alpha_\perp = \alpha_\parallel = 2.0$ is the central data point where the lines intersect.

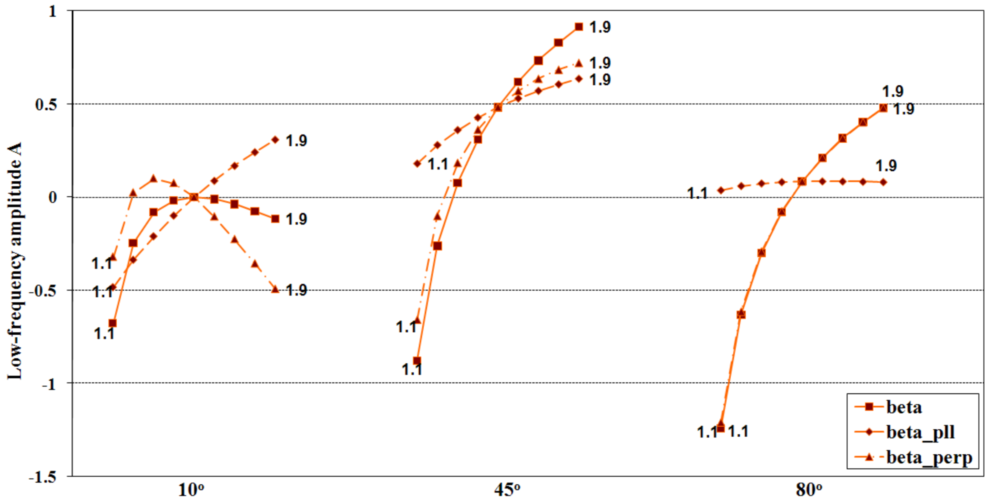

Figure 5.5: This figure shows the variation of the low-frequency amplitude of the radiation spectrum (vertical axis) with changes in the magnetic field parameters β_i, which are varied progressively in the horizontal dimension for the fixed viewing angles $\theta = 10^\circ$, 45°, and 80° (first, second, and third clusters respectively). The solid line with square data points indicates the behavior when β is jointly varied from 1.1 to 1.9, in increments of 0.1, in both the transverse and parallel magnetic field equation: $\beta = \beta_\perp = \beta_\|$. The dotted lines show the effect of varying $\beta_\perp$ (triangular data points) and $\beta_\|$ (diamond data points) individually, also from 1.1 to 1.9, in increments of 0.1. Our original value of $\beta = \beta_\perp = \beta_\| = 1.5$ is the central data point where the lines intersect.

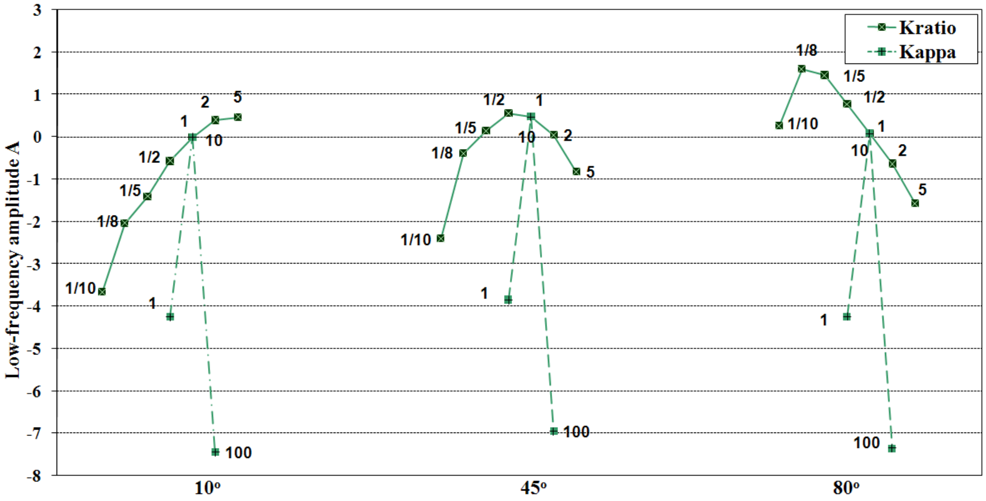

Figure 5.6: This figure shows the variation of the low-frequency amplitude of the radiation spectrum with changes in the magnetic field parameters κ, which are varied progressively in the horizontal dimension for the fixed viewing angles $\theta = 10°$, $45°$, and $80°$ (first, second, and third clusters respectively). We vary κ jointly ($\kappa = \kappa_\perp = \kappa_\|$) by powers of 10, from 1 to 100, as indicated. We also vary $\kappa_\perp$ and $\kappa_\|$ relative to one another by changing the ratio $K = \kappa_\perp/\kappa_\|$ through a range of values as indicated.

note that even at θ approaching $\pi/2$, we obtain a positive slope (and hence a peaked spectrum) for $K = 1/10$.

For both peaked and unpeaked forms, the high-frequency spectral index -s_2 is determined by taking the slope between the drop point and the absolute minimum of the second derivative above the peak (i.e., the closest data point to where the second derivative crosses zero). Figures 5.12 - 5.14 show the effects of variations in the magnetic field parameters on -s_2. We find that as expected analytically, this spectral index is primarily influenced by the magnetic field parameters β_i. In particular, s_2 is most strongly influenced by $\beta_\perp$, the high-wavenumber spectral index of the magnetic field spectrum transverse to the current filamentation. As seen in figure 5.13, $\beta_\|$ affects s_2 only at small angles θ, and its influence even then is less than that of varying $\beta_\perp$. The apparently strong influence of κ is largely an artificial effect as the κ parameter's strong

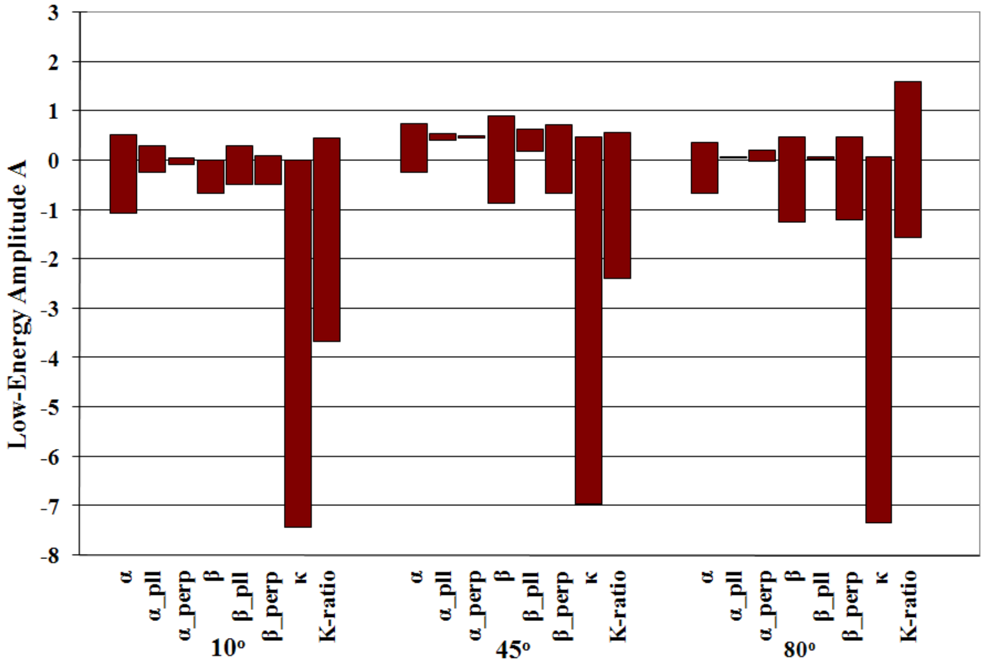

Figure 5.7: This figure compares the influences of the magnetic field spectral parameter variations on the low-frequency amplitude A of the radiation spectrum obtained for representative viewing angles $\theta = 10°$, 45°, and 80°. For each spectral parameter (indicated on the bottom axis) the graph indicates the range between the maximum and minimum values of A obtained by our variations of that parameter. (The parameter variations are as indicated in the previous figures and described in detail in the text.)

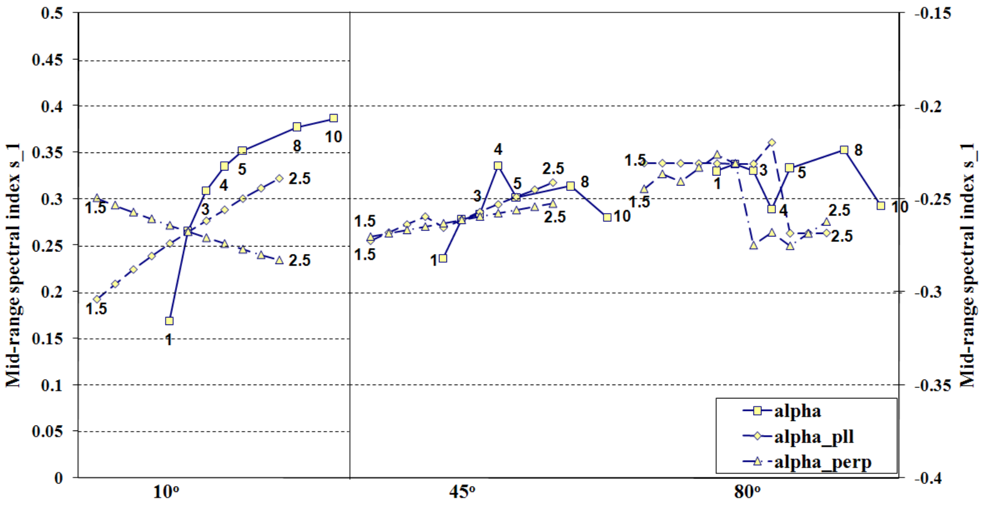

Figure 5.8: This figure shows the variation of the mid-range spectral index with changes in the magnetic field parameters α_i. This is the maximum slope below the peak for peaked spectra, and the average slope in intermediary region for unpeaked spectra, and is shown for representative viewing angles $\theta = 10^\circ$, 45°, and 80°. The solid line with square data points indicates the behavior when α is jointly varied (over a range from 1 to 10, as indicated) in both the transverse and parallel magnetic field equation: $\alpha = \alpha_\perp = \alpha_\parallel$. The dotted lines show the effect of varying $\alpha_\perp$ (triangular data points) and $\alpha_\parallel$ (diamond data points) individually, from 1.5 to 2.5, in increments of 0.1.

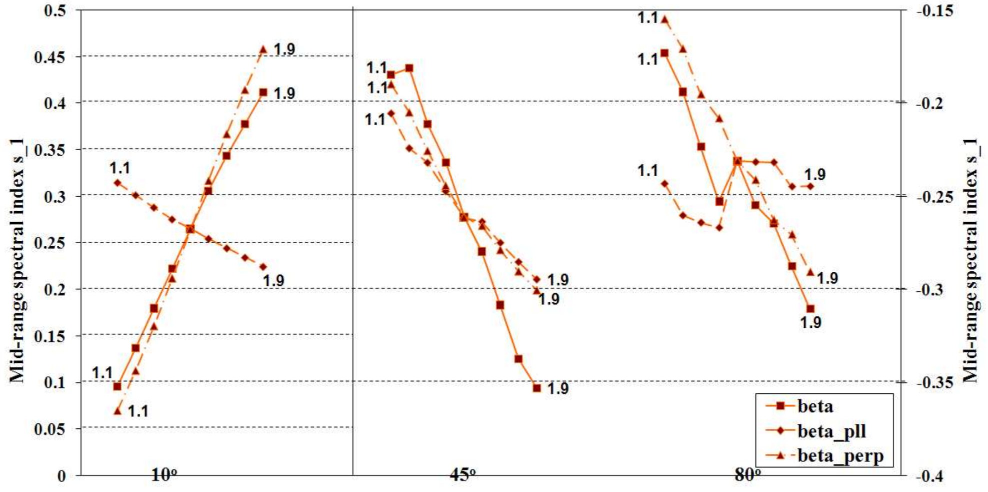

Figure 5.9: This figure shows the variation of the mid-range spectral index with changes in the magnetic field parameters β_i. The solid line with square data points indicates the behavior when β is jointly varied from 1.1 to 1.9, in increments of 0.1, in both the transverse and parallel magnetic field equation: $\beta = \beta_\perp = \beta_\|$. The dotted lines show the effect of varying $\beta_\perp$ (triangular data points) and $\beta_\|$ (diamond data points) individually, also from 1.1 to 1.9, in increments of 0.1.

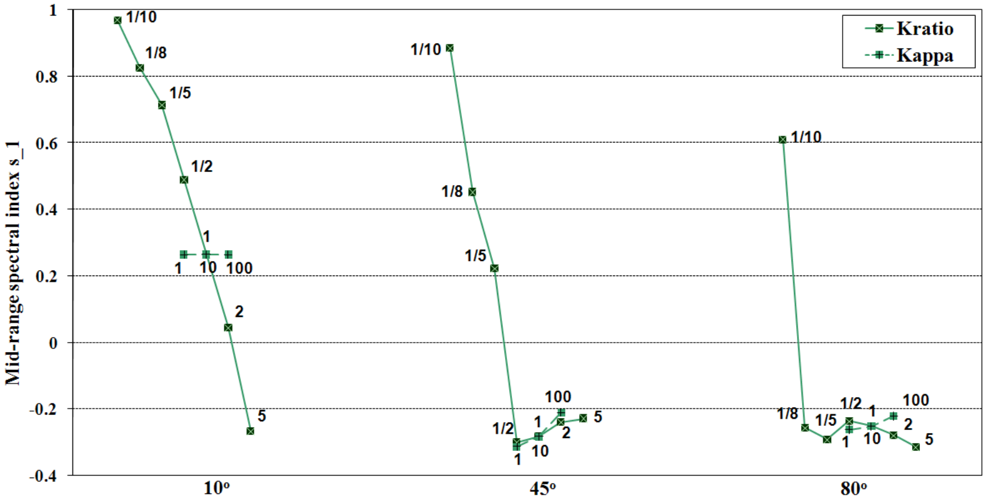

Figure 5.10: This figure shows the variation of the mid-range spectral index with changes in the magnetic field parameters κ. We vary κ jointly ($\kappa = \kappa_\perp = \kappa_\|$) by powers of 10, from 1 to 100, as indicated by the dotted line. We also vary $\kappa_\perp$ and $\kappa_\|$ relative to one another by changing the ratio $K = \kappa_\perp/\kappa_\|$ through a range of values as indicated by the solid line.

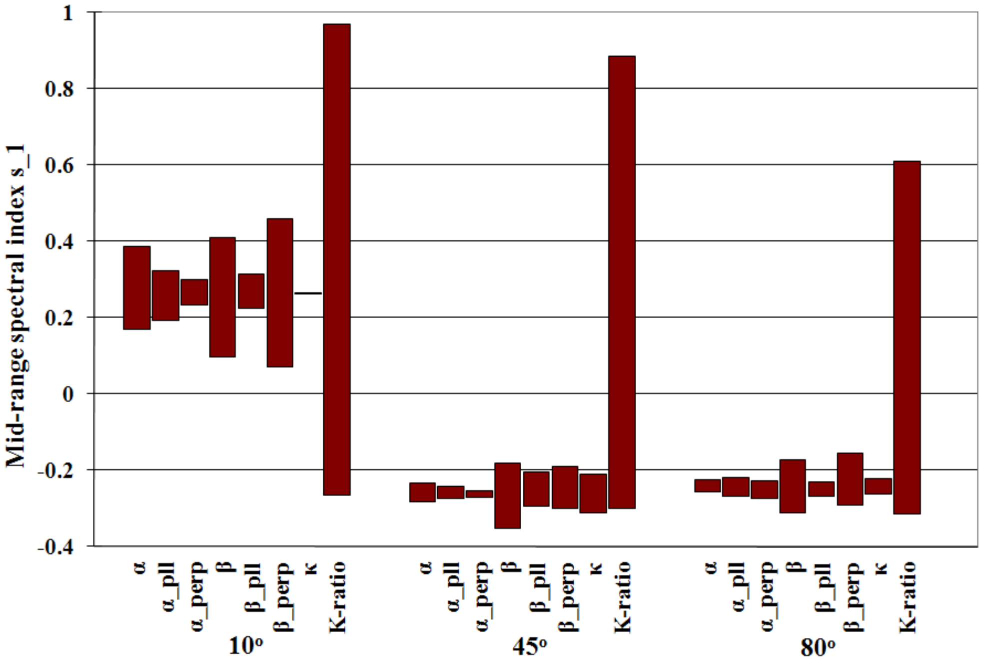

Figure 5.11: This figure compares the influences of different magnetic field spectral parameters on the mid-range spectral index s_1 of the radiation spectrum obtained for representative viewing angles $\theta = 10^\circ$, 45°, and 80°. For each spectral parameter (indicated on the bottom axis) the graph indicates the range between the maximum and minimum values of s_1 obtained by our variations of that parameter (The parameter variations are as indicated in the previous figure and described in detail within the text.)

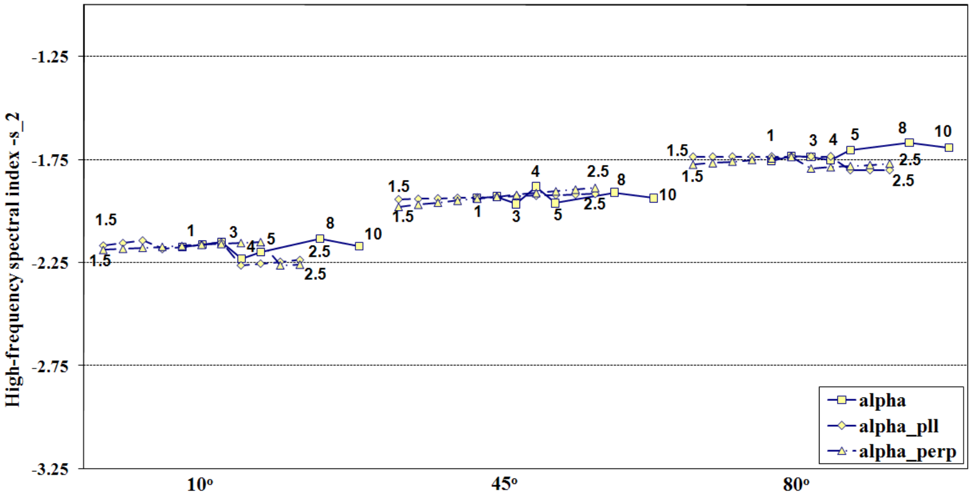

Figure 5.12: This figure shows the variation of the high-frequency spectral index with changes in the magnetic field parameters α_i. The solid line with square data points indicates the behavior when α is jointly varied (over a range from 1 to 10, as indicated) in both the transverse and parallel magnetic field equation: $\alpha = \alpha_\perp = \alpha_\|$. The dotted lines show the effect of varying $\alpha_\perp$ (triangular data points) and $\alpha_\|$ (diamond data points) individually, from 1.5 to 2.5, in increments of 0.1.

shifting of the function (as indicated in our analysis of the spectral breaks below) towards higher frequencies interferes with the calculation of s_2 by shifting the absolute minumum of the second derivative outside our calculation boundaries. This causes an artificial reduction in the steepness of the slope for $\kappa = 100$, as evident also in Figure 5.14.

We calculate the first spectral break (i.e. transition point) as the intersection between the line $\log \left\langle |\mathbf{w}_{\omega'}|^2 \right\rangle = A$ and the line of slope s_1 through the point of maximum positive slope for peaked spectra or through the data point in the middle of the range over which we averaged to obtain slope s_1 for unpeaked spectra. (If the middle of the range does not fall on a data point, we take the next larger data point.) We find, as shown in figures 5.16-5.19, that the first spectral break is strongly influenced by changes in α and κ or the κ-ratio K. The break position shifts to higher frequency by about an order of magnitude in e as we increase α from 1 to 10 jointly in the parallel and perpendicular

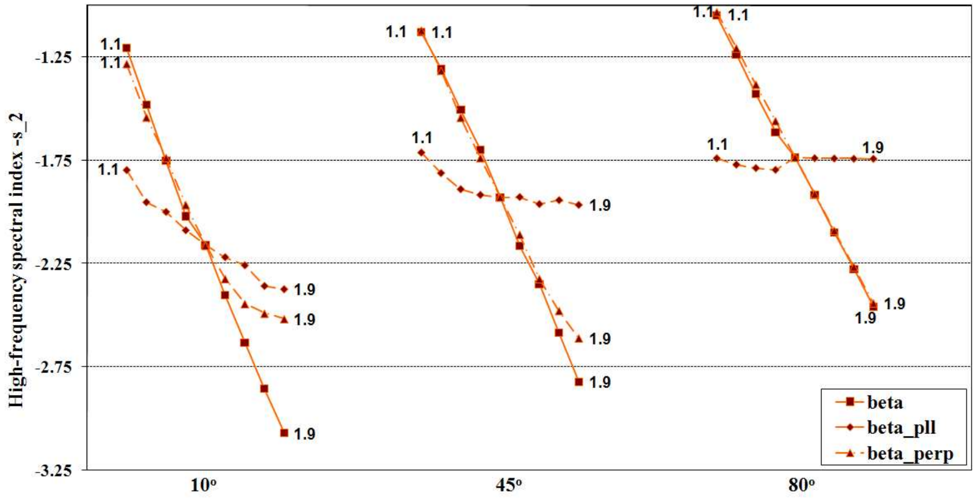

Figure 5.13: This figure shows the variation of the high-frequency spectral index with changes in the magnetic field parameters β_i. The solid line with square data points indicates the behavior when β is jointly varied from 1.1 to 1.9, in increments of 0.1, in both the transverse and parallel magnetic field equation: $\beta = \beta_\perp = \beta_\|$. The dotted lines show the effect of varying $\beta_\perp$ (triangular data points) and $\beta_\|$ (diamond data points) individually, also from 1.1 to 1.9, in increments of 0.1.

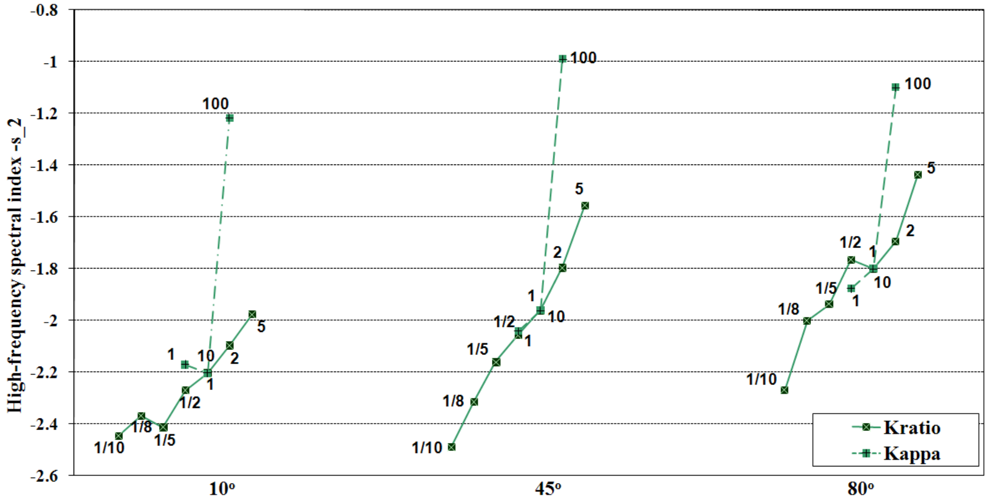

Figure 5.14: This figure shows the variation of the high-frequency spectral index with changes in the magnetic field parameters κ. We vary κ jointly ($\kappa = \kappa_\perp = \kappa_\|$) by powers of 10, from 1 to 100, as indicated. We also vary $\kappa_\perp$ and $\kappa_\|$ relative to one another by changing the ratio $K = \kappa_\perp / \kappa_\|$ through a range of values as indicated.

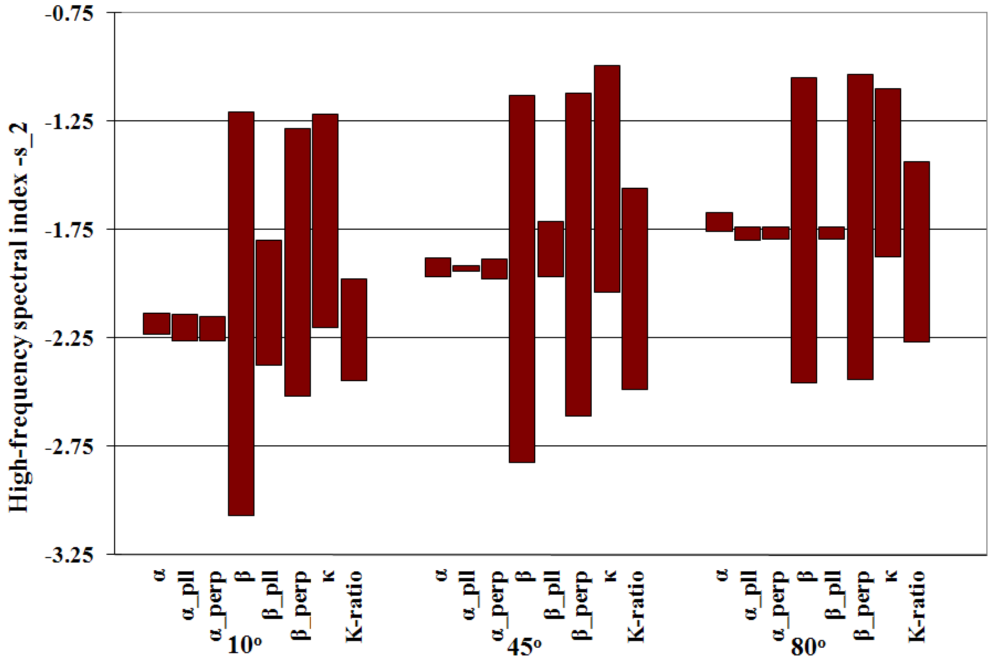

Figure 5.15: This figure compares the influences of different magnetic field spectral parameters on the high-frequency spectral index $-s_2$ of the radiation spectrum. For each spectral parameter (indicated on the bottom axis) the graph indicates the range between the maximum and minimum values of $-s_2$ obtained by our variations of that parameter (The parameter variations are as indicated in the previous figures and described in detail in the text.)

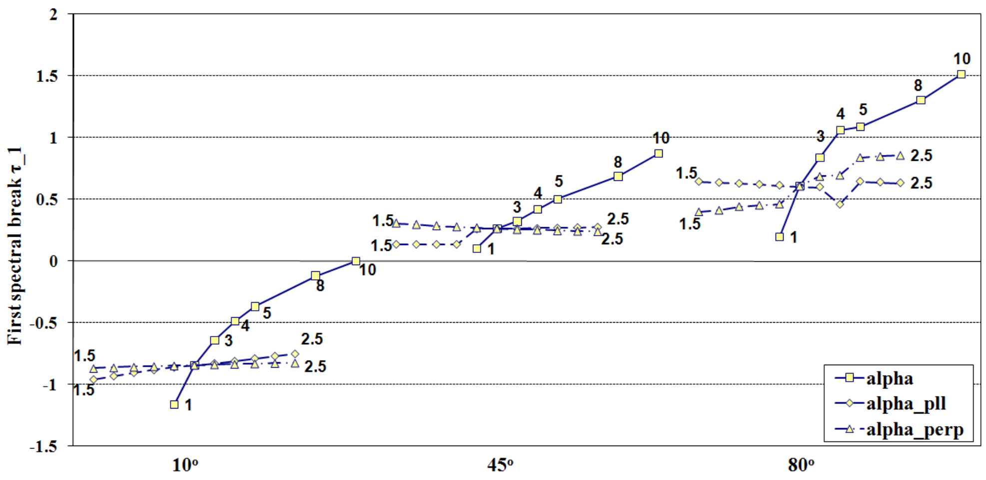

Figure 5.16: This figure shows the variation of the first spectral transition point with changes in the magnetic field parameters α_i, for $\theta = 10°$, $45°$, and $80°$. The solid line with square data points indicates the behavior when α is jointly varied (over a range from 1 to 10, as indicated) in both the transverse and parallel magnetic field equation: $\alpha = \alpha_\perp = \alpha_\|$. The dotted lines show the effect of varying $\alpha_\perp$ (triangular data points) and $\alpha_\|$ (diamond data points) individually, from 1.5 to 2.5, in increments of 0.1.

magnetic field spectra. In varying the α_i separately we see that $\alpha_\|$ has a larger influence at $\theta = 10°$ and $\alpha_\perp$ has a larger influence at $\theta = 80°$. Increasing the κ jointly by powers of 10 results in shifting the first spectral break to higher frequencies by roughly 4 orders of magnitude in e. Varying the κ parameters relative to one another results in a similarly strong shift, towards higher frequencies for $\kappa_\perp > \kappa_\|$.

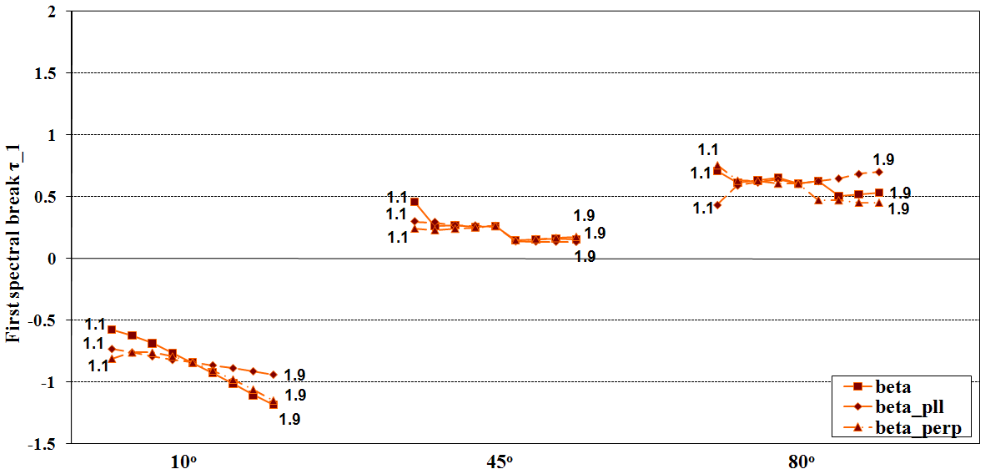

Figure 5.17: This figure shows the variation of the first spectral transition point with changes in the magnetic field parameters β_i, for $\theta = 10°$, 45°, and 80°. The solid line with square data points indicates the behavior when β is jointly varied from 1.1 to 1.9, in increments of 0.1, in both the transverse and parallel magnetic field equation: $\beta = \beta_\perp = \beta_\parallel$. The dotted lines show the effect of varying $\beta_\perp$ (triangular data points) and $\beta_\parallel$ (diamond data points) individually, also from 1.1 to 1.9, in increments of 0.1.

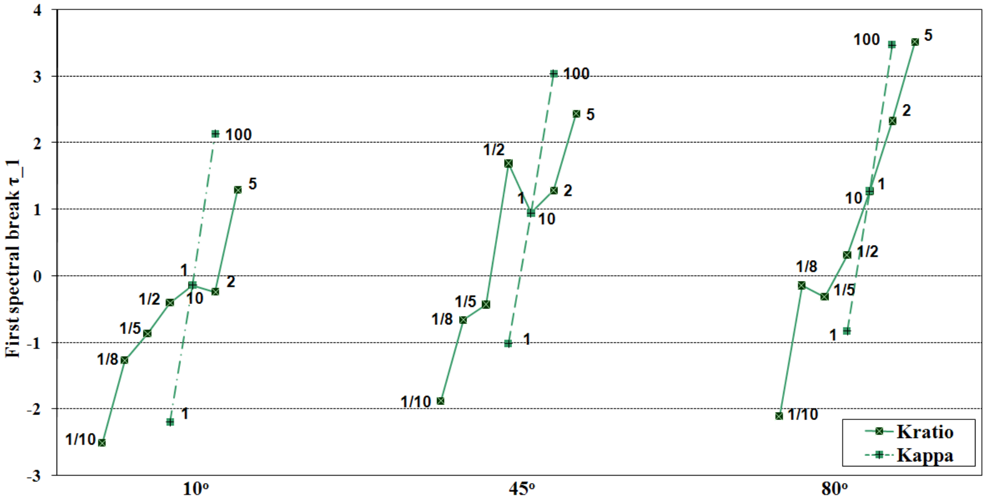

Figure 5.18: This figure shows the variation of the first spectral transition point with changes in the magnetic field parameters κ_i, for $\theta = 10^\circ$, 45°, and 80°. We vary κ jointly ($\kappa = \kappa_\perp = \kappa_\|$) by powers of 10, from 1 to 100, as indicated by the dotted lines. We also vary $\kappa_\perp$ and $\kappa_\|$ relative to one another by changing the ratio $K = \kappa_\perp / \kappa_\|$ through a range of values as indicated by the solid lines.

The second spectral break τ_2 is calculated as the intersection between a line of slope s_1 through the point of maximum positive slope (for peaked spectra) or through the mid-point of the averaging region (for unpeaked spectra), and the line of slope $-s_2$ through the ”drop point" at which the second derivative reaches a minimum (i.e., the largest negative change in the slope). Our results (in figures 5.20-5.23) indicate that the second transition point is most strongly influenced by the κ_i varied jointly or via the ratio K. The low-wavenumber magnetic field spectral index also demonstrates a fairly strong influence, with larger α shifting τ_2 to higher frequencies. A comparison of the influence of α on the two spectral break points (as seen in Figures 5.16 and 5.20) indicates a very similar shift in both break points; thus increasing α shifts the entire spectrum towards higher frequencies.

Figures 5.24-5.26 show the variation in the peak strength (which we have defined as the height of the spectral peak above the low-frequency amplitude A with changes

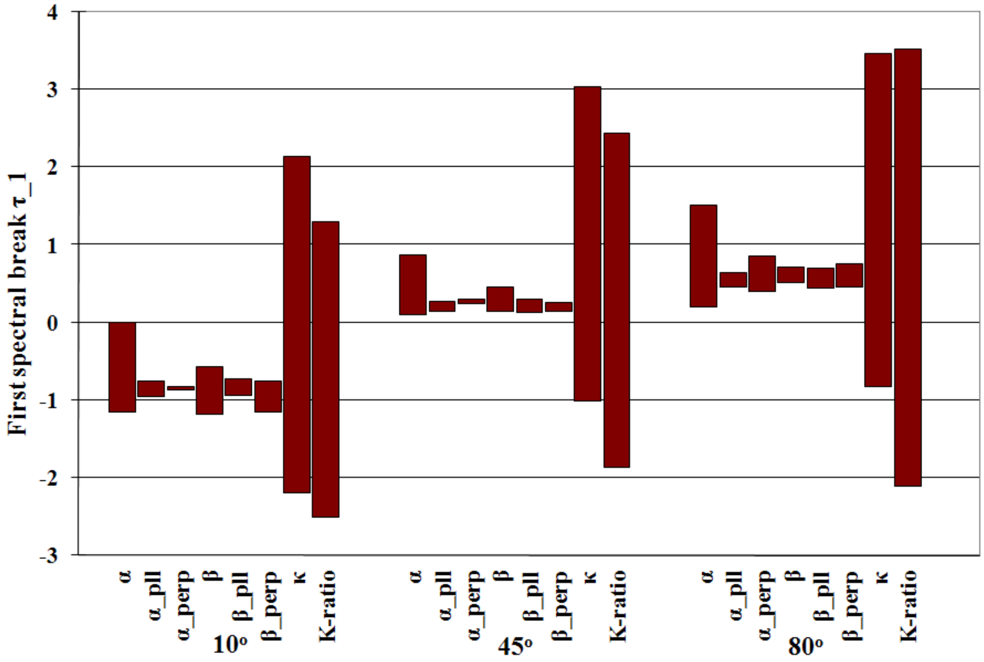

Figure 5.19: This figure compares the influences of different magnetic field spectral parameters on the first spectral break $\log_e(\omega/\omega_o\gamma^2) = \tau_1$ of the radiation spectrum obtained for representative viewing angles $\theta = 10°$, $45°$, and $80°$. For each spectral parameter (indicated on the bottom axis) the graph indicates the range between the maximum and minimum values of τ_1 obtained by our variations of that parameter. (The parameter variations are as indicated in the previous figure and described in detail within the text.

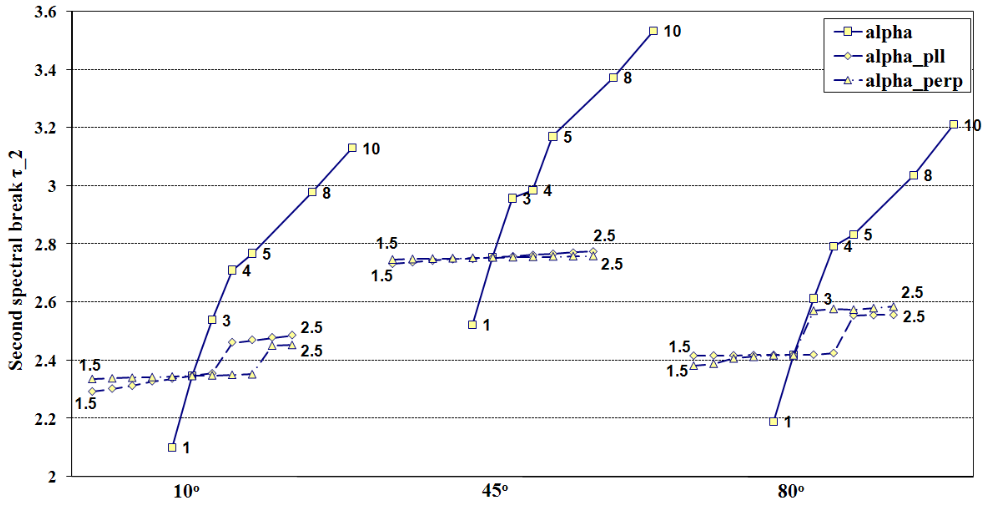

Figure 5.20: This figure shows the variation of the second spectral transition point with changes in the magnetic field parameters α_i. The solid line with square data points indicates the behavior when α is jointly varied (over a range from 1 to 10, as indicated) in both the transverse and parallel magnetic field equation: $\alpha = \alpha_{\perp} = \alpha_{\parallel}$. The dotted lines show the effect of varying $\alpha_{\perp}$ (triangular data points) and $\alpha_{\parallel}$ (diamond data points) individually, from 1.5 to 2.5, in increments of 0.1.

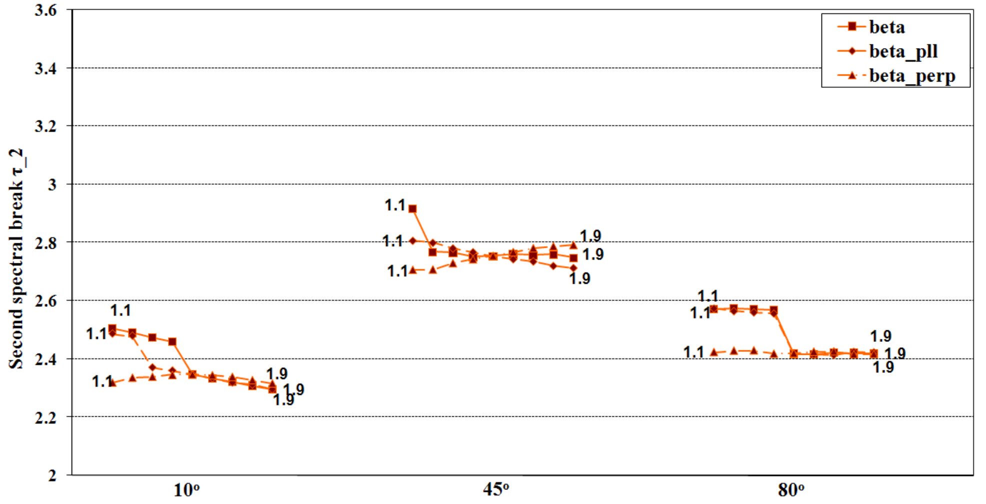

Figure 5.21: This figure shows the variation of the second spectral transition point with changes in the magnetic field parameters β_i. The solid line with square data points indicates the behavior when β is jointly varied from 1.1 to 1.9, in increments of 0.1, in both the transverse and parallel magnetic field equation: $\beta = \beta_{\perp} = \beta_{\parallel}$. The dotted lines show the effect of varying $\beta_{\perp}$ (triangular data points) and $\beta_{\parallel}$ (diamond data points) individually, also from 1.1 to 1.9, in increments of 0.1.

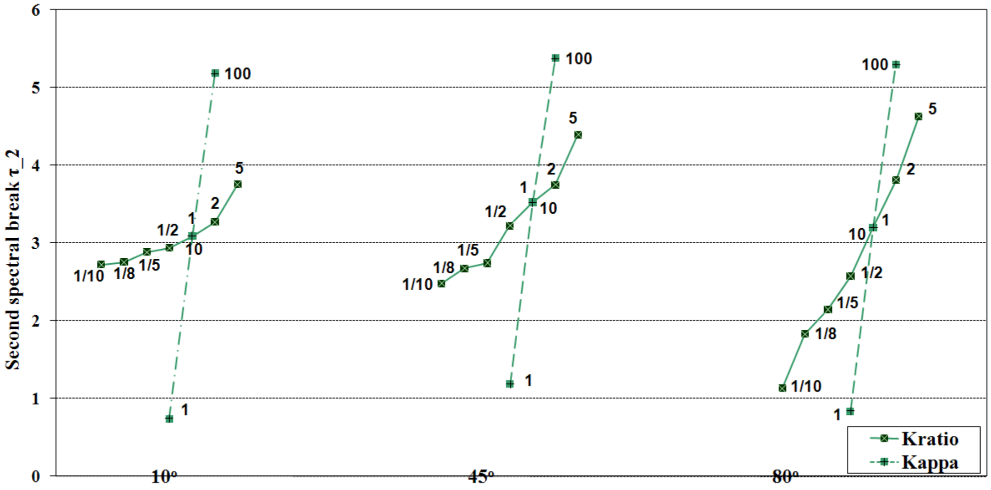

Figure 5.22: This figure shows the variation of the second spectral break with changes in the magnetic field parameters κ. We vary κ jointly ($\kappa = \kappa_\perp = \kappa_\|$) by powers of 10, from 1 to 100, as indicated by the dotted line. We also vary $\kappa_\perp$ and $\kappa_\|$ relative to one another by changing the ratio $K = \kappa_\perp / \kappa_\|$ through a range of values as indicated by the solid line.

in the magnetic field parameters. For $\theta = 10^\circ$, the only of our three representative angles that has peaked spectrum for $K = 1$, peak strength increases with increasing α and β. Individually, increasing $\beta_\perp$ has the largest effect in increasing the peak strength, while increasing $\alpha_\perp$ lowers it. Similarly, increasing $\alpha_\|$ increases the peak strength while increasing $\beta_\|$ lowers it. The largest effect overall is produced by variation of the ratio K between the perpendicular and parallel field parameters κ_i. For $\kappa_\| > \kappa_\perp$ (i.e. $K < 1$), the peak strength appears to persist to higher angles θ, while for $\kappa_\perp > \kappa_\|$ the peak can be small or non-existent even at $\theta = 10^\circ$. Thus the ratio between $\kappa_\perp$ and $\kappa_\|$, the respective peaks of the magnetic field perpendicular and parallel spectra, strongly influences the progression of the spectral evolution between its $\theta = 0$ and $\theta = \pi/2$ limiting values, as expected.

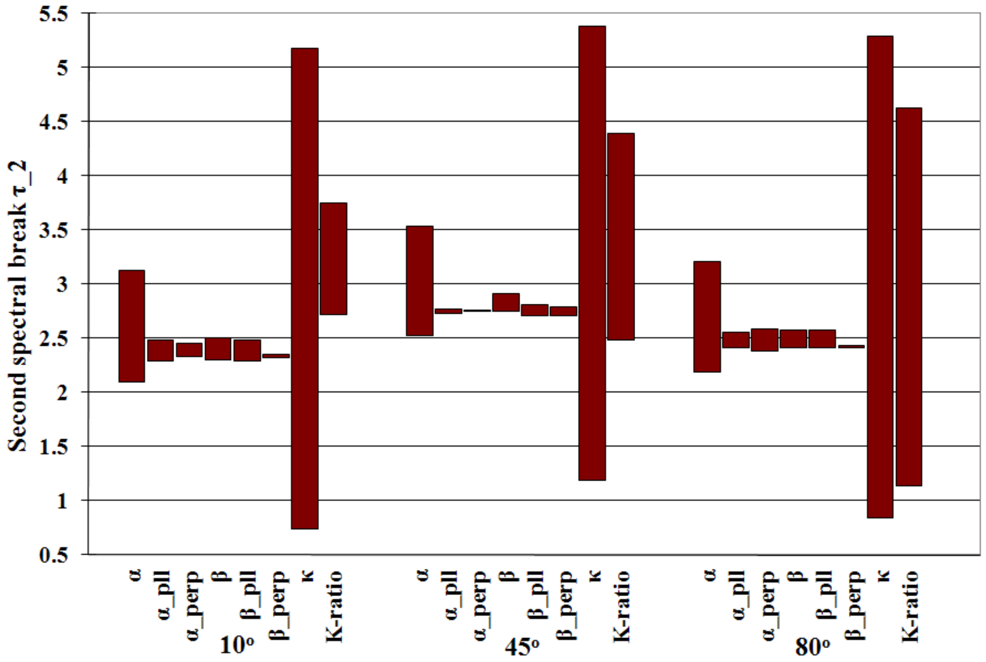

Figure 5.23: This figure compares the influences of different magnetic field spectral parameters on the second spectral break $\log_e(\omega/\omega_o\gamma^2) = \tau_2$ of the radiation spectrum. For each spectral parameter (indicated on the bottom axis) the graph indicates the range between the maximum and minimum values of τ_2 obtained by our variations of that parameter (The parameter variations are as indicated in the previous figure and described in detail in section within the text.

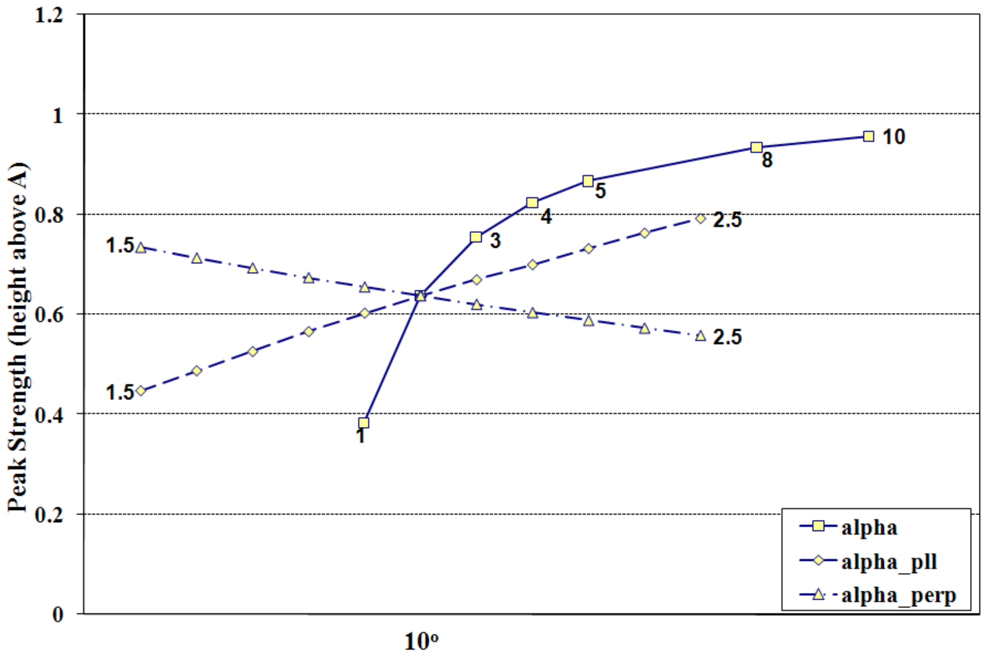

Figure 5.24: This figure shows the variation of peak strength, namely the peak height relative to the initial amplitude, for changes in the magnetic field parameters α_i. We present results only for $\theta = 10°$ because at $\theta = 45°$ and $\theta = 80°$ the spectrum is unpeaked. The solid line with square data points indicates the behavior when α is jointly varied (over a range from 1 to 10, as indicated) in both the transverse and parallel magnetic field equation: $\alpha = \alpha_\perp = \alpha_\|$. The dotted lines show the effect of varying $\alpha_\perp$ (triangular data points) and $\alpha_\|$ (diamond data points) individually, from 1.5 to 2.5, in increments of 0.1.

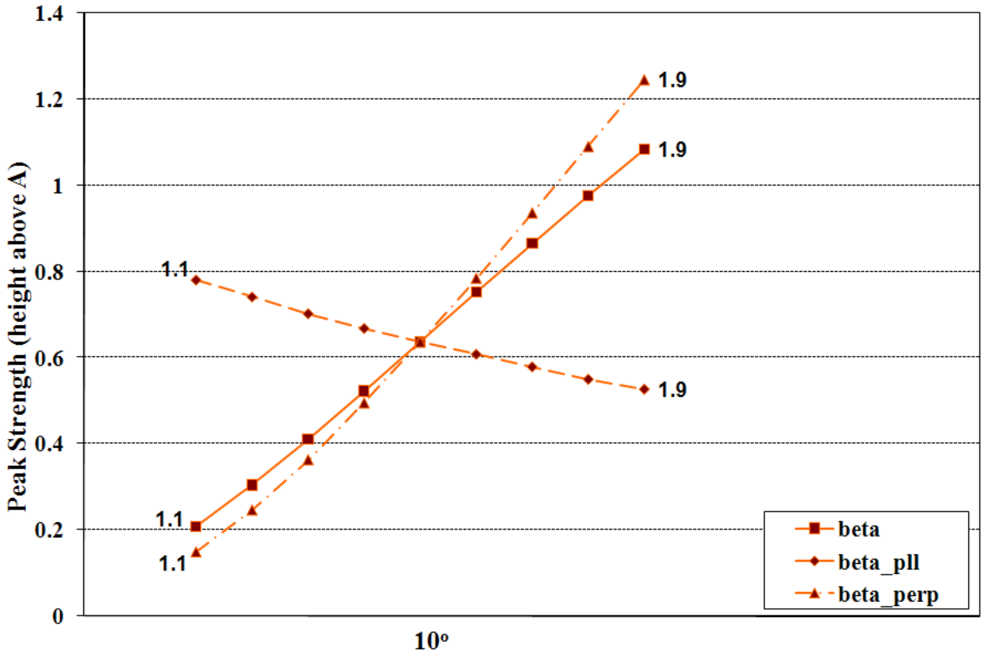

Figure 5.25: This figure shows the variation of peak strength (the peak height relative to the initial amplitude) with changes in the magnetic field parameters β_i. The solid line with square data points indicates the behavior when β is jointly varied from 1.1 to 1.9, in increments of 0.1, in both the transverse and parallel magnetic field equation: $\beta = \beta_\perp = \beta_\|$. The dotted lines show the effect of varying $\beta_\perp$ (triangular data points) and $\beta_\|$ (diamond data points) individually, also from 1.1 to 1.9, in increments of 0.1.

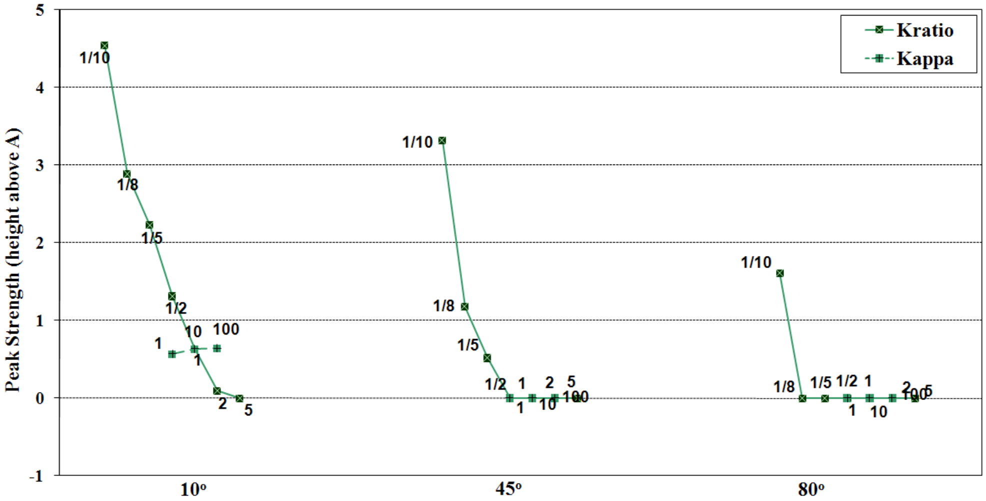

Figure 5.26: This figure shows the variation of peak strength (the peak height relative to the initial amplitude) with changes in the magnetic field parameters κ. We vary κ jointly ($\kappa = \kappa_\perp = \kappa_\parallel$) by powers of 10, from 1 to 100, as indicated. We also vary $\kappa_\perp$ and $\kappa_\parallel$ relative to one another by changing the ratio $K = \kappa_\perp / \kappa_\parallel$ through a range of values as indicated. Note that we obtain peaked forms of the spectra for larger θ when we have small values of the ratio K.

5.4 Discussion of Results

We have seen that relatively minor changes in the magnetic field spectra can produce notable effects upon the jitter radiation spectra, particularly in determining whether the spectrum at certain viewing angles θ are peaked or unpeaked and at what energy the peak or break appears. While we have included in this section only spectra from a few representative viewing angles θ, the angular dependence of these spectra demonstrates that the connection of spectral features to the defining characteristics of the transverse or parallel magnetic field spectra can be tested by observing their variation with viewing angle.

Variations in the magnetic field spectral parameters influence the final radiation spectrum by controlling the width and peak-positions of the functions within the integrand and the extent to which this directly modifies the effect of the offset, which is proportional to ω'. If we consider the general progression of the radiation spectra from being strongly peaked at small θ to unpeaked at θ near $\pi/2$, the trends shown here indicate that the speed of the progression of the spectral shape between the two extremes is dependent on the relative strengths of the parameters in the magnetic field spectra transverse and parallel to the shock front.

We have also developed in detail the connection between the radiation spectrum and the underlying Fourier spectrum of the particle's acceleration. In particular, we find that the radiation spectrum has much the same shape as the acceleration spectrum but that the apparent transition points in the two spectra do not simply coincide for most angles of θ. Furthermore, although the acceleration spectrum sees the re-emergence of a spectral peak for $\theta \to \pi/2$, the radiation spectrum does not. We have also demonstrated that a simple fit to the acceleration (or angle-resolved) spectrum allows for the generation of a model radiation (angle-averaged) spectrum which approximates the realistic one with 10% accuracy.

In our exploration of the jitter radiation spectral parameter space, we have confirmed that the jitter radiation high-energy spectral index is determined primarily by the high-k magnetic field spectral index β, which otherwise has little influence on the spectrum. The low-k magnetic field spectral index α significantly influences the low-energy and mid-range portions of the radiation spectrum when varied jointly in both magnetic field spectrum, but this influence is substantially reduced when only one α_i is varied.

The parameters $\kappa_\perp$ and $\kappa_\|$ represent the dimensionless correlation lengths of the magnetic field distribution in the direction along the Weibel current filaments (and the direction of shock propagation in the case of a GRB) and in the perpendicular plane (parallel to the shock plane for a GRB). We find that increasing $\kappa_\perp$ and $\kappa_\|$ jointly shifts the entire spectrum to higher energies with relatively little effect on the spectral shape. Thus, as expected, the location of the spectral peak and break energies (and the corresponding peak energy E_p of the νF_ν spectrum) are determined primarily by the correlation length of the magnetic field turbulence. The progression of the spectral shape between the head-on and edge-on cases is sensitive to the variation of the κ parameter in one function relative to the other, such that for a particular viewing angle θ either peaked or unpeaked spectra can be attained via modification of the κ ratio K. In the extreme that $\kappa_{||}$ is 2 orders of magnitude larger than $\kappa_\perp$ we recover a peaked spectra for the angles as high as $\theta \sim 80$ degrees. It is also notable that the spectral peak and transition points undergo relatively little horizontal shift as K varies when $\theta = 10$ degrees, but shift quite dramatically (3-4 orders of magnitude) during this variation for $\theta = 80$ degrees.

Chapter 6

Conclusion

6.1 Jitter Radiation: General Results and Consequences

The theory of jitter radiation has been developed to accurately model the radiation produced when relativistic charged particles propagate through a turbulent magnetic field which varies on small scales less than a particle Larmor radius. We have demonstrated both theoretically and via numerical calculation that the jitter radiation spectrum depends upon the magnetic field distribution encountered by particle's moving on a path oriented towards an observer. The resulting jitter radiation spectrum thus depends directly upon the magnetic field variations encountered by the particles. This allows for the radiation spectrum produced by a single particle in this scenario to vary more widely in form than the synchrotron case in which the synchrotron emission from a monoenergetic particle distribution always exhibits the same low-frequency power law behavior with a spectral index of 1/3. While particle distribution effects can produce synchrotron radiation spectrum with lower low-frequency spectral indices, higher values are not possible without frequency-dependent absorption effects. The jitter radiation spectrum, however, can vary in its low-frequency spectral index even for the case of a monoenergetic particle distribution, depending on the underlying magnetic field distribution. Consequently, the jitter radiation mechanism can be a natural source of synchrotron-violating spectra.

Small-scale magnetic field turbulence can be established by the Weibel-like filamentation instability, in which perturbations transverse to the flow velocities of counterstreaming particle populations causes the formation and growth of current filaments that reinforce the initial fluctuations in the transverse magnetic field. The filamentation establishes an anisotropy such that the resulting magnetic field distribution can be described in terms of separate distributions of magnetic field wavenumber components along and perpendicular to the current filamentation axis.

Because of relativistic beaming, the radiation produced into a particular direction will be dominated by emission from particles moving with velocities $\boldsymbol{\beta}$ within a small range of angles within $1/\gamma$ of the observer's line of sight. Consequently, the jitter radiation spectrum observed depends upon the angle θ made between the velocity $\boldsymbol{\beta}$ of particles along the observer's line of sight and the filamentation axis $\hat{\mathbf{s}}$. This dependence of jitter radiation's spectral form on viewing angle with respect to magnetic field anisotropy can allow for rapid temporal-evolution of the spectrum based on shock and field geometries, without requiring any evolution of the radiating particle population's distribution function.

6.2 Jitter Radiation as a Laboratory Diagnostic

Jitter radiation's sensitivity to magnetic field distribution within a turbulent region may allow it to serve as a minimally-invasive magnetic field diagnostic in laboratory plasmas. We have calculated the jitter radiation spectrum as may be generated by the Weibel-like filamentation instability when a laboratory laser-plasma experiment when a quasimonoenergetic beam impinges upon a plasma to create current filamentation.

We present results for the spectrum produced both for a monoenergetic "single particle" (or delta function particle distribution) and for a Gaussian distribution of particle energies such as is produced in quasimonoenergetic electron beams. The jitter radiation spectrum produced by a Gaussian distribution of peak energy 200 MeV and full-width-at-half-maximum of 50 MeV showed little overall difference from the single-particle result.

We first considered the radiation from electrons in the instability-generating beam, which may be those caught up in the production of the instability itself. In this initial case, we find that the radiation spectrum produced is reflective of the distribution of the magnetic field wavenumber's component along the filamentation axis ($k_{\parallel}$), with a peak frequency that reflects the dominant wavenumber component and low- and high-frequency spectral indices that reflect the corresponding indices in the distribution of $k_{\parallel}$. Consequently, the resulting spectrum is notably steeper at low-energy wavelengths than the synchrotron case would be: for our choice of field parameters the spectral index has a value of about 4, well exceeding the synchrotron limit of $1/3$.

Secondly, we calculated the radiation produced if a secondary electron beam is used to probe the filamentation region at other angles θ relative to the filamentation axis $\hat{\mathbf{s}}$. Such a scenario allows one to vary the influence of the magnetic field wavenumber components parallel and perpendicular to $\hat{\mathbf{s}}$. A probe angle of $\theta = 90^\circ$ returns a radiation spectrum that depends only on the distribution of the magnitude $k_{\perp}$ of the magnetic field wavevector's projection onto the plane transverse to filamentation. Even for an choice of wavenumber distribution $f_{\perp}(k_{\perp})$ identical to our choice of $f_{\parallel}(k_{\parallel})$ the form of the radiation spectrum produced for $\theta = 90^\circ$ is different than that obtained at $\theta = 0^\circ$ because the projection $\mathbf{k}_{\perp} = k_x\hat{\mathbf{x}} + k_y\hat{\mathbf{y}}$ is a function of two wavenumber components and randomly oriented in the transverse (xy, for our choice of coordinate systems here) plane. Consequently, spectrum produced by particles moving in a direction along one of the transverse components (say along $\hat{\mathbf{x}}$ involves integrating the transverse field distribution over the other transverse component (k_y). As we vary the probe beam's incident angle, we progress from a strongly peaked spectral form with a steep, synchrotron-violating low-energy spectra index, to peaked forms that have a low-energy flattening, and to unpeaked forms with a low-frequency spectral index of 0 and a single break at the transition to the high-frequency spectral index.

For both scenarios, the spectral intensity is greatest when viewed from the beams's forward direction, in keeping with the expected relativistic beaming of the emission. Increasing the viewing angle α between the radiating particle velocity $\boldsymbol{\beta}$ and the direction to an observer $\hat{\mathbf{n}}$ serves both to produce this rapid decrease in the amplitude of the spectrum and to shift the spectral frequency dependence to lower frequencies.

6.3 Jitter Radiation Implications for GRB Studies

As we have seen in Chapter 4, the diversity of jitter radiation spectra even for a monoenergetic particle distribution may explain the rapid temporal spectral evolution seen from certain high-energy astrophysical sources such as gamma-ray bursts. If produced by jitter radiation, such an evolution need not reflect changes in the underlying particle distribution but can instead reflect changes in the viewing angle θ relative to current filaments produced in small-scale magnetic field turbulence by the Weibel-like filamentation instability.

The jitter radiation spectra are also notably not limited by the synchrotron "line of death" that limits the low-energy photon index to values above $-2/3$. Thus jitter radiation may be able to explain observations of synchrotron-violating spectra in a number of GRB time-resolved spectra, without requiring *ad hoc* postulates of selective absorption. If spectra which violate the synchrotron limit can be reliably linked to sites of small-scale magnetic field turbulence, then jitter radiation spectral analysis has the possibility to uncover features of the magnetic field distribution within such astrophysical sources.

Although we have focused on GRBs as possible sources of jitter radiation, many other astrophysical objects may also be likely sites of small-scale magnetic field turbulence. Furthermore, while we have here focused primarily on a filamentation geometry postulated to lie everywhere along the normal to a spherically-propagating shock front, the Weibel-like filamentation instability can arise in other scenarios of counterstreaming particle flow. This could lead to localized "patches" of filamentation, such as in systems where magnetic reconnection leads to rapid outflow of plasma and may generate Weibel filamentation in such regions. Consequently, jitter radiation may be able to trace more complicated behaviors and particle flow structures in GRBs, astrophysical jets, and stellar explosions or eruptions for which magnetic field may vary widely from the large-scale steady-state field required to produce synchrotron radiation.

Bibliography

D. Band, J. Matteson, L. Ford, B. Schaefer, D. Palmer, B. Teegarden, T. Cline, M. Briggs, W. Paciesas, G. Pendleton, G. Fishman, C. Kouveliotou, C. Meegan, R. Wilson, and P. Lestrade. BATSE observations of gamma-ray burst spectra. I - Spectral diversity. *Astrophysical Journal*, 413:281–292, August 1993.

P. N. Bhat, G. J. Fishman, C. A. Meegan, R. B. Wilson, C. Kouveliotou, W. S. Paciesas, G. N. Pendleton, and B. E. Schaefer. Spectral evolution of a subclass of gamma-ray bursts observed by BATSE. *Astrophysical Journal*, 426:604–611, May 1994.

C. Brau. *Modern Problems in Classical Electrodynamics*. Oxford University Press, Oxford, United Kingdom, 2004.

A. Bret, L. Gremillet, and M. E. Dieckmann. Multidimensional electron beam-plasma instabilities in the relativistic regime. *Physics of Plasmas*, 17(12):120501, December 2010.

P. Chang, A. Spitkovsky, and J. Arons. Long-Term Evolution of Magnetic Turbulence in Relativistic Collisionless Shocks: Electron-Positron Plasmas. *Astrophysical Journal*, 674:378–387, February 2008.

A. Crider, E. P. Liang, I. A. Smith, R. D. Preece, M. S. Briggs, G. N. Pendleton, W. S. Paciesas, D. L. Band, and J. L. Matteson. Evolution of the low-energy photon spectra in gamma-ray bursts. *The Astrophysical Journal Letters*, 479(1):L39, 1997. URL `http://stacks.iop.org/1538-4357/479/i=1/a=L39`.

J. Faure, Y. Glinec, A. Pukhov, S. Kiselev, S. Gordienko, E. Lefebvre, J.-P. Rousseau, F. Burgy, and V. Malka. A laser-plasma accelerator producing monoenergetic electron beams. *Nature*, 431:541–544, September 2004.

J. Faure, C. Rechatin, A. Norlin, A. Lifschitz, Y. Glinec, and V. Malka. Controlled injection and acceleration of electrons in plasma wakefields by colliding laser pulses. *Nature*, 444:737–739, December 2006.

R. A. Fonseca, L. O. Silva, J. W. Tonge, W. B. Mori, and J. M. Dawson. Three-dimensional Weibel instability in astrophysical scenarios. *Physics of Plasmas*, 10: 1979–1984, May 2003.

L. A. Ford, D. L. Band, J. L. Matteson, M. S. Briggs, G. N. Pendleton, R. D. Preece, W. S. Paciesas, B. J. Teegarden, D. M. Palmer, B. E. Schaefer, T. L. Cline, G. J. Fishman, C. Kouveliotou, C. A. Meegan, R. B. Wilson, and J. P. Lestrade. BATSE observations of gamma-ray burst spectra. 2: Peak energy evolution in bright, long bursts. *Astrophysics Journal*, 439:307–321, January 1995.

J. T. Frederiksen, C. B. Hededal, T. Haugbølle, and Å. Nordlund. Magnetic Field Generation in Collisionless Shocks: Pattern Growth and Transport. *Astrophysical Journal Letters*, 608:L13–L16, June 2004.

B. D. Fried. Mechanism for Instability of Transverse Plasma Waves. *Physics of Fluids*, 2:337, May 1959.

F. Frontera, L. Amati, E. Costa, J. M. Muller, E. Pian, L. Piro, P. Soffitta, M. Tavani, A. Castro-Tirado, D. Dal Fiume, M. Feroci, J. Heise, N. Masetti, L. Nicastro,

M. Orlandini, E. Palazzi, and R. Sari. Prompt and Delayed Emission Properties of Gamma-Ray Bursts Observed with BeppoSAX. *Astrophysical Journal Supplement Series*, 127:59–78, March 2000.

C. G. R. Geddes, C. Toth, J. van Tilborg, E. Esarey, C. B. Schroeder, D. Bruhwiler, C. Nieter, J. Cary, and W. P. Leemans. High-quality electron beams from a laser wakefield accelerator using plasma-channel guiding. *Nature*, 431:538–541, September 2004.

N. Gehrels, E. Ramirez-Ruiz, and D. B. Fox. Gamma-Ray Bursts in the Swift Era. *Annual Reviews of Astronomy and Astrophysics*, 47:567–617, September 2009.

G. Ghirlanda, L. Nava, G. Ghisellini, A. Celotti, and C. Firmani. Short versus long gamma-ray bursts: spectra, energetics, and luminosities. *Astronomy and Astrophysics*, 496:585–595, March 2009.

V. L. Ginzburg and S. I. Syrovats. Cosmic Magnetobremsstrahlung (Synchrotron Radiation). *Annual Review of Astronomy and Astrophysics*, 3:297–&, 1965.

J. Granot, T. Piran, and R. Sari. Images and Spectra from the Interior of a Relativistic Fireball. *Astrophysical Journal*, 513:679–689, March 1999.

Y. Kaneko. *Spectral studies of gamma-ray burst prompt emission*. PhD thesis, The University of Alabama in Huntsville, Alabama, USA, 2005.

Y. Kaneko, R. D. Preece, M. S. Briggs, W. S. Paciesas, C. A. Meegan, and D. L. Band. The Complete Spectral Catalog of Bright BATSE Gamma-Ray Bursts. *Astrophysical Journal Supplement*, 166:298–340, September 2006.

R. W. Klebesadel, I. B. Strong, and R. A. Olson. Observations of Gamma-Ray Bursts of Cosmic Origin. *Astrophysical Journal Letters*, 182:L85, June 1973.

L. Landau and E. M. Lifshitz. *The Classical Theory of Fields*. Pergamon Press, Oxford, United Kingdom, 1971.

F. Lindau, O. Lundh, S. P. D. Mangles, M. C. Kaluza, K. Krushelnick, Z. Najmudin, A. Persson, A. G. R. Thomas, and C.-G. Wahlstrom. Characterization of Quasi-Monoenergetic Electron Beams at the Lund Laser Centre. *IEEE Transactions on Plasma Science*, 36:1707–1714, August 2008.

V. Malka, J. Faure, Y. A. Gauduel, E. Lefebvre, A. Rousse, and K. T. Phuoc. Principles and applications of compact laser plasma accelerators. *Nature Physics*, 4:447–453, June 2008.

S. P. D. Mangles, C. D. Murphy, Z. Najmudin, A. G. R. Thomas, J. L. Collier, A. E. Dangor, E. J. Divall, P. S. Foster, J. G. Gallacher, C. J. Hooker, D. A. Jaroszynski, A. J. Langley, W. B. Mori, P. A. Norreys, F. S. Tsung, R. Viskup, B. R. Walton, and K. Krushelnick. Monoenergetic beams of relativistic electrons from intense laser-plasma interactions. *Nature*, 431:535–538, September 2004.

M. V. Medvedev. Theory of “Jitter” Radiation from Small-Scale Random Magnetic Fields and Prompt Emission from Gamma-Ray Burst Shocks. *Astrophysical Journal*, 540:704–714, September 2000.

M. V. Medvedev. The Theory of Spectral Evolution of the Gamma-Ray Burst Prompt Emission. *Astrophysical Journal*, 637:869–872, February 2006.

M. V. Medvedev and A. Loeb. Generation of Magnetic Fields in the Relativistic Shock of Gamma-Ray Burst Sources. *Astrophysical Journal*, 526:697–706, December 1999.

M. V. Medvedev, S. S. Pothapragada, and S. J. Reynolds. Modeling Spectral Variability of Prompt Gamma-Ray Burst Emission within the Jitter Radiation Paradigm. *Astrophysical Journal Letters*, 702:L91–L95, September 2009.

P. Mészáros. Gamma-ray bursts. *Reports on Progress in Physics*, 69:2259–2321, August 2006.

K. Nakamura, B. Nagler, C. Tóth, C. G. R. Geddes, C. B. Schroeder, E. Esarey, W. P. Leemans, A. J. Gonsalves, and S. M. Hooker. GeV electron beams from a centimeter-scale channel guided laser wakefield accelerator. *Physics of Plasmas*, 14(5):056708, May 2007.

K.-I. Nishikawa, J. Niemiec, P. E. Hardee, M. Medvedev, H. Sol, Y. Mizuno, B. Zhang, M. Pohl, M. Oka, and D. H. Hartmann. Weibel Instability and Associated Strong Fields in a Fully Three-Dimensional Simulation of a Relativistic Shock. *Astrophysical Journal Lettersl*, 698:L10–L13, June 2009.

J. Osterhoff, A. Popp, Z. Major, B. Marx, T. P. Rowlands-Rees, M. Fuchs, M. Geissler, R. Hörlein, B. Hidding, S. Becker, E. A. Peralta, U. Schramm, F. Grüner, D. Habs, F. Krausz, S. M. Hooker, and S. Karsch. Generation of Stable, Low-Divergence Electron Beams by Laser-Wakefield Acceleration in a Steady-State-Flow Gas Cell. *Physical Review Letters*, 101(8):085002, August 2008.

B. B. Pollock, C. E. Clayton, J. E. Ralph, F. Albert, A. Davidson, L. Divol, C. Filip, S. H. Glenzer, K. Herpoldt, W. Lu, K. A. Marsh, J. Meinecke, W. B. Mori, A. Pak, T. C. Rensink, J. S. Ross, J. Shaw, G. R. Tynan, C. Joshi, and D. H. Froula. Demonstration of a Narrow Energy Spread, 0.5GeV Electron Beam from a Two-Stage Laser Wakefield Accelerator. *Physical Review Letters*, 107(4):045001, July 2011.

S. Pothapragada. *Temporal Variation in Spectral Parameters of Prompt GRB Emission*. PhD thesis, The University of Kansas, Kansas, USA, 2012.

R. D. Preece, M. S. Briggs, R. S. Mallozzi, G. N. Pendleton, W. S. Paciesas, and D. L. Band. The Synchrotron Shock Model Confronts a “Line of Death” in the BATSE Gamma-Ray Burst Data. *Astrophysical Journal Letters*, 506:L23–L26, October 1998.

S. J. Reynolds and M. V. Medvedev. Radiative diagnostics for sub-Larmor scale magnetic turbulence. *Physics of Plasmas*, 19:023106, February 2012.

S. J. Reynolds, S. Pothapragada, and M. V. Medvedev. Angular Dependence of Jitter Radiation Spectra from Small-Scale Magnetic Turbulence. *Astrophysical Journal*, 713:764–779, April 2010.

G. B. Rybicki and A. P. Lightman. *Radiative Processes in Astrophysics*. Wiley-VCH Verlag GmbH & Co. KGaA, Weinheim, Germany, 2004.

F. Ryde and V. Petrosian. Gamma-Ray Burst Spectra and Light Curves as Signatures of a Relativistically Expanding Plasma. *Astrophysical Journal*, 578:290–303, October 2002.

B. E. Schaefer, B. J. Teegarden, S. F. Fantasia, D. Palmer, T. L. Cline, J. L. Matteson, D. L. Band, L. A. Ford, G. J. Fishman, C. A. Meegan, R. B. Wilson, W. S. Paciesas, G. N. Pendleton, M. S. Briggs, and J. P. Lestrade. BATSE spectroscopy catalog of bright gamma-ray bursts. *Astrophysical Journal Supplement*, 92:285–310, May 1994.

L. O. Silva, R. A. Fonseca, J. W. Tonge, J. M. Dawson, W. B. Mori, and M. V. Medvedev. Interpenetrating Plasma Shells: Near-equipartition Magnetic Field Generation and Nonthermal Particle Acceleration. *Astrophysical Journal Letters*, 596: L121–L124, October 2003.

E. S. Weibel. Spontaneously Growing Transverse Waves in a Plasma Due to an Anisotropic Velocity Distribution. *Physical Review Letters*, 2:83–84, February 1959.

E. Woods and A. Loeb. Constraints on Off-Axis X-Ray Emission from Beamed Gamma-Ray Bursts. *Astrophysical Journal*, 523:187–191, September 1999.

S. Zenitani and M. Hesse. The role of the Weibel instability at the reconnection jet front in relativistic pair plasma reconnection. *Physics of Plasmas*, 15(2):022101, February 2008.

E. G. Zweibel and M. Yamada. Magnetic Reconnection in Astrophysical and Laboratory Plasmas. *Annual Review of Astronomy and Astrophysics*, 47:291–332, September 2009.